Earth-Science Reviews 172 (2017) 140–177

Contents lists available at ScienceDirect

Earth-Science Reviews

journal homepage: www.elsevier.com/locate/earscirev

Invited review

Iron formations: A global record of Neoarchaean to Palaeoproterozoic environmental history

K.O. Konhauser[a,*], N.J. Planavsky[b,j], D.S. Hardisty[c], L.J. Robbins[a], T.J. Warchola[a], R. Haugaard[a,d], S.V. Lalonde[e], C.A. Partin[f], P.B.H. Oonk[g], H. Tsikos[g], T.W. Lyons[h,j], A. Bekker[h], C.M. Johnson[i,j]

[a] Department of Earth & Atmospheric Sciences, University of Alberta, Edmonton, Alberta T6G 2E3, Canada
[b] Department of Geology and Geophysics, Yale University, New Haven, CT 06520, USA
[c] Department of Geology and Geophysics, Woods Hole Oceanographic Institution, Woods Hole, MA 02542, USA
[d] Mineral Exploration Research Centre, Harquail School of Earth Science, Laurentian University, Sudbury, Ontario P3E 2C6, Canada
[e] UMR6538 Laboratoire Géosciences Océan, European Institute for Marine Studies, Technopôle Brest-Iroise, Plouzané 29280, France
[f] Department of Geological Sciences, University of Saskatchewan, Saskatoon, Saskatchewan S7N 5E2, Canada
[g] Department of Geology, Rhodes University, Grahamstown 6140, South Africa
[h] Department of Earth Sciences, University of California, Riverside, CA 92521, USA
[i] Department of Geoscience, University of Wisconsin–Madison, Madison, WI 53706, USA
[j] NASA Astrobiology Institute, USA

ABSTRACT

Iron formations (IF) represent an iron-rich rock type that typifies many Archaean and Proterozoic supracrustal successions and are chemical archives of Precambrian seawater chemistry and post-depositional iron cycling. Given that IF accumulated on the seafloor for over two billion years of Earth's early history, changes in their chemical, mineralogical, and isotopic compositions offer a unique glimpse into environmental changes that took place on the evolving Earth. Perhaps one of the most significant events was the transition from an anoxic planet to one where oxygen was persistently present within the marine water column and atmosphere. Linked to this progressive global oxygenation was the evolution of aerobic microbial metabolisms that fundamentally influenced continental weathering processes, the supply of nutrients to the oceans, and, ultimately, diversification of the biosphere and complex life forms. Many of the key recent innovations in understanding IF genesis are linked to geobiology, since biologically assisted Fe(II) oxidation, either directly through photoferrotrophy, or indirectly through oxygenic photosynthesis, provides a process for IF deposition from mineral precursors. The abundance and isotope composition of Fe(II)-bearing minerals in IF additionally suggests microbial Fe(III) reduction, a metabolism that is deeply rooted in the Archaea and Bacteria. Linkages among geobiology, hydrothermal systems, and deposition of IF have been traditionally overlooked, but now form a coherent model for this unique rock type. This paper reviews the defining features of IF and their distribution through the Neoarchaean and Palaeoproterozoic. This paper is an update of previous reviews by Bekker et al. (2010, 2014) that will improve the quantitative framework we use to interpret IF deposition. In this work, we also discuss how recent discoveries have provided new insights into the processes underpinning the global rise in atmospheric oxygen and the geochemical evolution of the oceans.

1. Introduction

Iron formations (IFs) are iron-rich (15–40 wt% Fe) and siliceous (40–60 wt% SiO_2) chemical sedimentary rocks that precipitated from seawater throughout the Precambrian Eon, the majority having been deposited between 2.80 and 1.85 Ga in the Neoarchaean and Palaeoproterozoic (Figs. 1–2). Minimal detrital input during deposition of deep water IF is indicated by low concentrations of Al_2O_3 (< 1 wt%) and trace elements that are enriched in crustal rocks (Ti, Zr, Th, Hf, and Sc < 20 ppm). Most IFs show distinctive layering of variable thickness, from macrobands (meter-thick) to mesobands (centimeter-thick) by which they are typically defined (i.e., banded iron formations, BIFs), to microbands (millimeter and submillimeter layers). Microbands have been linked to episodic hydrothermal input, hypothesised in early

* Corresponding author.
E-mail address: kurtk@ualberta.ca (K.O. Konhauser).

http://dx.doi.org/10.1016/j.earscirev.2017.06.012
Received 26 April 2017; Received in revised form 26 June 2017; Accepted 27 June 2017
Available online 30 June 2017
0012-8252/

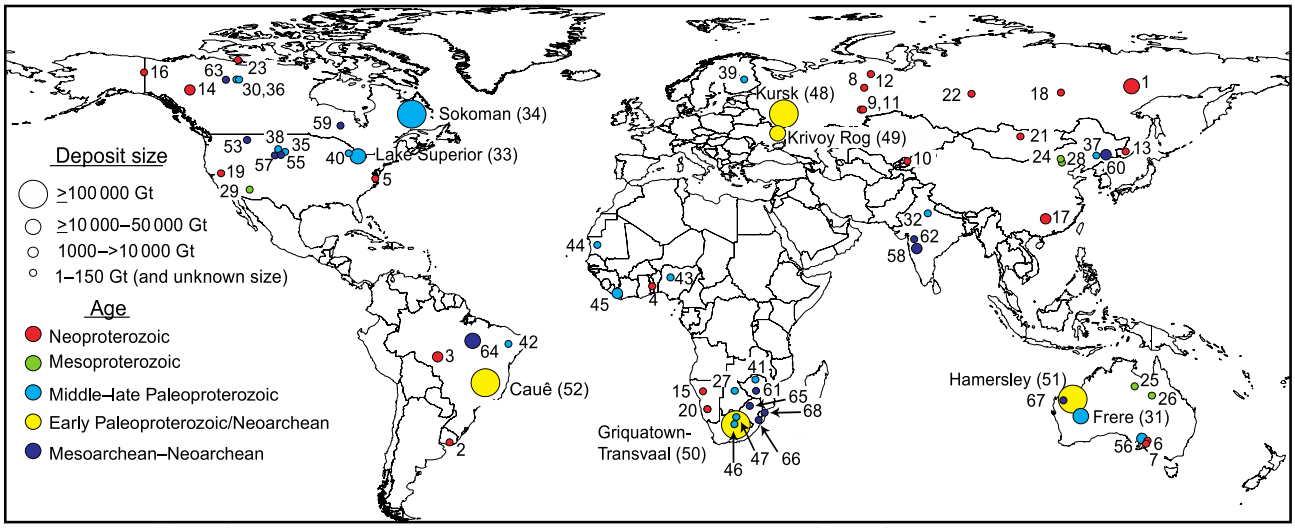

#	Formation/Group/Deposit	Location	Age (Ma)
1.	Maly Khinghan Formation	Russia	560
2.	Yerbel Formation	Uruguay	600
3.	Jacadigo Group (Urucum district)	Brazil	600
4.	Bisokpabe Group	Togo	600
5.	Chestnut Hill Formation	USA	600
6.	Holowilena Ironstone	Australia	650
7.	Braemar Iron Formation	Australia	650
8.	Vil'va and Koyva Formations	Russia	650
9.	Bakeevo (Tolparovo) Formation	Russia	650
10.	Dzhetymtau Suite	Kyrgyzstan	650
11.	UK Formation	Russia	700
12.	Yamata Formation	Russia	700
13.	Lake Khanka Formation	Russia	700
14.	Rapitan Formation	Canada	715
15.	Chuos Formation	Namibia	715
16.	Tindir Group	USA	715
17.	Fulu Formation	China	741
18.	Medvezhevo Formation	Russia	700-750
19.	Kingston Peak Formation	USA	700-750
20.	Numees Formation	Namibia	700-750
21.	Mugur Formation	Mongolia	767
22.	Nizhne-Angara Formation	Russia	800
23.	Aok Formation (Shaler Supergr.)	Canada	840
24.	Xiamaling Formation	China	1368
25.	Roper Group	Australia	1490
26.	South Nicholson Group	Australia	1500
27.	Shoshong Formation	Botswana	1600
28.	Chuanlinggou Iron Formation	China	1650-1600
29.	Pike's Peak Iron-Formation	USA	1728
30.	Gibraltar Formation	Canada	1880
31.	Frere Formation	Australia	1890
32.	Alwar Group (North Delhi fold belt)	India	1850-2000
33.	Lake Superior region	USA + CAN	
	Gunflint Iron Formation	Canada	1878-1850
	Negaunee Iron Formation	USA	1874-1850
	Biwabik Iron Formation	USA	1880-1850
	Ironwood Iron Formation	USA	1880-1850
	Riverton Iron Formation	USA	1880-1850
34.	Sokoman Iron Formation	Canada	1877
35.	Rochford Formation	USA	1884
36.	Basile Formation	Canada	1930
37.	Liaohe Group	China	1950-2050
38.	Estes Formation	USA	2020-2100
39.	Pääkkö Iron Formation	Finland	2080
40.	Glen Township Formation	USA	2100
41.	Lomagundi Group	Zimbabwe	2100-2200
42.	Caldeirão belt	Brazil	>2078-<2687
43.	Malumfashi, Maru, Birnin Gwari, Kushaka, Muro, Egbe-Isanlu, and Obajana schist belts	Nigeria	2100
44.	Ijil Group	Mauritania	2200
45.	Nimba Itabirite	Liberia	>2100-<2615
46.	Hotazel Iron Formation	South Africa	2200
47.	Timeball Hill Formation	South Africa	2320
48.	Kursk Supergroup	Russia	2450
49.	Krivoy Rog Supergroup	Ukraine	2450
50.	Transvaal Province	South Africa	
	Griquatown Iron Formation	South Africa	2431
	Kuruman Iron Formation	South Africa	2465
	Penge Iron Formation	South Africa	2480
51.	Hamersley Basin	Australia	
	Boolgeeda Iron Formation	Australia	2445
	Weeli Wolli Formation	Australia	2449
	Brockman IF (Joffre Mbr)	Australia	2461
	Brockman IF (Dales Gorge Mbr)	Australia	2461-2495
	Mt. Sylvia Formation	Australia	2505
	Marra Mamba Iron Formation	Australia	2597
52.	Cauê Formation	Brazil	2450
53.	Indian Creek Metamorphic Suite	USA	2470-2750
54.	Ruker Series	Antarctica	2450-2480
55.	Benchmark Iron Formation	USA	2480-2560
56.	Hutchison Group (Middleback)	Australia	2500
57.	Nemo Iron Formation	USA	2560-2890
58.	Chitradurga Group	India	2614
59.	Beardmore-Geraldton assemblage	Canada	2700
60.	Anshan Iron Formation	China	2700
61.	Manjeri Iron Formation	Zimbabwe	2700-2830
62.	Bababudan Group	India	2720
63.	Central Slave Cover Group	Canada	2730-2920
64.	Carajás Formation	Brazil	2740-2750
65.	West Rand Group	South Africa	2960
66.	Pongola Supergroup	South Africa	2960
67.	Jack Hills belt	Australia	>3080
68.	Moodies Group	South Africa	3230

Fig. 1. Geographical and size distribution of iron formations through time.
Modified from Bekker et al. (2014).

studies to represent an annual depositional process (e.g., Trendall and Blockley, 1970; Morris, 1993). Layering in BIF can be laterally extensive, indicating deposition below wave base. Some IF, known as granular iron formations (GIFs), however, lack this characteristic banding. These are composed of granules of chert and iron oxides or silicates, with early diagenetic chert, carbonate or hematite cement filling pore space (e.g., Simonson, 1985). GIFs are generally thought to have been deposited in shallow water in proximal settings. IFs of all types can provide important information regarding the composition of past oceans, but only if their physical and chemical depositional environment, basin tectonic setting, and primary versus secondary signals can be teased apart. In this review, we address the current state of knowledge surrounding IF deposition and what it can tell us about the evolving Earth.

IFs are broadly defined as being either Algoma-type or Superior-type based on depositional environment (Gross, 1980), although it is more practical to consider these classifications as end members having a spectrum of intermediate varieties (Bekker et al., 2012). Algoma-type IF are interlayered with, or stratigraphically and genetically linked to, submarine-emplaced mafic-ultramafic to felsic volcanic rocks and associated volcaniclastic greywackes and shales in greenstone belts, and in many cases, spatially coupled with volcanogenic massive sulfide

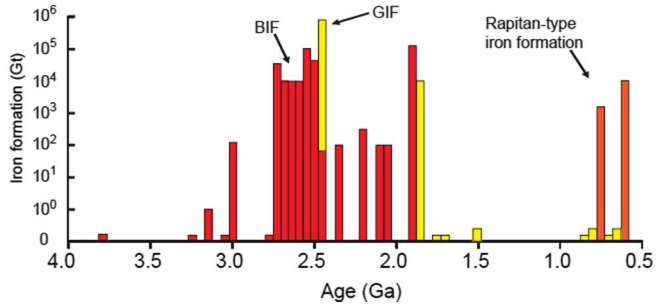

Fig. 2. Iron formation deposition in billions of metric tonnes with 50 m.y. bar widths (modified from Bekker et al., 2010). Most deposits before 2.4 Ga comprise BIF; those ca. 2.3–0.8 Ga are predominantly GIF; Neoproterozoic Rapitan-type iron formation (~0.715 Ga) are associated with glacial deposits.

(VMS) deposits (Bekker et al., 2010). Algoma-type IFs were apparently formed close to volcanic arcs and spreading centres and produced by exhalative hydrothermal processes related to submarine volcanism (e.g., Goodwin, 1962; Gross, 1980, 1983). These IFs contain oxide, silicate, and carbonate facies and commonly grade into sulfidic sediments, which can be enriched in copper, zinc, lead, silver, and gold. The lack of any sedimentological features besides fine banding (i.e., absence of current-, tide-, or wave-generated sedimentary structures) in Algoma-type IF indicates a deep-water depositional environment, likely distal to continental landmasses (Bekker et al., 2010). In this regard, Algoma-type IFs have compositions that reflect the influence of local hydrothermal vent fluids in either partially closed basins or open seawater systems (Gourcerol et al., 2016). Iron formations that precipitated before 3.0 Ga are generally described as being Algoma-type, though there are also examples that formed at 2.7–2.6 Ga, as well as non-Algoma, shallow-marine jasper/IF sequences in the Palaeoarchaean.

In contrast, Superior-type IFs developed in passive-margin, sediment-dominated settings (i.e., after stable continental shelves evolved) and generally lack direct stratigraphic relations with volcanic rocks. These IFs are regarded as having been deposited in near-shore shelf environments (e.g., Trendall, 2002) because they are typically interbedded with, or grade into, carbonates and black shales (Gross, 1980). Unlike most Algoma-type IFs, which rarely extend for > 10 km along strike and typically are not > 50 m thick, Superior-type IFs can be very laterally extensive, with original aerial extents estimated in some cases to be over 100,000 km^2 (Isley, 1995; Bekker et al., 2010). In terms of mass, the largest Superior-type IFs contain over 10^{14} tons of iron (Isley, 1995), supplying the majority of iron required for the world's economy. These IFs include those of the Hamersley Range in Australia, Minas Gerais in Brazil, Transvaal Supergroup in South Africa, Krivoy Rog in Ukraine, and the Labrador Trough in Canada (see Fig. 1).

As noted above, texturally, IF are divided into two groups – BIF and GIF. BIF are dominant in Eoarchaean to early Palaeoproterozoic successions. They consist mainly of interbanded iron- and silica-rich layers and were generally, but not entirely, deposited in relatively deep-water settings, as they typically lack evidence for wave or storm action (Simonson and Hassler, 1996; Trendall, 2002; Krapež et al., 2003) (Fig. 3). Most BIF commonly are either overlain or underlain by organic matter-rich and sulfidic shales, and, in some cases, are interstratified with them. For example, the well-studied 2.48 Ga Dales Gorge Member of the Brockman Iron Formation in Western Australia is composed of 17 BIF macrobands intercalated with 16 shale ("S") macrobands (Trendall and Blockley, 1970), a sequence that has been correlated with age-equivalent IFs in South Africa (Beukes and Gutzmer, 2008). These shales are thought to be shallower-water equivalents of BIF (e.g., Beukes and Klein, 1990; Beukes et al., 1990; Beukes and Cairncross, 1991; Bau and Dulski, 1996). There are, however, several key examples of shallow-water Archaean BIF that are interbedded with sandstones (e.g., Fralick and Pufahl, 2006).

GIF first appear in the rock record at ca. 2.90 Ga (Siahi et al., 2017), reach their acme at ca. 1.88 Ga, and are then replaced by ironstones in the Phanerozoic record (after ca. 543 Ma) (Bekker et al., 2014). They are characterised by granules that can vary in morphology, size (micrometers to centimeter in diameter), and composition (chert, iron oxides, iron carbonates, and/or iron silicates); the cement is typically chert, carbonate or hematite (Fig. 4). Many of the granules are considered detrital, with some being derived by sedimentary re-working of iron-rich clay, mudstones, arenites, and even stromatolites (e.g., Ojakangas, 1983; Simonson and Goode, 1989). Others, such as the ca. 2.32 Ga oolitic GIF of the Timeball Hill Formation in South Africa, are composed of concentric cortices of hematite (Dorland, 1999) that were likely precipitated where Fe(II)-rich waters met more oxygenated shallow seawater. The granules are either grain- or cement-supported; in the case of the latter, it appears that the cement precipitated early, protecting the granules from compaction and preserving "floating" textures. The presence of wave- and current-formed sedimentary structures and hummocky cross-stratification indicates that the granules were deposited near-shore in water depths close to, or above, storm and fair-weather wave base (e.g., Dorland, 1999; Pufahl and Fralick, 2004).

What is the mineralogy of IFs and what do they record about coeval seawater? The best-preserved successions are remarkably uniform, composed mostly of fine-grained quartz (in the form of chert), magnetite, and hematite, with variable amounts of Fe-rich silicate minerals (e.g., stilpnomelane, minnesotaite, greenalite, and riebeckite), carbonate minerals (siderite, ankerite, calcite, and dolomite), and locally sparse sulfides (pyrite and pyrrhotite). The presence of both ferric and ferrous minerals gives IFs an average oxidation state of $Fe^{2.4+}$ (Klein and Beukes, 1992). James (1954) defined four facies of IFs: oxide, silicate, carbonate, and sulfide; they are generally interbedded with variably recrystallised chert (Simonson, 2003). The oxide facies consist predominantly of magnetite and/or hematite, whereas carbonate-facies varieties contain siderite or ankerite as major constituents. The mineralogy of silicate-facies IF is more complex and depends to a large extent on the degree of metamorphism. Under relatively low-grade metamorphic conditions (greenschist facies or below), greenalite, minnesotaite, stilpnomelane, chamosite, ripidolite, riebeckite, and ferriannite may be present (Klein, 2005). At higher grades, cummingtonite, grunerite, actinolite, hornblende, pyroxene, garnet, and fayalite can be present. The sulfide-facies IF described by James (1954) are now believed to be pyritic carbonaceous shales and ferruginous slates, and therefore do not represent a chemical precipitate (Bekker et al., 2010). Given that the accumulation of sulfide and subsequent pyrite formation requires iron limitation (Berner, 1984; Poulton and Canfield, 2011), Bekker et al. (2010) suggested that sulfide-facies IF should no longer be considered a variety of IF, sensu stricto.

It is generally agreed that none of the minerals in IF are primary in origin in the sense that the original seafloor precipitate was likely a water-rich gel that was not preserved. Instead, the observed minerals reflect significant post-depositional alteration under diagenetic and metamorphic conditions, including, in some cases, post-depositional fluid flow, particularly within oxidised and mineralised zones. The effect of increasing temperature and pressure is manifested by the progressive change in mineralogy through replacement and recrystallisation, increase in grain size, and obliteration of primary textures (Klein, 2005). Traditionally, iron oxides in IF are interpreted to have formed from an initial Fe(III)-oxyhydroxide phase, e.g., ferrihydrite, $Fe(OH)_3$, which precipitated in the photic zone from seawater via the oxidation of dissolved ferrous iron, Fe(II), at concentrations that may have ranged from 0.03 to 0.5 mM; Holland, 1973; Morris, 1993). By contrast, modern seawater typically has iron concentrations in the range of 0.05 to 2.0 nM (de Baar and de Jong, 2001). However, recent work suggests that in the presence of dissolved silica, the initial water column precipitate may have been a Fe(III)-Si gel (e.g., Percak-Dennett et al.,

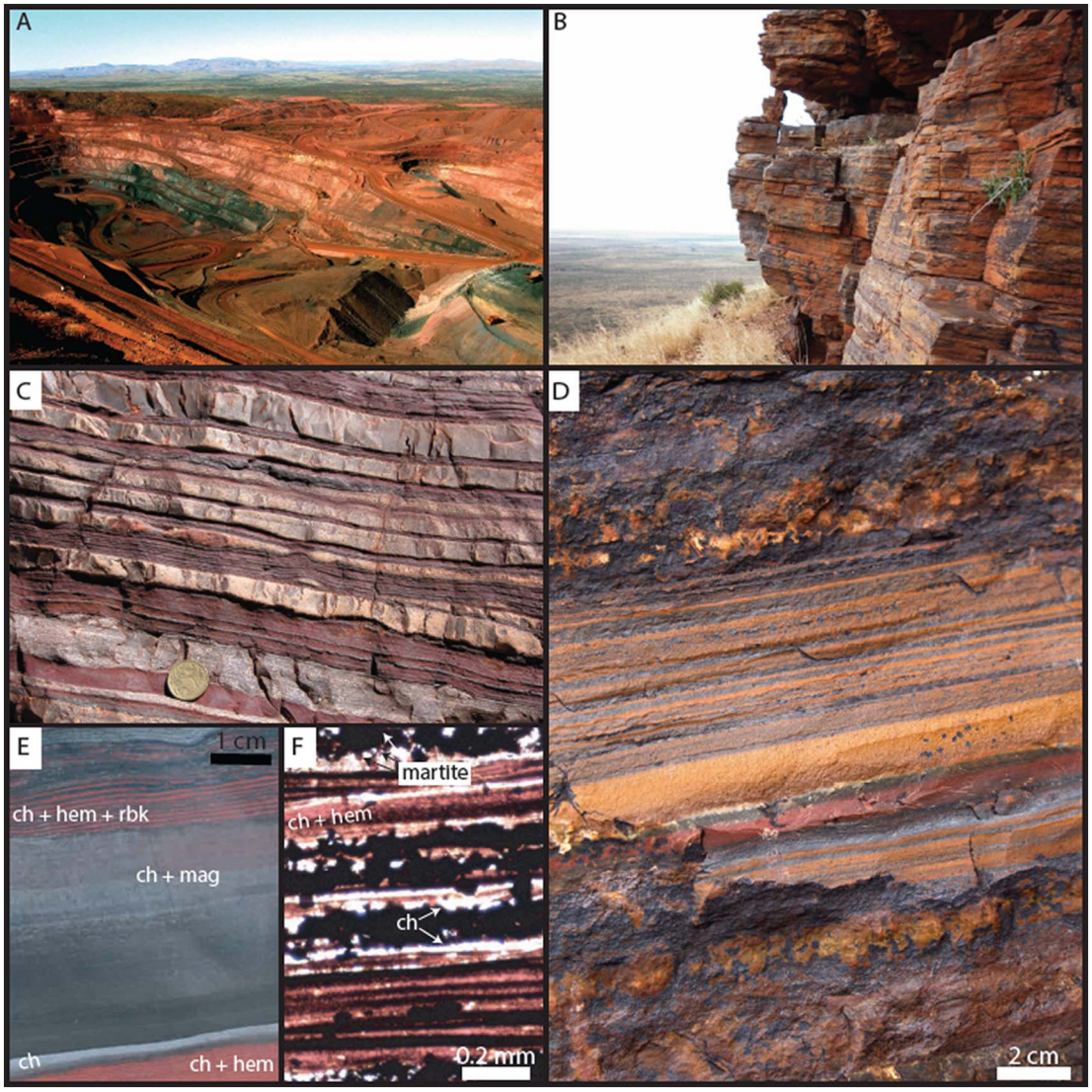

Fig. 3. Representative images of Paleoproterozoic BIF. (A) Aerial overview of the 2.48 Ga Dales Gorge Member along the southern ridge at Mt. Tom Price, Western Australia. (B) Field photograph of basal part of rhythmically banded 2.47 Ga Kuruman Formation BIF outcropping at Kuruman Kop locality. (C) Section of banding in 2.46 Ga Joffre Member, Western Australia. (D) Weathered Kuruman BIF showing distinct iron-rich and iron-poor (sub-)millimeter thick microbands. Field of view 20 cm in height. (E–F) Photos and photomicrographs illustrating main petrographic characteristics of oxide-facies BIF in Joffre BIF. (E) Core displays pale grey micro- and mesobands of alternating chert and magnetite, dark grey magnetite mesobands, and reddish and bluish (1 mm thin) microbands of chert–hematite–riebeckite. Field of view 5 cm in height. (F) Coarse- and fine-magnetite microbands with chert and very fine hematite. The latter likely is a product of secondary oxidation of magnetite. Note single grains of martite in upper left. Field of view 1 cm in height. Abbreviations: ch = chert, mag = magnetite, hem = hematite, rbk = riebeckite.

2011). During IF mineralisation, sinking of Fe(III)-silica particles to the seafloor eventually led to formation of (1) magnetite or iron carbonates when organic remineralisation was coupled to Fe(III) reduction, either during diagenesis or metamorphism; (2) hematite, through dewatering and silica release, assuming insufficient organic carbon for Fe(III) reduction; (3) iron silicates, possibly in the form of a precursor mineral, such as greenalite ($(Fe)_3Si_2O_5(OH)_4$), when silica sorbed onto or was incorporated in Fe(III)-oxyhydroxides reacted with other cationic species within sediment pore waters (Morris, 1993; Fischer and Knoll, 2009); and (4) precipitation of quartz through dehydration of opaline silica and/or Fe(III)-Si gels. Ferrous iron sorption to those particles may also have given rise to 'green rust'-type deposits that eventually transformed into magnetite or iron silicates (Tamaura et al., 1984; Zegeye et al., 2012; Halevy et al., 2017). Recently, greenalite has also been suggested as a primary precipitate that formed in the water column (Rasmussen et al., 2015, 2016, 2017); a more detailed discussion of the primary mineralogy of BIF is given below in Section 2.3, but we note here the consensus suggests that the primary mineral phase being a silica-associated Fe(III)-oxyhydroxide.

Organic material, whether in the form of pelagic rain or intimately associated with sinking Fe(III)-oxyhydroxide particles, would have fuelled the organic remineralisation reactions mentioned above, and is likely to have been largely consumed by excess Fe(III) oxidants during diagenesis and metamorphism (see Section 2.6). Although siderite in some IF has been interpreted to be a primary mineral phase (e.g., Beukes and Klein, 1990), there are strong isotopic and petrographic arguments that point instead to formation linked to the remineralisation of organic matter (e.g., Johnson et al., 2003, 2008a, 2008b; Fischer et al., 2009; Pecoits et al., 2009; Heimann et al., 2010; Johnson et al., 2013).

Chert is commonly considered to have precipitated from the water column or in sediment porewaters as colloidal silica co-precipitated with Fe(III)-oxyhydroxide particles, but it is also possible that chert formed through the dewatering of Fe(III)-Si gels. Similar to Fe(II), the Archaean ocean had significantly elevated concentrations of dissolved silica, at least as high as at saturation with cristobalite (0.67 mM at

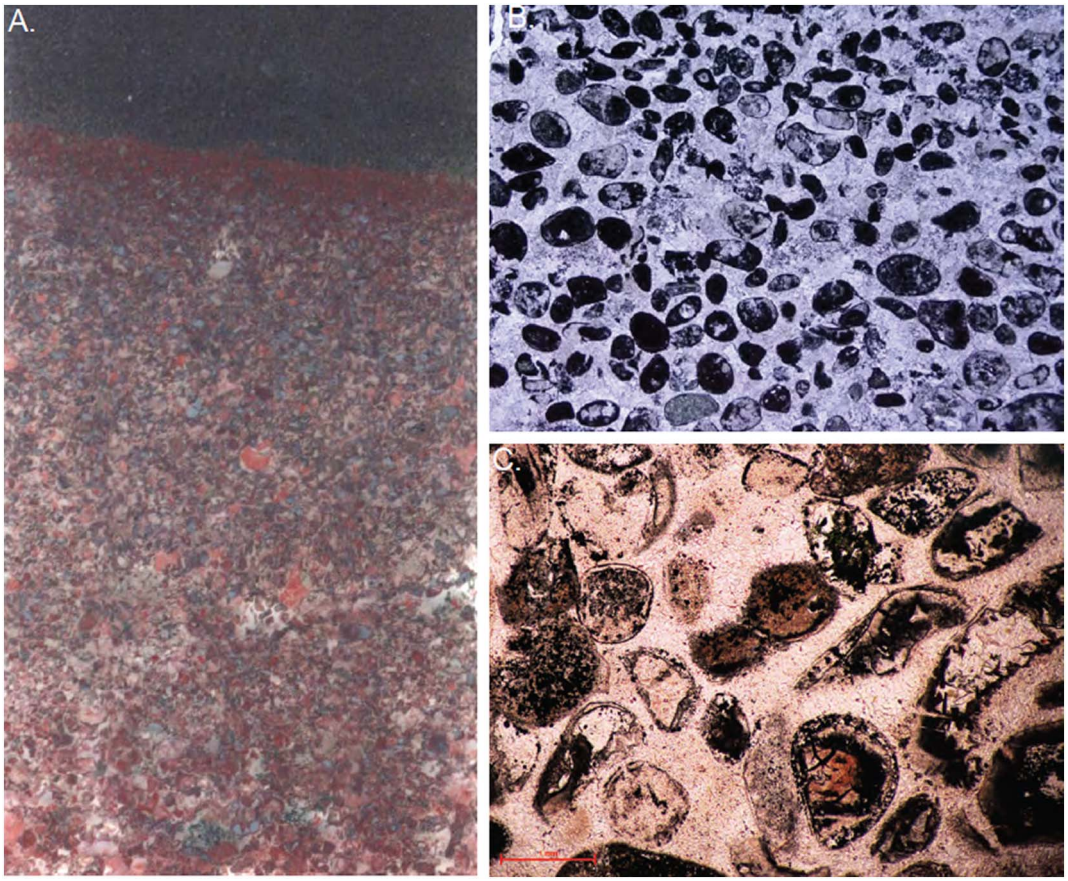

Fig. 4. (A–B) Middle Proterozoic GIF from 1.88 Ga Frere Formation, Earaheedy Group, Western Australia. (A) Graded bed comprising granules and ooids. Field of view is 2 cm in width. (B) Rounded granules comprising hematite, magnetite, chlorite, chert, and carbonate 'floating' in a matrix of carbonate cement. Field of view is 6 mm. (C) Thin section of 2.32 Ga GIF of Timeball Hill Formation, South Africa.

40 °C in seawater), between 0.5 and 1.5 mM for Fe(III)-Si gels, depending on the Fe/Si ratio, or as high as 2.20 mM for amorphous silica (Siever, 1992; Maliva et al., 2005; Konhauser et al., 2007a; Zheng et al., 2016). In contrast, modern seawater has dissolved silica typically < 0.10 mM (Tréguer et al., 1995), reflecting uptake by silica-secreting organisms. Alternative interpretations for the chert include formation (1) at the sediment-water interface as a replacement phase of a precursor sediment (Krapež et al., 2003), (2) within the sediment following desorption of silica that was adsorbed to the surface of Fe(III)-oxyhydroxides during the diagenetic reduction of Fe(III) by organic carbon (Fischer and Knoll, 2009), or (3) as a cement phase that infilled the pore spaces within primary iron-rich silicate muds (Rasmussen et al., 2015). Given the diversity of chert occurrences among different IF, these interpretations are not mutually exclusive.

2. What iron formations indicate about the Precambrian environment

2.1. Hydrothermal sources of iron to the oceans

The abundance of IFs in Precambrian successions and their absence in Phanerozoic successions was used in early studies to argue for a largely anoxic Precambrian atmosphere and ocean system (e.g., Cloud, 1973; Holland, 1973, 1984). The accumulation of such large masses of iron (in the form of Superior-type BIF) required the transport of dissolved Fe(II), because Fe(III) is essentially insoluble at circumneutral pH values. Early studies invoked a continental source of iron, where Fe(II) would have been mobile during weathering in the absence of atmospheric O_2 (e.g., James, 1954; Lepp and Goldich, 1964), as well as the expectation that early continents would have been more mafic than today, and hence richer in iron (Condie, 1993). However, detailed studies of IF that followed in the Hamersley Province, Western Australia, suggested that the amount of iron deposited was on the order of 1×10^{13} g/yr (Trendall and Blockley, 1970), requiring rivers the size of the modern Amazon to transport orders of magnitude more iron than they do today. Furthermore, IFs typically lack significant detrital input, which argued against a riverine source of the iron (Holland, 1978). Holland (1973) had previously suggested that the iron was instead sourced from deep-marine, hydrothermally influenced waters and supplied to the depositional settings via upwelling processes.

With the 1977 discovery of modern seafloor-hydrothermal systems (e.g., Corliss et al., 1978), the observed high flux of dissolved iron derived from slow-spreading mid-ocean ridges (e.g., Saito et al., 2013), and the recognition that even modern hydrothermal systems may contribute up to 75% of dissolved iron to the iron budget in the deep oceans (German et al., 2010; Carazzo et al., 2013; German and Seyfried, 2014), the interpretation that iron was sourced from the deep ocean became increasingly favoured. Moreover, it has been demonstrated that, even in the modern ocean, particulate and dissolved iron can be transported > 2000 km from the ridge axis in seafloor- hydrothermal settings (Fitzsimmons et al., 2017), and that variability in this input and ocean mixing regimes have influenced the extent of iron transport even in the more recent past (Horner et al., 2015). Along similar lines, it has also been proposed that dissolved iron could have been supplied directly by hydrothermal plumes to the uppermost levels of the water column. Archaean ridge crests were likely shallower than today (Isley, 1995), reflecting higher mantle temperatures, and under such conditions, hydrothermal effluent could have risen buoyantly upwards through the water column to the photic zone – where various oxidative mechanisms could have occurred (see Section 2.4). Although modern

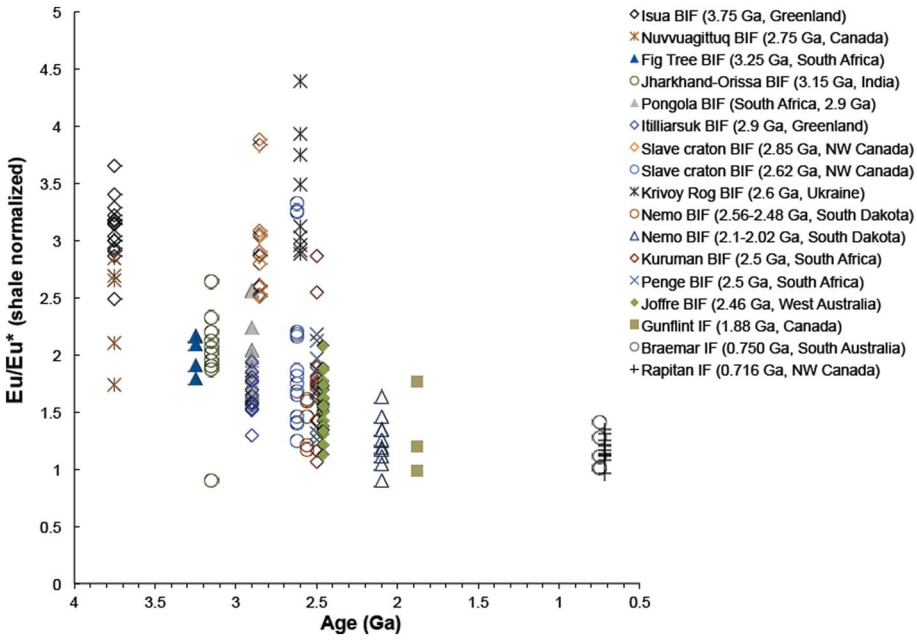

Fig. 5. PAAS-normalised (McLennan, 1989) Eu anomaly (Eu/Eu*) through time of some of the important IFs. Data for Isua from Frei and Polat (2007); Nuvvuagittuq from Mloszewska et al. (2012, 2013); Fig Tree from Derry and Jacobsen (1990) and Hofmann (2005); Jharkhand-Orissa from Bhattacharya et al. (2007); Pongola from Alexander et al. (2008); Itilliarsuk from Haugaard et al. (2013); Slave Craton from Haugaard et al. (2016a, 2017b); Krivoy Rog from Viehmann et al. (2015); Joffre from Haugaard et al. (2016b). Kuruman and Penge from Bau and Dulski (1996); Nemo from Frei et al. (2008); Gunflint from Danielson et al. (1992); Braemar from Lottermoser and Ashley (2000); Rapitan from Halverson et al. (2011).

hydrothermal Fe(II) input concentrations (1–3 nM) are significantly below what would be required to form an IF, this system provides evidence that the long-distance transport of iron and the formation of Superior type IF is mechanistically possible. This would especially be the case under less oxidising conditions, such as those predicted for the Archaean and Palaeoproterozoic, favouring dissolved Fe(II) transport over even longer distances than those observed today. Moreover, the elevated temperatures of water-rock reactions in the Archaean and the low concentration of marine sulfate (which affect the Eh of hydrothermal fluids, as well as limit near-vent precipitation of iron sulfides) suggest that dissolved Fe(II) in hydrothermal effluents may have been orders of magnitude greater than today (e.g., Kump and Seyfried, 2005). Indeed, the concentration of dissolved Fe(II) effused from some modern deep-sea vents is as high as 25 mM/kg; a few, in arc- and back-arc settings have as much as 2500 mM (German and Von Damm, 2003), highlighting the possibility that Archaean hydrothermal fluids could have been significantly enriched in dissolved Fe(II). Furthermore, the observation that Archaean shales are enriched in iron, relative to average Phanerozoic shales, may also indicate a larger hydrothermal flux of Fe(II) to the early oceans (Kump and Holland, 1992; Bekker and Holland, 2012), or greater delivery of iron-rich siliciclastic sediment due to the Archaean crust being more mafic (e.g., Dhuime et al., 2015; Lee et al., 2016).

Rare earth elements and yttrium (REE + Y) in hydrothermal fluids have characteristic distributions that provide additional evidence for a hydrothermal Fe(II) source for IFs, based on the assumption that their patterns record the source of iron due to high partition coefficients of the REEs onto hydrothermal precipitates (e.g., Koeppenkastrop and De Carlo, 1992). Modern seawater generally displays heavy REE (HREE) enrichments relative to light REE (LREE), as well as positive La, Gd, and Y anomalies, and strong negative Ce anomalies when normalised to shales (e.g., post-Archaean average shale - PAAS) (e.g., Elderfield and Greaves, 1982; Taylor and McLennan, 1985; de Baar et al., 1985; Derry and Jacobsen, 1990; Bau et al., 1995; Alibo and Nozaki, 1999; Bolhar et al., 2004; Planavsky et al., 2010a). These patterns are typically mimicked in the REE + Y patterns of post-Archaean IF (Laajoki, 1975; Fryer, 1977a, 1977b; Graf, 1978; Barrett et al., 1988; Klein and Beukes, 1989). Iron formations older than 2.5 Ga display positive La, Gd, and Y anomalies as well, but lack regular negative Ce anomalies and instead contain large positive Eu anomalies (e.g., Alexander et al., 2008). Estimates suggest that a 1:100 or 1:1000 mixture of modern seawater to hydrothermal fluid may account for the observed REE + Y patterns of IF (Barrett et al., 1988; Dymek and Klein, 1988; Klein and Beukes, 1989).

Recent in-situ and fraction-specific REE + Y trends for the ca. 2.47 Ga Kuruman and Griquatown IFs show a marked difference in carbonate versus oxide mineral-hosted REE + Y patterns (Oonk, 2017). The carbonate REE + Y patterns seem to mimic that of modern seawater even closer than do bulk-rock patterns. In addition, the changing steepness of the REE + Y spectra (Yb_{SN}/Ce_{SN}) could be related to corresponding changes in depth of deposition, as suggested for modern seawater (e.g., Piepgras and Jacobsen, 1992; Alibo and Nozaki, 1999). The oxide fraction is the most depleted in REE + Y and has a slight MREE enrichment (Oonk, 2017), which has been described from modern oxygen-limited ferrous environments (e.g., Haley et al., 2004).

Europium anomalies in REE + Y patterns have been central in tracing Fe sources. Europium enrichment in chemical sedimentary rocks that precipitated from seawater indicates a strong influence of high-temperature hydrothermal fluids on the seawater dissolved REE + Y load (e.g., Klinkhammer et al., 1983; Derry and Jacobsen, 1988, 1990; Bau and Dulski, 1996; Viehmann et al., 2015). Positive Eu anomalies in hydrothermal fluids are linked to the breakdown of plagioclase minerals within the volcanic rocks underlying hydrothermal vents, as plagioclase is intrinsically enriched in Eu relative to other REE + Y during igneous crystallisation (Schnetzler and Philpotts, 1970; Graf, 1977, 1978; Fryer et al., 1979). Furthermore, Eu remains in the soluble Eu^{2+} state in hydrothermal fluids because Eu^{2+} is more stable at higher temperatures (Sverjensky, 1984; Bau, 1991). It is generally assumed that Fe and REE + Y will not be fractionated during transport from spreading ridges or other exhalative centres, owing to the high sorption capacity of Fe(III)-oxyhydroxides; therefore, a large positive Eu anomaly (> 2) indicates that the Fe in the precursor sediment was hydrothermally derived (e.g., Michard and Albarède, 1986; Bau, 1991; Danielson et al., 1992; Slack et al., 2007, 2009). However, Eu concentrations can also be elevated by the erosion of Eu-enriched Archaean continental crust (Taylor and McLennan, 1985; Bolhar et al., 2004), and anomalies generated in vent systems may be diluted by mixing of seawater and hydrothermal fluids (Olivarez and Owen, 1991). Nonetheless, secular trends in the magnitude of Eu anomalies in large Superior-type IFs have historically been assumed to record variations in hydrothermal flux (e.g., Fryer, 1977a; Derry and Jacobsen, 1990; Danielson et al., 1992; Bau and Möller, 1993; Sreenivas and Murakami,

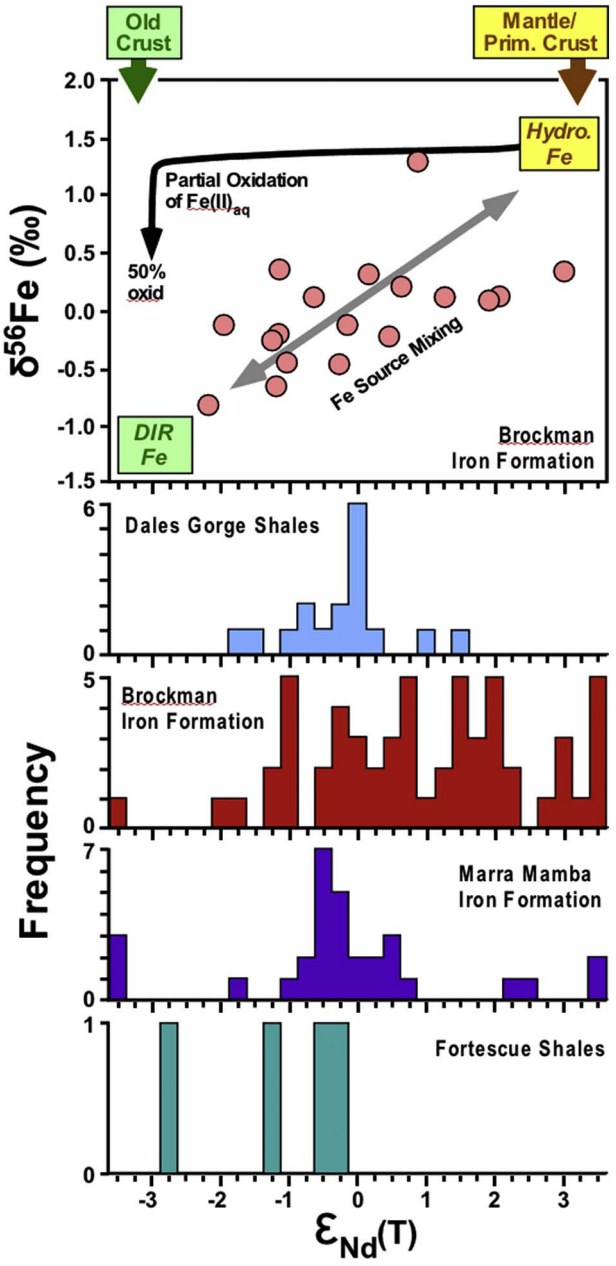

Fig. 6. Neodymium and Fe isotope data from Marra Mamba and Brockman IFs and associated shales of the Hamersley Basin, Western Australia. $\varepsilon_{Nd}(t)$ values for IFs scatter between mantle/primitive crust composition and those of old crust, indicating a mix of REE + Y sources. Intermediate $\varepsilon_{Nd}(t)$ values for associated shales indicate local continental crust may have near-zero $\varepsilon_{Nd}(t)$, which would increase the continental component of REE + Y relative to an assumed continental $\varepsilon_{Nd}(t)$ value of −3. Positive correlation between $\varepsilon_{Nd}(t)$ and $\delta^{56}Fe$ seen in 2.48 Ga Dales Gorge Member is interpreted to reflect mixing between a hydrothermal (high-$\varepsilon_{Nd}(t)$, high-$\delta^{56}Fe$) iron source and iron mobilized by a basinwide Fe shuttle via DIR on continental shelf.
Data sources: Jacobsen and Pimentel-Klose (1988a), Alibert and McCulloch (1993), W. Li et al. (2015) and C. Li et al. (2015).

2005; Viehmann et al., 2015). This trend is clearly demonstrated through a compilation of chondrite-normalised Eu anomaly data (Eu_{CN}/Eu_{CN^*}) in IF spanning the Precambrian (Fig. 5). The magnitude of positive Eu anomalies steadily decreases from the Eoarchaean, which reflects both high hydrothermal input and low dissolved oxygen required to stabilise Eu^{2+} for transport before the deep oceans became oxygenated (Viehmann et al., 2015). The very high peak between 2.7 and 2.5 Ga likely corresponds to a very high mantle input of hydrothermally-derived iron at that time.

Positive Y anomalies are typical of aqueous systems (Bau and Möller, 1993). Aqueous fluids and their precipitates display Y/Ho ratios significantly higher than the molar ratio of 52 shown by common igneous rocks and epiclastic sediments (Bau, 1996, and references therein), reaching molar ratios up to 90 (Zhang et al., 1994; Bau et al., 1997; Nozaki et al., 1997). The Y/Ho ratio in chemical precipitates is also typically depressed by clastic input because crustal rocks have lower Y/Ho ratios (Kamber and Webb, 2001; Bolhar et al., 2004). Similarly, Viehmann et al. (2015) noted the depression of the La anomaly in IF with increased detrital contamination; La anomalies are strongly expressed in pure IF (La_{SN}/La_{SN^*} ratios between 1.32 and 1.80), whereas they are small or absent in impure IF (between 0.85 and 1.52). Detrital contamination would also act to decrease the slope of the REE + Y pattern. Typically, HREE are enriched in the oxide facies of IF, as the result of interaction between hydrothermal fluids and mid-ocean ridge basalt (MORB) at spreading centres, which are typically tholeiitic and depleted in LREE (Derry and Jacobsen, 1990; Bau, 1991).

Sources of REE + Y and the fidelity of their signals have been investigated using the ^{138}La-^{138}Ce and ^{147}Sm-^{143}Nd isotope systems (e.g., Tanaka et al., 1982; Derry and Jacobsen, 1990; Shimizu et al., 1991; Hayashi et al., 2004; Viehmann et al., 2015; Haugaard et al., 2016a, 2016b). Both Ce and Nd have short residence times in the modern ocean, 90–165 and 1000–1500 years, respectively (Amakawa et al., 1996), and in the Archaean oceans these elements likely had a similar residence times on the order of 10^3 years, suggesting that Ce and Nd isotope compositions would be spatially heterogeneous. In the Archaean and Proterozoic oceans, $\varepsilon_{Nd}(t)$ values (which describe the deviation of the $^{143}Nd/^{144}Nd$ ratio measured in a sample relative to the $^{143}Nd/^{144}Nd$ ratio in a chondritic uniform reservoir at time t and in parts per 10^4) are estimated to have been +1 to +2 for deep waters dominated by hydrothermal sources, whereas values down to −3 would have been typical of shallow-waters dominated by terrestrial sources (Miller and O'Nions, 1985; Jacobsen and Pimentel-Klose, 1988a, 1988b; Alexander et al., 2008). The relative contribution of continentally-sourced versus mantle-sourced REE + Y, discussed in more detail in the next section, has been estimated using Ce and Nd isotope compositions (Piepgras and Wasserburg, 1980; Bau et al., 1997; Shimizu et al., 1990, 1991; Alexander et al., 2008, 2009; Viehmann et al., 2015). In some cases, ^{138}La-^{138}Ce systematics show that Ce anomalies in IFs are a feature produced by recent hydrothermal events and are not intrinsic to ancient seawater (Hayashi et al., 2004). Similarly, young ^{147}Sm-^{143}Nd isotope ages indicate post-depositional REE + Y mobility during metamorphic events (e.g., Shimizu et al., 1990). Such results highlight the need to consider the possibility of post-depositional REE + Y mobility in some IFs, particularly those that have been subjected to metamorphic and supergene alteration.

Building on the premise of a hydrothermal iron source, Isley and Abbott (1999) suggested a direct link between mantle plume activity between 3.8 and 1.8 Ga and global IF deposition. It is now widely accepted that the deposition of large, economically important IF coincided in time with mantle plume breakout events, as recorded by the secular distribution of large igneous provinces (LIPs), dike swarms, and submarine-emplaced mafic volcanic rocks (e.g., Isley and Abbott, 1999; Rasmussen et al., 2012), as well as that of major mantle plume events (Viehmann et al., 2015). LIPs are linked to relatively short-lived (< 10–20 Myr) igneous events with magma having been produced in the mantle, resulting in relatively rapid intrusion and eruption of high volumes of mafic to ultramafic magma (Coffin and Eldholm, 1994; Ernst and Buchan, 2001). Greater oceanic spreading rates, increased submarine and subaerial volcanic activity, high sea-level, greenhouse conditions, and an enhanced production of VMS are all consequences of mantle plume breakout events (e.g., Condie et al., 2001; Barley et al., 1997, 2005; Bekker et al., 2010, 2014).

2.2. Continental sources of iron to the oceans

Compilations of Nd isotope data from Archaean to Palaeoproterozoic IFs highlight the fact that most IFs have $\varepsilon_{Nd}(t)$ values that are intermediate between those of the depleted mantle and ancient continental crust (Alexander et al., 2009; Viehmann et al., 2015). Assuming that the sources of REE + Y closely track the sources of Fe(II), Nd isotope data for IFs suggest a significant contribution from "continental" iron (Haugaard et al., 2013; W. Li et al., 2015). Based on Nd-Fe isotope variations in the ca. 2.5 Ga Brockman Iron Formation (Fig. 6), W. Li et al. (2015) modelled the mixing between a hydrothermal Fe(II) source (high δ^{56}Fe, $\varepsilon_{Nd}(t)$) and a continental Fe(II) source (low δ^{56}Fe, $\varepsilon_{Nd}(t)$). The high δ^{56}Fe values of the hydrothermal source are interpreted to reflect partial oxidation of hydrothermally-derived Fe (II), whereas the low δ^{56}Fe values of the continental source are attributed to microbial dissimilatory iron reduction (DIR) that released dissolved Fe(II) from pore fluids in continental margin sediments that was transported to the deep basin. Basin-wide transport of DIR-generated dissolved Fe(II) has been referred to as a "benthic iron shuttle" (Anderson and Raiswell, 2004), and has been inferred to have occurred in Archaean and Proterozoic basins (Severmann et al., 2008).

A benthic iron shuttle predicts that proximal sediments should have relatively high δ^{56}Fe values, reflecting the residual iron pool after export of low-δ^{56}Fe dissolved Fe(II). Support for this model comes from the Kuruman Iron Formation, where near-shore samples have consistently higher δ^{56}Fe values than more distal samples (Heimann et al., 2010). In terms of the Brockman Iron Formation, which is correlative with the Kuruman Iron Formation (Beukes and Gutzmer, 2008), the observed co-variations in δ^{56}Fe - $\varepsilon_{Nd}(t)$ values (Fig. 6) lends itself to differing interpretations, even among the co-authors. On the one hand, the scatter in the data might indicate that REEs and Fe isotopes are decoupled, and hence, given the range of potential Fe and REE pathways and variable basin geometry, the relations in Fig. 6 do not necessarily support a mixture of hydrothermal and benthic Fe sources. On the other hand, some scatter is expected given the range in δ^{56}Fe values for the hydrothermal component (recording differing extents of oxidation), and the range in $\varepsilon_{Nd}(t)$ values for the continental endmember, and perhaps the focus of interpretation is the fact that the observed data do not lie near the "L-shaped" trend that is required by a strictly hydrothermal model, such as that proposed by Rouxel et al. (2005), who argued that the negative δ^{56}Fe values of IFs reflect a residual iron component after extensive oxidation.

The broader database of Nd isotope compositions reported from the Hamersley Basin (Jacobsen and Pimentel-Klose, 1988a; Alibert and McCulloch, 1993; W. Li et al., 2015; C. Li et al., 2015) indicates that both the 2.60 Ga Marra Mamba and Brockman IFs contain a mixture of hydrothermally- and continentally-derived Nd. Although most studies assume that the continental component has a highly negative $\varepsilon_{Nd}(t)$ value, this assumption is only valid if the continental crust is significantly older than the depositional age of the IFs. Primitive orogenic crust derived from the mantle would have $\varepsilon_{Nd}(t)$ values that are similar to those of the mantle. $\varepsilon_{Nd}(t)$ values for shales that are coeval with IFs in the Hamersley Basin indicate that at least one continental endmember has near-zero or only slightly negative $\varepsilon_{Nd}(t)$ values (Fig. 6), suggesting the presence of continental crust that is only slightly older than the depositional age of IFs. These relations indicate, therefore, that the continental component in IFs may be underestimated if that component is only slightly older than the depositional age of the IF.

2.3. Plausible primary iron mineralogy

Iron formations are defined by their unusual mineralogy, where silica and a wide range of iron-rich (but aluminium-poor) minerals constitute the majority. The notion that some of the Fe(III) mineral phases (hematite, magnetite) are the primary precursor phase for IF was suggested over four decades ago. Ayres (1972) documented the presence of possible original granular textures, including microspheres of 5–15 μm in diameter, in several of the hematite-rich mesobands of the Dales Gorge Member. Also present within the hematite layers are chert globules containing hematite inclusions. Trendall and Blockley (1970) reported "jaspery platelets" of hematite (2–10 μm in diameter) within chert that they argued was paragenetically the oldest of the hematite grains observed in the Dales Gorge Member. Ahn and Buseck (1990) observed 120–200 nm hematite nanospheres in the underlying Marra Mamba Formation, which they attributed to structural ordering that accompanied dehydration of colloidal Fe(III) oxyhydroxide particles. These spheroids are similar to hematite spheroids found in the Quaternary hydrothermal fields of Milos Island in Greece (Chi Fru et al., 2013) and in modern iron oxide deposits of the Red Sea (Taitel-Goldman and Singer, 2002), and may record early diagenetic transformations of original Fe(III)-oxyhydroxide particles. In their review of IF genesis, Beukes and Gutzmer (2008) stressed that the earliest oxide mineral in Superior-type IFs was fine-grained hematite dispersed throughout the chert. An early paragenesis for hematite is supported by the recent study of Sun et al. (2015), who conducted high-resolution transmission electron microscopy (TEM) and selected area electron diffraction (SAED) analyses to ascertain the timing and paragenesis of hematite within IF from the 2.73 Ga Abitibi greenstone belt in northeastern Canada and the Kuruman Iron Formation. Those authors interpreted the 3–5 nm ultrafine hematite crystals in the hematite bands, as well as submicrometer (sub)euhedral hematite crystals randomly distributed in the chert matrix of transitional zones between iron oxide- and chert-rich bands, to have formed directly by dehydration from a precursor Fe(III)-oxyhydroxide phase.

Although the case for primary hematite discussed above is strong in some examples, hematite in IFs is typically secondary in origin, linked with iron enrichment leading to ore genesis, even in sections distal to iron ore bodies. Iron formations that contain hematite and martite-goethite are some of the largest known ore bodies. Their origin remains controversial, but hydrothermal processes are well documented (Taylor et al., 2001; Thorne et al., 2009). Ore hematite is typically prismatic or platy, and commonly occurs with bladed carbonate minerals, indicating late-stage carbonate recrystallisation, in contrast to finer-grained hematite that characterises occurrences distal to ore. Interpretation of platy hematite as depositionally or diagenetically early is suspect, however, because such a morphology is the typical form of ore-generation hematite. Indeed, geochronological studies of xenotime and monazite paragenesis within hematite and martite-goethite ore bodies that formed during hydrothermal alteration of IF indicate that iron-ore formation was a long-lived and multi-stage process (Rasmussen et al., 2007). Within the iron ore bodies of the Hamersley Province, hematite-carbonate alteration occurred at temperatures of ~250 °C under high fluid pressures (Taylor et al., 2001).

Silica concentrations in Precambrian seawater are estimated to have been high (~1 to 2 mM), assuming control by the solubility of amorphous silica and sorption to silicate minerals (Maliva et al., 2005), raising the possibility that the primary Fe(III) minerals were enriched in SiO_2. Percak-Dennett et al. (2011) and Wu et al. (2012) studied dissolved Fe(II) oxidation in the presence of dissolved silica, which produced an Fe(III)-Si gel that was homogenous on the nm scale, indicating the presence of a single phase in which Si and Fe are tightly bonded and distinct from, for example, Si sorbed to ferrihydrite, as has been previously described from terrestrial hot springs (e.g., Lalonde et al., 2007). Previous spectroscopic studies indicate that co-precipitation of Fe(III) and Si from a mixed solution tends to form an intimately bonded Fe(III)–Si phase, rather than separate Fe(III) and Si phases (Doelsch et al., 2000, 2001, 2003). Identifying the specific primary Fe(III) precipitate in IFs is important, because when exposed to dissolved Fe(II), Fe(III)-Si gels are resistant to phase transformations that may occur in dissolved Fe(II)-ferrihydrite experiments (e.g., Johnson et al., 2005), and uptake of Fe(II) into the solid is inhibited under abiological conditions (Zheng et al., 2016).

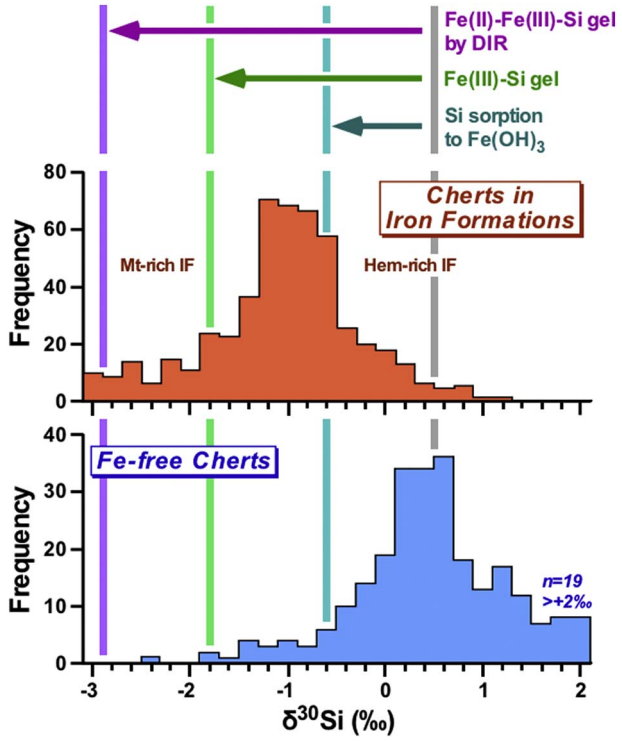

Fig. 7. Histograms of Si isotope compositions for Precambrian cherts in IFs, as well as Fe-free cherts. Also shown are Si isotope fractionation factors for Si sorption onto Fe(III)-oxyhydroxides (Delstanche et al., 2009), Fe(III)-Si gels (Zheng et al., 2016), and mixed Fe (II)-Fe(III)-Si gels produced by DIR (Reddy et al., 2016), referenced to the average δ^{30}Si value of Fe-free chert. Lower δ^{30}Si values of IF cherts cannot be explained solely by Si sorption to Fe(III)-oxyhydroxides, but likely involves Fe(III)-Si gels as the primary phase. As discussed in Reddy et al. (2016), magnetite-rich IFs have lower δ^{30}Si values than hematite-rich IFs; measured Si isotope fractionations suggest production of magnetite-quartz assemblages that have very low δ^{30}Si values through DIR.
Data sources: André et al. (2006), Robert and Chaussidon (2006), van den Boorn et al. (2007, 2010), Delvigne et al. (2012), Steinhofel et al. (2009, 2010), Abraham et al. (2011), Heck et al. (2011), Chakrabarti et al. (2012), Li et al. (2014), Geilert et al. (2014), Stefurak et al. (2015), Ding et al. (2017).

New research on Si isotopes provides insight into the primary solid phase of Fe(III) in IF genesis due to the strong control that Fe—Si bonding exerts on Si isotope fractionations. δ^{30}Si values for Precambrian cherts, including those associated with IFs, vary by ~7‰, and broad secular trends of increasing δ^{30}Si with decreasing age have been attributed to decreasing ocean temperature (Robert and Chaussidon, 2006), although this proposal has been difficult to test owing to the lack of experimental determination of Si isotope fractionation factors. A recent review of the Si isotope record has highlighted the fact that δ^{30}Si values for IFs are systematically lower than those of similar-aged cherts that are not associated with IFs (Marin-Carbonne et al., 2014), which is ascribed to the effects of Si sorption to Fe(III)-oxyhydroxides (Delstanche et al., 2009). Recent experimental studies, however, document large Si isotope fractionations between dissolved Si and Fe(III)-Si gel, significantly larger than those produced by sorption of dissolved Si to Fe(III)-oxyhydroxides (Zheng et al., 2016), thus providing an explanation for the highly negative δ^{30}Si values observed in some IF cherts (Fig. 7). Such observations strongly support the idea that the primary Fe(III) precipitate in IFs was an Fe(III)-Si gel. Moreover, Reddy et al. (2016) found that even larger Si isotope fractionations occur upon microbial reduction of Fe(III)-Si gels, which may explain the tendency of magnetite-rich IFs to have lower δ^{30}Si values than hematite-rich IFs (Fig. 7).

The paragenesis of magnetite in IFs is quite variable. Formation through dewatering of primary $Fe(OH)_2$ and $Fe(OH)_3$ precipitates has been proposed as the origin of disseminated fine-grained magnetite (Klein, 2005), but most workers consider magnetite to have formed through diagenetic and metamorphic reactions and there is in cases compelling petrographic evidence for a metamorphic origin (see below). In the case of diagenesis, Y.-L. Li et al. (2013) proposed a biological model to account for its formation via a three-stage sequence, beginning with magnetite formation by DIR within an initial ferrihydrite-rich sediment, coupled to the oxidation of lysed phytoplankton biomass. DIR was followed by magnetite crystal aging, and ultimately pressure–temperature-induced abiotic growth of the pre-existing biogenic magnetite during metamorphism. In support of the notion that magnetite nucleated during diagenesis, Li et al. (2011) conducted detailed crystallochemical analysis of magnetite from the Dales Gorge Member and reported a lattice constant and Fe^{2+}/Fe^{3+} stoichiometry very similar to those produced by DIR bacteria including *Geobacter*, *Shewanella*, and *Thermoanaerobacter*. Interestingly, Halama et al. (2016) experimentally simulated the metamorphism of precursor and diagenetic iron-rich minerals (ferrihydrite, goethite, hematite) under low-grade metamorphic conditions (170 °C, 1.2 kbar) for 14 days, and showed that thermochemical magnetite formation was limited to samples containing ferrihydrite and glucose, or goethite and glucose. No magnetite was formed from Fe(III) minerals when microbial biomass was present as the carbon and electron sources for thermochemical Fe(III) reduction, suggesting that biomass-derived organic molecules were bound to the mineral surfaces and prevented, or at least inhibited, solid-state conversion of ferric iron phases to magnetite.

Petrographic evidence certainly implies a secondary origin for magnetite in IFs (Ewers and Morris, 1981). Magnetite is a common replacement or overgrowth of early hematite and siderite, and of most rhombic, iron-rich carbonate. For instance, Krapež et al. (2003) reported several forms of diagenetic and metamorphic magnetite, including (1) disseminated grains within, but obscuring, sedimentary laminae; (2) laminated beds that clearly truncate sedimentary layering; (3) layer-discordant veins; and (4) infilling of cleavage. Ayres (1972) reported that magnetite euhedra pre-date rhombic carbonate, but post-date matrix chert. In contrast, laminated bands of magnetite can post-date burial stylolites and destroy primary layering; Krapež et al. (2003) referred to such laminated bands as iron proto-ore. Discordant veins, laminae, and cleavage fillings of magnetite cut these bands. Beukes and Gutzmer (2008) documented the occurrence of magnetite as a replacement of hematite-chert pods, and proposed formation through the addition of $Fe(II)_{aq}$ to ferrihydrite. Finally, magnetite is a common ore mineral, showing preserved transformations from proto-ore to ore magnetite, ore hematite to ore magnetite, and ore magnetite to ore hematite.

The genetic relations between hematite and magnetite in IFs are well traced using O and Fe isotope compositions (Fig. 8). Bulk mineral separates of hematite, magnetite, and quartz from the Dales Gorge Member have average δ^{18}O values of ~ −2‰, ~ +3‰, and ~ +21‰, respectively, which produces quartz-hematite and quartz-magnetite $^{18}O/^{16}O$ fractionations of ~ +23‰ and +18‰, respectively, indicating that on average, hematite formed at a lower temperature than magnetite (Becker and Clayton, 1976). In situ oxygen isotope analysis, however, indicates significantly larger ranges in δ^{18}O values, which correlate with petrographic relationships and chemical compositions (Li et al., 2013a). Fine-grained and dispersed hematite, considered to reflect the earliest generation, have δ^{18}O values as low as −9‰ as determined by in situ analysis, indicating formation temperatures as low as ~25 °C (Fig. 8). The earliest generation of magnetite in the Dales Gorge Member contains minimal Si content (Huberty et al., 2012), and in situ analysis shows that this magnetite has δ^{18}O values of ca. −6 to +4‰, indicating formation temperatures between ~50 °C and ~100 °C (Fig. 8). This is consistent with an early diagenetic origin for the low-Si magnetite. Significantly higher δ^{18}O values observed for Si-bearing magnetite, as well as for coarse, euhedral magnetite, indicate higher formation temperatures up to ~250 °C (Fig. 8). As discussed in Li et al. (2013a), the very low diffusivity of oxygen in

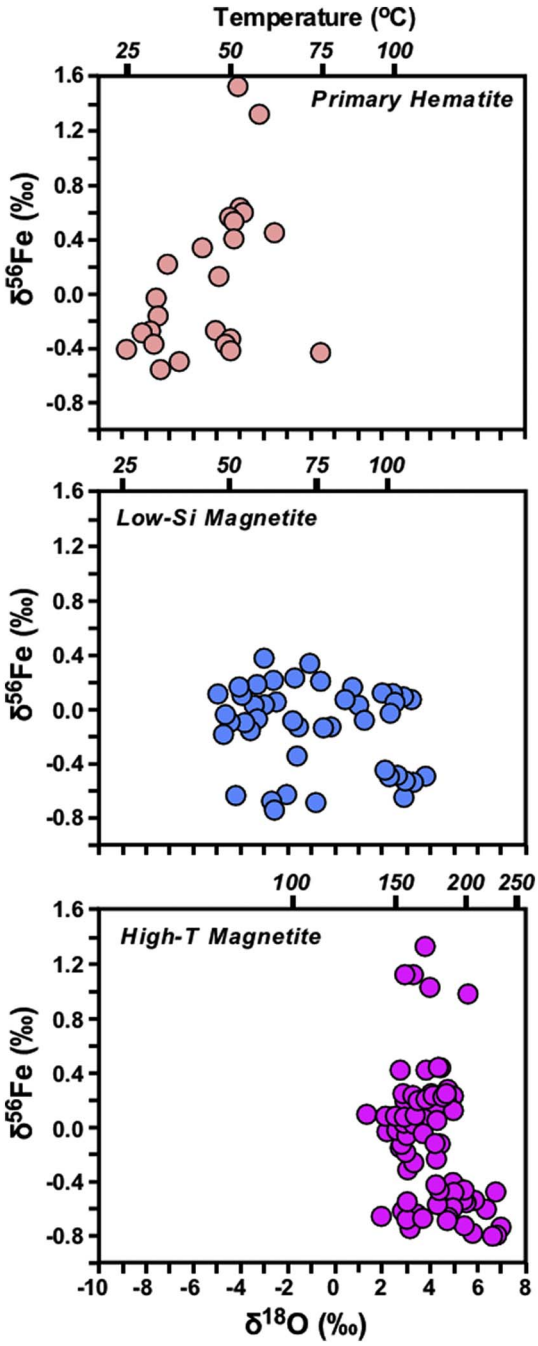

Fig. 8. Iron-O isotope variations in coexisting hematite and magnetite from the Dales Gorge Member. Earliest magnetite is recorded in magnetite that is fine-grained and has low Si contents, whereas high-temperature magnetite is coarse-grained and/or contains high levels of Si (Huberty et al., 2012). Oxygen isotope temperatures were obtained using hematite-quartz and magnetite-quartz fractionations; those for high-temperature magnetite use the average measured $\delta^{18}O$ value for quartz ($\delta^{18}O \sim +21‰$), reflecting the last equilibration of quartz during metamorphism, whereas low-temperature magnetite and hematite assumes a $\delta^{18}O$ value for quartz of +23‰ (see discussion in Li et al., 2013a). Oxygen isotope fractionation factors are from Kita et al. (1985), Mandernack et al. (1999), and Bao and Koch (1999).

hematite makes this mineral relatively resistant to post-formation oxygen isotope exchange with fluids or quartz, whereas magnetite and quartz will more readily exchange with each other, or with a fluid, at elevated temperatures.

In contrast to the systematic changes in $\delta^{18}O$ values with increasing formation temperature for hematite and magnetite, $\delta^{56}Fe$ values should remain relatively unchanged due to the low solubility of iron in aqueous solutions at hydrothermal temperatures (Chou and Eugster, 1977; Simon et al., 2004), slow diffusion of Fe in hematite and magnetite (Hallstrom et al., 2011), and lack of a large external reservoir for equilibration, in contrast to quartz for oxygen isotope exchange. The spread in $\delta^{56}Fe$ values for hematite and magnetite, as determined by in situ methods, is therefore likely to record original values upon increase in temperature (Li et al., 2013a), allowing inferences to be made regarding the sources of iron (e.g., hydrothermal versus DIR; Fig. 8).

Iron-bearing carbonates, which we broadly refer to as "siderite" are the most common carbonate minerals in IF, and include carbonates along the magnesite-siderite ($MgCO_3$-$FeCO_3$) and dolomite-ankerite ($Ca_{0.5}Mg_{0.5}CO_3$-$Ca_{0.5}Fe_{0.5}CO_3$) solid-solution series; the former having an average composition of $Mg_{0.2}Fe_{0.8}CO_3$ (Klein, 2005). Siderite typically occurs as minute, single rhomb-shaped crystals or massive layers of microcrystalline aggregates (James, 1951; Trendall and Blockley, 1970; Ayres, 1972). In some beds, siderite may constitute > 50% of the rock, and such occurrences are often classified as "siderite facies IF". Small siderite nodules are common in some layers, where they display evidence of differential compaction, thus indicating that the nodules probably formed prior to deep burial. The texturally earliest siderite is present as minute (< 20 μm) spheroids, which occur in some IFs and intercalated mudstones from the Hamersley Province (Ayres, 1972). The siderite appears to have replaced or overgrown an earlier phase (e.g., ferric oxyhydroxides), which occurs in the core of some crystals. Consistent with this suggestion, it has been shown that in the 1.88 Ga Gunflint Iron Formation in Ontario (Canada) some siderite rhombohedra contain spheres in their cores and a clear progression exists from siderite spheres to siderite rhombohedra without any trace of spheres remaining (LaBerge et al., 1987; Carrigan and Cameron, 1991). This progression was also found in the Dales Gorge Member, where siderite spheres and rhombohedra occur near each other. Such features suggest that some siderite formed during the diagenetic (biological or non-biological), and subsequent metamorphic, oxidation of microbial biomass to CO_2/bicarbonate coupled to the reduction of Fe(III), followed by reaction of the product Fe^{2+}_{aq} with sediment pore-water bicarbonate (Johnson et al., 2008a, 2008b; Heimann et al., 2010; Köhler et al., 2013; Halama et al., 2016). Importantly, in most cases, the C, O, Fe, and Sr isotope compositions of IF carbonates clearly preclude formation in equilibrium with seawater (Johnson et al., 2013). With that said, although petrographically most siderite (and ankerite) exhibit recrystallised and, therefore, apparently secondary textures, their geochemistry does indicate that some potentially "primary" signals can be retained in IF carbonates. Iron isotopes of extracted carbonate fraction remained unaffected by low-grade metamorphism (Frost et al., 2007) and carbonate-specific REE + Y patterns, both in situ (Alibert, 2016) and extracted as bulk (Oonk, 2017), mimic REE + Y aspects of present-day seawater.

Despite the consensus among workers that the precursor phase during the sedimentation of IF was most likely Fe(III)-oxyhydroxides (e.g., Konhauser et al., 2002; Kappler et al., 2005; Posth et al., 2014; Sun et al., 2015) or an Fe(III)-Si gel (e.g., Percak-Dennett et al., 2011; Zheng et al., 2016), there is renewed interest in possible alternative phases that may have influenced or been important for IF sedimentation. These alternative authigenic phases include dominantly Fe(II) or mixed-valence phases, such as greenalite and various "green-rust" phases.

The possible significance of greenalite versus other Fe(II) phases has been discussed previously (Eugster and Chou, 1973). Greenalite has been identified in chert layers from several Palaeoproterozoic IFs, including the Brockman Iron Formation in Western Australia (Kaufman et al., 1990; Rasmussen et al., 2015, 2016) and the Transvaal Supergroup in South Africa (Rasmussen et al., 2017). The identification of fine-grained greenalite nanoparticles in laminated cherts (Rasmussen et al., 2016, 2017) has been taken as evidence for water column precipitation of this mineral, and by extrapolation, as a critical precursor to hematite and magnetite. However, at least in the case of the

nanoparticles examined by Rasmussen et al. (2017), the succession examined more likely represents distal deep-water deposits not characteristic of IF deposited on a shelf. Moreover, ascribing a precursor phase containing significant ferrous iron requires a post-depositional mechanism to convert the Fe(II) on a layer-by-layer basis to Fe(III). Rasmussen et al. (2014) have argued that this oxidation, in the case of the Dales Gorge Member, occurred in association with a major collisional event at ca. 2.2 Ga when oxygenated and heated groundwaters (> 200–400 °C) migrated along sedimentary layers of pre-existing IF sediment (Rasmussen et al., 2005). Such an interpretation, however, is in conflict with the very low $\delta^{18}O$ values measured for hematite in the Dales Gorge Member (Fig. 8), which requires a very low temperature of formation. Late-stage oxidation also conflicts with the paragenetic sequence of oxides outlined by Huberty et al. (2012) for the Dales Gorge Member, which relies on the temperature-dependence of Si substitution. Although it is clear that oxygenated groundwaters may produce hematite mineralisation in ore zones (McLellan et al., 2004), the evidence does not support this mechanism for all hematite in the Dales Gorge Member. Finally, the laboratory experiments by Tosca et al. (2016), who examined the solubility of freshly precipitated greenalite suggest that its precipitation requires a pH of 7.75–8.3, values that are at odds with those predicted for Archaean seawater (e.g., Grotzinger and Kasting, 1993; Blättler et al., 2016; Halevy and Bachan, 2017). However, it is important to note that porewater pH in systems dominated by DIR will be in the range expected for greenalite precipitation, and that the petrographic evidence outlined above could also be consistent with early diagenetic precipitation of greenalite.

Carbonated green-rust has been observed in modern ferruginous and sulfate-poor Lake Matano in Indonesia (Zegeye et al., 2012), an environment proposed to be an analogue for the Archaean ocean (Crowe et al., 2008), and it is possible that green-rust was a precursor to magnetite in IFs. In Lake Matano, nanoparticle clusters of ferrihydrite or nanogoethite form at the redoxcline; while at 10–15 m below the redoxcline, small hexagonal plates that are characteristic of green-rust or fougerite were observed. Zegeye et al. (2012) attributed the formation of the green-rust phase to one of several possible pathways, including: (1) direct precipitation from a supersaturated water column, (2) as a microbial by-product of either photoferrotrophy or DIR, or (3) due to the interaction between aqueous Fe^{2+} and the surface of ferrihydrite below the redoxcline. Regardless of the mechanism, Zegeye et al. (2012) demonstrated that green-rust can be found within a naturally stratified water column, and that it may act as an important transitory phase between the redoxcline and the export of iron phases to the sediment. Thermodynamic calculations and precipitation experiments by Halevy et al. (2017) support carbonated “green-rust” as a possible phase given the appropriate Eh-pH conditions. Those authors further suggested that green-rust may have been an important factor in Archaean IF deposition before the Great Oxidation Event (GOE) – the time in Earth's history ca. 2.45 Ga when the atmosphere first became oxygenated (see Lyons et al., 2014) - and the subsequent dominance of ferrihydrite as the precursor phase to IF. It is unknown, however, whether such a conclusion may change in the presence of high concentrations of dissolved Si. Critically, green-rust phases are of mixed valence (e.g., Rickard and Luther, 2007), and accordingly, require a source of Fe(III). For instance, Etique et al. (2015) demonstrated that green rust might be the product of a bacterially mediated reaction involving Fe(III)-reducing bacteria and magnetite. In experiments conducted by Li et al. (2017), the authors reacted natural ferrihydrite-encrusted bacterial mats with dissolved Fe(II) and showed that hexagonal platelets of a siliceous green-rust phase formed, which then agglomerated into aggregates. The latter dissolved within hours and re-precipitated as ultrafine crystals of magnetite tens of nm in size, similar to the structure made of magnetite nanoparticles produced in previous mineral synthetic experiments (e.g., Guan et al., 2009). An argument against a green-rust precursor to BIF magnetite, however, is found in the Fe isotope composition of the Dales Gorge Member (Fig. 8), where the positive $\delta^{56}Fe$ values cannot be explained using the $^{56}Fe/^{54}Fe$ fractionation of ca. −0.2‰ measured between $Fe(II)_{aq}$ and green-rust (Wiesli et al., 2004). Nevertheless, the possibility of green-rust as a precursor precipitate for IFs remains a subject of interest.

2.4. Available oxidants in seawater for Fe(II) oxidation

The mineralogy and Fe isotope composition of IF dictates that some oxidation of Fe(II) was necessary for precipitation, yet which mechanism(s) were dominant remains uncertain. Prior to the rise of atmospheric oxygen and the development of a protective ozone layer, Earth's surface would have been subjected to high levels of ultraviolet radiation. Ocean waters at this time were anoxic and could have supported high concentrations of dissolved Fe(II). Under such conditions, dissolved ferrous iron species, such as Fe^{2+} or $Fe(OH)^{+}$, absorb radiation in the 200–400 nm range, leading to the photochemical formation of dissolved ferric iron [reaction 1], which in turn, hydrolyses to form Fe(III)-oxyhydroxides at circumneutral pH (Cairns-Smith, 1978; Braterman et al., 1983; Anbar and Holland, 1992).

$$2Fe^{2+}_{(aq)} + 2H^{+} + h\nu \rightarrow 2Fe^{3+}_{(aq)} + H_2, \quad (1)$$

where $h\nu$ represents ultraviolet radiation.

However, experiments focused on determining the specific rates of Fe(II) photochemical oxidation did not simulate the complex, disequilibrium water chemistry characteristic of an ocean where Fe(II)- and Si-rich hydrothermal waters mixed with ambient Si-saturated seawater that also contained high concentrations of HCO_3^{-}. Indeed, in fluids having high dissolved Fe(II), $Si(OH)_4$, and HCO_3^{-}, the oxidation effects of either UV-C (200–280 nm wavelength) or UV-A (320–400 nm wavelength) were found to be negligible compared to the precipitation of ferrous silicates and ferrous carbonates (e.g., Konhauser et al., 2007b). The point here is that although UV photo-oxidation does occur, in an ocean approaching saturation or supersaturation with respect to ferrous carbonate and silicate phases, UV photo-oxidation may have been relatively insignificant, particularly at anything but the shallowest water depths. Importantly, iron-rich waters, near saturation with ferrous iron phases, are likely essential for driving IF deposition, instead of simply background marine sedimentation.

Renewed interest in UV photo-oxidation of Fe(II) has focused on the possibility of UV-derived oxidants, such as hydrogen peroxide (H_2O_2), causing Fe(III) precipitation (Pecoits et al., 2015). Based on mass-balance calculations and consideration of the amount of hydrogen peroxide potentially generated by UV photo-oxidation of water, it was determined that the amount of hydrogen peroxide derived from atmospheric reactions is orders of magnitude too small to account for the Fe(III) sedimentation required to form IF (Pecoits et al., 2015). Studies of Fe and O isotopes have attempted to constrain the potential contribution of UV photo-oxidation of Fe(II) for IF deposition; but, results proved to be non-unique isotope signatures associated with UV photo-oxidation, thus hindering such an approach (Nie et al., 2017). Moreover, the recent UV photo-oxidation experiments of Nie et al. (2017) utilised a relatively simple, borate-buffered solution without silica that does not correspond to Archaean and Palaeoproterozoic seawater compositions. Accordingly, although it remains possible that UV photo-oxidation contributed to IF precipitation, this mechanism seems unlikely to have provided the major source of Fe(III) for the deposition of large IFs.

As an alternative to the abiological model, the presence of ferric iron minerals in IFs has also been ascribed to the metabolic activity of planktonic bacteria in oceanic photic zones (Fig. 9). Although a biological role in Fe(III)-oxyhydroxide precipitation was suggested around a century ago (e.g., Leith, 1903; Gruner, 1922), the importance of bacteria in this process began to receive greater acceptance with the discovery of microfossils in the ca. 1.88 Ga IFs in the Animikie Basin of the Lake Superior region (e.g., Tyler and Barghoorn, 1954; Barghoorn and

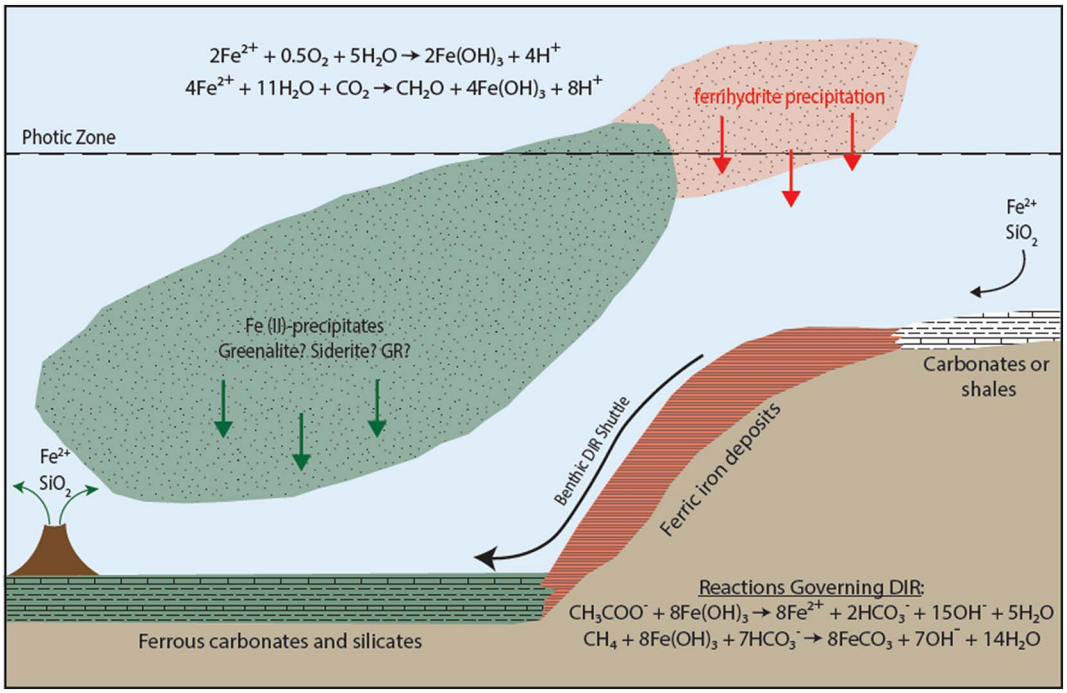

Fig. 9. Mechanisms of Fe(II) oxidation in Precambrian oceans. Two biologically controlled mechanisms are envisioned: (1) reaction of cyanobacterially-generated O_2 with dissolved Fe (II), and/or (2) direct oxidation via Fe(II)-based anoxygenic photosynthesis (photoferrotrophy). The Fe(II) was sourced from both deep-sea hydrothermal systems and continental weathering, whereas the Fe(III) formed in the photic zone was precipitated as ferrihydrite, $Fe(OH)_3$, and deposited onto the seafloor as a precursor sediment for IF. Some ferrihydrite was later reduced either through direct bacterial Fe(III) reduction (DIR) utilizing organic carbon or through a potential metabolic coupling of Fe(III) reduction and methane oxidation (e.g., Konhauser et al., 2005).

Tyler, 1965; Cloud, 1965). Based on the assumption that the microfossils were cyanobacteria, or their predecessors, Cloud (1973) proposed that these primitive O_2-producing photosynthetic bacteria lacked suitably advanced oxygen-mediating enzymes, and, consequently, required Fe(II) as an oxygen acceptor. Therefore, these microorganisms would have flourished when Fe(II) (and other nutrients) were made episodically available, allowing for the indirect oxidation and precipitation of Fe(III)-oxyhydroxides. By contrast, the photosynthetic population would have declined in number when Fe(II) availability was limited. Recent analyses of the microfossils within the 1.88 Ga Gunflint Iron Formation appear to confirm that cyanobacteria were a significant component of shallow-marine communities at that time (Lepot et al., 2017). What makes this model particularly intriguing, however, is experimental work demonstrating that Fe(II) concentrations in the range of 10s to 100 s of μM would lead to oxidative stress in cyanobacteria, resulting from reactions between Fe(II) and oxygen that produce reactive oxygen species (Swanner et al., 2015). These contradictory findings may suggest that primitive cyanobacteria had, at least by 1.9 Ga, some form of protection mechanism against Fe(II) concentrations becoming too high in proximal environments. In this regard, the study of Lepot et al. (2017) proposes that intracellular ferric iron biomineralisation might have offered protection against Fe(II) toxicity by reducing proximal iron concentrations.

Other bacteria may have directly utilised low O_2 concentrations available in surface waters of the Archaean oceans for Fe(II) oxidation. For example, Holm (1989) speculated that oxidation of Fe(II) by chemolithoautotrophic species, such as *Gallionella ferruginea*, would have been kinetically favoured in an ocean having limited free oxygen because abiological rates of Fe(II) oxidation at circumneutral pH are slow under microaerobic conditions (e.g., Søgaard et al., 2000). Interestingly, some of the ca. 1.88 Ga Gunflint-type microfossils from the Animikie Basin have been reinterpreted as chemolithoautotrophic Fe(II)-oxidisers (Golubic and Lee, 1999; Planavsky et al., 2009). It is important to note that some Gunflint fossil groupings (e.g., *Gunflintia*) may encompass multiple types of bacteria, including those with different metabolisms (Shapiro and Konhauser, 2015). The prospect of an early community of Fe(II)-oxidisers has been bolstered by the recognition of the importance of these bacteria in modern Fe-cycling in Chesapeake Bay (Field et al., 2016). These authors demonstrated that the Fe(II)-oxidisers were associated with low oxygen concentrations and active Fe redox cycling in the oxic–anoxic transition zone (< 3 μM O_2, < 0.2 μM H_2S). Although cyanobacteria were also detected in this transition zone, oxygen concentrations were too low to support significant rates of abiotic Fe(II) oxidation. Therefore, Field et al. (2016) speculated that cyanobacteria may be providing oxygen for microaerophilic Fe(II) oxidation through a symbiotic relationship; at high Fe(II) levels, cyanobacteria would gain protection against Fe(II) toxicity. The implication of recognising microaerophilic Fe(II)-oxidisers in modern ferruginous environments for IF deposition has also been discussed in recent reviews by Chan et al. (2016) and Koeksoy et al. (2016).

A different biological model was proposed by Garrels et al. (1973) and Hartman (1984), who both suggested photoferrotrophy as a metabolism supporting Fe(III) production. During this form of anoxygenic photosynthesis, light, not O_2, may have coupled the carbon and iron cycles, with the bacteria using Fe(II) rather than H_2O as an electron donor, and producing Fe(III) instead of O_2 as the metabolic waste [reaction 2].

$$4Fe^{2+} + HCO_3^- + 10H_2O \rightarrow 4Fe(OH)_3 + CH_2O + 7H^+ \quad (2)$$

Since then, several experimental studies have confirmed that various purple and green bacteria can use Fe(II) as a reductant for CO_2 fixation (e.g., Widdel et al., 1993; Heising et al., 1999; Straub et al., 1999). The ferric iron minerals these strains produce are also consistent with the most likely precursor IF minerals, Fe(III)-oxyhydroxides (Kappler and Newman, 2004). Photoferrotrophs have also been identified in Kabuno Bay, Democratic Republic of Congo, a basin characterised by ferruginous conditions and by observed rates of Fe(II) oxidation that appear to exceed those required for IF deposition (Llirós et al., 2015). In particular, photoferrotrophs produce amorphous to poorly crystalline Fe(III)-oxyhydroxide minerals, which carry a net

positive charge. Such biogenic minerals are expected to bind to organic carbon (cells) and silica, with the net effect being the deposition of Fe-Si-C aggregates onto the sea floor (Posth et al., 2008, 2010). One potential issue with the suggestion of photoferrotrophy in the Archaean is that a lack of an early ozone layer would have allowed high incoming UV radiation in the photic zone where photoferrotrophs are presumed to have resided. A solution to this issue lies in the work of Gauger et al. (2015, 2016), who provided evidence that minerals produced by photoferrotrophs, as well as other Fe(II)-oxidising bacteria, can protect the cells from UV radiation. These Fe(III) "shields" consist of nanometer-sized grains of ferrihydrite loosely attached to the cell surfaces.

2.5. The geobiology of iron formations

2.5.1. Evidence in the rock record for the evolution of oxygenic photosynthesis

To determine the significance of different biological oxidative mechanisms that may have driven IF deposition it is essential to constrain when oxygenic photosynthesis and anoxygenic photosynthesis evolved. Although the timing of cyanobacterial and photoferrotroph evolution is still debated, with some molecular clock and phylogenomic analyses suggesting that the crown group of oxygenic cyanobacteria post-dates the Proterozoic rise in oxygen (Shih et al., 2016), many indicators exist in the rock record pointing to an earlier appearance in the Archaean for both. In the case of cyanobacteria, these indicators include:

(1) Stromatolitic assemblages in the 2.72 Ga Tumbiana Formation, Western Australia, are presumed to have been constructed by photoautotrophs that utilised oxygenic photosynthesis (Buick, 1992). This view is supported by the earliest recognised fossil assemblage of filamentous and coccoidal cell colonies from the ca. 2.6 Ga Campbellrand Group, South Africa, possibly including oscillatoriacean cyanobacterial genera such as *Phormidium* and *Lyngbya* (Altermann and Schopf, 1995). Dodd et al. (2017) have recently identified microscale hematite-encrusted filaments within the ca. 3.8 Ga Nuvvuagittuq Supracrustal Belt in northern Québec, which they suggest may be ancient microaerophilic Fe(II)-oxidisers. If true, this implies a metabolism that relied on the presence of oxygen, and, by extension, cyanobacteria. Putative stromatolites have also been identified in the ca. 3.7 Ga Isua Greenstone Belt, southwest Greenland (Nutman et al., 2016), which the authors ascribed to an autotrophic carbon-fixing metabolism. However, the construction of stromatolite-like structures by the anoxygenic phototroph *Rhodopseudomonas palustris* (Bosak et al., 2007) challenges the notion that stromatolites uniquely mark cyanobacterial presence in the geologic record and that microfossil metabolism can be inferred from morphology alone.

(2) When microbial mats grow on siliciclastic sediment (e.g., in tidal flats, lagoons, sabkhas) they locally leave distinctive wrinkle and roll-up structures, laminated textures, and micro-impressions collectively referred to as mat-related structures (MRS). The filamentous bacteria, typically cyanobacteria or chemotrophic sulfide-oxidising bacteria, such as *Beggiatoa*, that comprise the mats, trap and bind sediments with their exopolysaccharide (EPS) secretions as they grow upward; this biostabilisation method allows them to withstand erosion by waves and currents. MRS are one of the oldest forms of fossil evidence, having been found in rocks as old as the 3.2 Ga Moodies Group, South Africa (Noffke et al., 2006; Heubeck, 2009) and the 2.9 Ga Pongola Supergroup, South Africa (Noffke et al., 2003). In the case of the Moodies Group, recent stratigraphic and depositional facies analysis have documented the association of three principal mat morphotypes representing different environmental settings: (1) planar-type in coastal floodplains, (2) wavy-type in intertidal zones, and (3) tufted-type in upper inter- to supratidal zones. All mat types suggest formation by phototrophic biota, but the tufted morphology implies an intricate level of coordinated growth commonly known from cyanobacterial mats in modern environments (Homann et al., 2015).

(3) Oxygenic photosynthesis at 2.72 to 2.59 Ga has been inferred from the presence of extremely isotopically depleted kerogen within carbonates and shales in the Hamersley Province of Western Australia, the Kaapvaal Craton in South Africa, and the Superior Craton in Canada. Organic carbon $\delta^{13}C$ values in these metasediments are as low as $-60‰$ (Hayes, 1983; Eigenbrode and Freeman, 2006). The most ^{13}C-depleted values have been ascribed to the assimilation of methane by chemolithoautotrophic, methanotrophic bacteria that in the modern world utilise electron acceptors such as O_2, SO_4^{2-}, or NO_3^-. However, sulfate can also form via photolysis of SO_2 of volcanic origin, and it might be possible to have methane oxidation via Fe^{3+} (e.g., Konhauser et al., 2005; Beal et al., 2009; Crowe et al., 2011). As outlined above, Fe(II) oxidation does not require oxygenic photosynthesis.

(4) Nitrogen isotope compositions of kerogens in minimally altered shales from the Campbellrand-Malmani carbonate platform in South Africa and broadly correlative sedimentary succession in Western Australia (Hamersley Group) show a significant rise in $\delta^{15}N$ values between 2.67 and 2.50 Ga (Godfrey and Falkowski, 2009; Garvin et al., 2009). Exceptionally high $\delta^{15}N$ values are also reported for the 2.72 Ga Tumbiana Formation (Thomazo et al., 2011). This positive shift has been interpreted as evidence for the onset of nitrification-denitrification reactions in the surface oceans (e.g., Beaumont and Robert, 1999); importantly, nitrification is typically thought to require oxygen. However, the emerging view is that it is possible to have anaerobic nitrification via Fe^{3+} (e.g., Yang et al., 2012; Busigny et al., 2013), thus making implications of the N isotope record more ambiguous than considered previously. Stüeken et al. (2015a) identified $\delta^{15}N$ values from a series of 3.2 to 2.75 Ga fluvial and marine successions that are centred on 0‰, which in their opinion is indicative of biological nitrogen fixation by the Mo-based nitrogenase. This may be difficult to reconcile owing to the low levels of Mo in the ancient ocean as a function of limited oxidative weathering (e.g., Scott et al., 2008); however, Stüeken et al. (2015a) suggested this constraint may have been overcome by either small contributions from oxidative weathering in localised areas or with hydrothermally-sourced Mo. If we assume that the Mo necessary to allow for Mo nitrogenase to be the predominant pathway for biological nitrogen fixation was sourced by weak oxidative weathering, then the implicit implication is that cyanobacteria would have been active since ~3.2 Ga.

(5) Over the past decade, redox-sensitive trace element data generated from paleosols, shales, carbonates, and IFs suggests an early Archaean rise of oxygenic photosynthesisers (see Robbins et al., 2016 for review). Among these data, the most widely cited are from shales in the Campbellrand-Malmani and Hamersley groups that contain high concentrations of Re and Mo. Strong Re and Mo enrichments and coupled Mo-Fe isotope data were interpreted as evidence for oxidative weathering of sulfide-bearing minerals on the continents, and thus the evolution of oxygenic photosynthesis as early as ca. 2.6 Ga (Anbar et al., 2007; Kendall et al., 2010; Czaja et al., 2012; Stüeken et al., 2015b). Re-Os isotopes from the same succession investigated by Anbar et al. (2007) further indicate that the observed Re enrichment is a primary, terrestrial signal, and not the result of post-depositional alteration (Kendall et al., 2015). Additional support for the appearance of oxygenic photosynthesis by 2.7 Ga comes from sulfide concentrations in marginal marine sediments (Stüeken et al., 2012). Also, continuously increasing $\delta^{98}Mo$ values in the black shales, carbonates, and oxide-facies IFs of the Marra Mamba and Wittenoom formations (2.6–2.5 Ga) in the

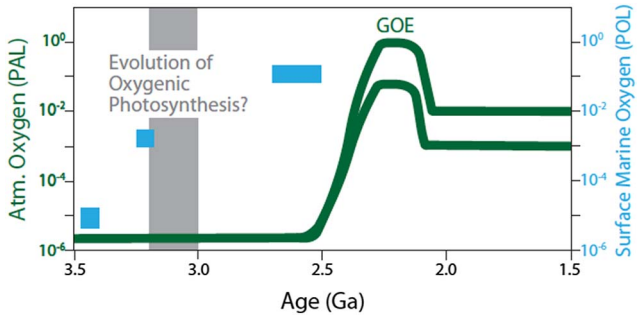

Fig. 10. Secular variations in atmospheric O_2 (green curve) and shallow ocean O_2 (blue boxes). Atmospheric O_2 curve is relative to present atmosphere levels (PAL), adapted from Lyons et al. (2014). GOE marks the "Great Oxidation Event" that may record an "over-shoot" (Bekker and Holland, 2012) in the first major rise in atmospheric O_2, followed by low periods in most of the Proterozoic. The green curves represent the range of commonly proposed pO_2 estimates for early Paleoproterozoic. There may also have been transient increases in atmospheric O_2 before the GOE (so-called whiffs), although such increases could also represent oxidative weathering associated with benthic mats (Lalonde and Konhauser, 2015). Estimates for maximum O_2 contents in shallow oceans (photic zones) in blue boxes relative to Present Ocean Level (POL) are based on modelling of stable Fe isotopes (Czaja et al., 2012; Li et al., 2013b; Satkoski et al., 2015), and potentially provide evidence that the shallow oceans had significant free O_2 levels by 3.2 Ga, hundreds of millions of years prior to the rise in atmospheric O_2. (For interpretation of the references to colour in this figure legend, the reader is referred to the web version of this article.)

Hamersley Basin have been tied to the sorption of light Mo isotopes onto Mn-oxides (Kurzweil et al., 2016). This pattern is also observed in the IF of the 2.95 Ga Sinqeni Formation, Pongola Supergroup, where the Mo isotope signature is consistent with the interaction with Mn(IV) oxides (Planavsky et al., 2014a). These Mo isotope signatures likely required an oxygenated water column and delivery of Mn(IV) oxides to the sediment pile, given rapid Mn(IV) oxide reduction via Fe^{2+} (e.g., Busigny et al., 2014). This implies that these signatures cannot be easily linked to anoxygenic photosynthetic Mn(II) oxidation more than a half of billion years before the GOE. Similarly, Cr isotopes from the 2.98 Ga Nsuze paleosol, also in the Pongola Supergroup, have been used as evidence for significant oxidative weathering on land, and thus appreciable levels of atmospheric oxygen, even at that time (Crowe et al., 2013). Frei et al. (2016) combined U/Th ratios and Cr isotopes to argue for oxidative weathering as far back in time as the 3.8–3.7 Ga Isua Supracrustal Belt, but at very low atmosphere oxygen contents (i.e., $\ll 10^{-5}$ present atmospheric levels, PAL; Fig. 10).

In terms of seawater, Satkoski et al. (2015) used a combination of stable Fe and radiogenic U–Th–Pb isotope data from the 3.2 Ga Manzimnyama IF of the Fig Tree Group, South Africa to demonstrate that proximal, shallow-water samples record precipitation under more oxic conditions compared to the distal, deeper-water facies, and that the presence of U enrichment in the shallow-water samples indicates the presence of free oxygen in the photic zone (Fig. 10). Results of the same approach applied to the 3.4 Ga Marble Bar Chert led Li et al. (2013b) to conclude that Fe(II) oxidation occurred under anoxic marine conditions by photoferrotrophy. Czaja et al. (2013), modelling Fe isotope fractionations, estimated free oxygen contents of < 0.001% that of modern seawater during deposition of the Isua IF. Although this approach clearly delineates a shift in the oxidative capacity of surface seawater, the limited extent of predicted Fe(II) oxidation could have been linked to oxidation pathways independent of O_2. Indeed, as explored below, photoferrotrophs can drive a wide range of extent of water column Fe (II) oxidation—including quantitative oxidation.

It is also important to note that oxygen evolution in the photic zone may have been decoupled from atmospheric evolution. Olson et al. (2013) estimated that photic zone O_2 contents could be as high as ~10 μM under an essentially anoxic atmosphere. Based on modelling of Fe isotopes in the Manzimnyama jasper, Satkoski et al. (2015) calculated shallow photic zone O_2 contents at ~10 μM (between 10^{-3} and 10^{-2} POL, or Present Ocean Level; Fig. 10), and deep-water O_2 contents at ~0.4 μM. The calculations of Czaja et al. (2012), based on covariation in Mo and Fe isotope compositions in carbonates of the 2.65–2.5 Ga Campbellrand-Malmami carbonate platform, estimated 35 μM O_2 content in the photic zone during this time period, being ~12% of modern level. The potential decoupling of photic zone and atmospheric O_2 content prior to the GOE is important in our understanding of the roles of O_2 sources and sinks, and of atmospheric evolution prior to the GOE.

(6) Several weight percent concentrations of organic carbon in sedimentary rocks provide one of the most straightforward and compelling arguments for the Archaean evolution of oxygenic photosynthesis, although this record becomes sparse for strata older than ~2.8 Ga. A wide range of microbial metabolisms can, of course, generate organic carbon, but only a handful of these metabolisms can realistically produce organic carbon-rich sedimentary rocks (Buick, 2008; Scott et al., 2011; Lyons et al., 2014; Krissansen-Totton et al., 2015). Since photoferrotrophy produces a particulate Fe(III)-oxyhydroxide as well as organic carbon, this process is more likely, as outlined below, to produce organic carbon-poor, iron-rich rocks like IF, because much of the organic matter would be oxidised via DIR, which, if this process was widespread, would limit the use of organic carbon content in IFs as a direct indicator of organic carbon deposition. Photosynthetic sulfide and H_2 oxidisers can be important primary producers and could in theory produce organic matter-rich rocks like black shales. However, the reductant for these microbial metabolisms, unlike for oxygenic photosynthesis, must be sourced from a hydrothermal system or produced via microbial degradation of organic matter. Sulfide and H_2, unlike Fe(II), are not thought to have been present at significant levels in the Archaean water column (Lyons et al., 2014).

2.5.2. Evidence in the rock record for the evolution of photoferrotrophy

Compared to oxygenic photosynthesis, there is less actual physical and chemical evidence for the existence of Fe(II)-oxidising phototrophs in the Archaean. An argument in favour of photoferrotrophy having played a prominent role in IF deposition is that much of the evidence for pre-GOE surface-ocean oxygenation remains contested and proxies that specifically focus on shallow-ocean redox conditions, such as carbonate iodine (Hardisty et al., 2014) and REEs (Planavsky et al., 2010a), point to the dominance of IF and carbonate deposition under broadly anoxic conditions in the oceans until the GOE. Supporting this, molecular phylogenetic analysis of many enzymes involved in (bacterio)-chlorophyll biosynthesis suggests that anoxygenic photosynthetic lineages are likely more deeply rooted than oxygenic cyanobacterial lineages (Xiong, 2006).

Numerical models have been used to suggest that anoxygenic photosynthesisers would control Fe(II) oxidation even if the surface layer was weakly oxygenated (Kappler et al., 2005). This model is based on the simple idea that a layer of photoferrotrophs could thrive beneath an oxygenated surface layer even at low levels of photosynthetically active light. The model employs Fe(II) oxidation rates from modern photoferrotrophs under a range of reasonable mixing rates in the ocean. It is also likely that photoferrotrophs flourishing at depth could have exhausted dissolved phosphorous in upwelling waters, thus outcompeting cyanobacteria for a key nutrient, and by extension limiting their activity in overlying waters (Jones et al., 2015).

Kappler et al. (2005) presented a model for determining the thickness of a marine layer with photoferrotrophic bacteria required to fully oxidise a hydrothermal source of Fe(II) at a variety of Fe(II)-oxidation rates in which eddy-diffusion was the predominant mode of Fe(II) transport. This essentially assumes that diapycnal diffusivity was the main transport term. At a conservative, experiment-based, depth-

integrated, phototrophic Fe(II)-oxidation rate of 1.4×10^{-5} M/day (corresponding to a depth of 100 m), an estimated Fe(II) concentration of 0.5 mM, and the modern global mean eddy-diffusion rate of 0.1 cm^2/s, it was estimated that a photoferrotrophic bacterial layer 17.6 m thick was required to completely oxidise the Fe(II) input. This result suggests that such bacteria could potentially have oxidised all of the upwelling Fe(II) in Precambrian oceans.

A potential limitation with the approach of Kappler et al. (2005) is that in many settings advection can be the dominant transport process (e.g., upwelling zones). As a simple test to assess the required thickness of a photoferrotrophic bacterial layer to oxidise both upwelling and diffusive Fe(II) inputs, we add upwelling as a mode of Fe(II) transport to the Kappler et al. (2005) model. The thickness required to quantitatively oxidise upwelling iron is calculated similarly to Kappler et al. (2005) using the expression: $z = \omega \times \Delta C / (d\mathrm{Fe(II)} / dt)$, where ω represents advection or upwelling rate, ΔC is the iron concentration gradient from the bottom to the top of the Fe(II)-oxidising bacterial community, and $d\mathrm{Fe(II)} / dt$ is the rate of photoferrotrophic Fe(II) oxidation. The calculated thickness is then added to that for eddy-diffusion, using the modern global mean eddy diffusivity of 0.1 cm^2/s. Results with ΔC values of 0.5 mM and 0.1 mM and upwelling rates of 0.5 m/day and 5 m/day are shown in Fig. 11. Modelled advection rates (0.5 and 5 m/day) fall within the average and high ranges of annual averages observed in modern continental upwelling zones (e.g., Canfield, 2006).

Not surprisingly, the thickness of the photosynthetic Fe(II)-oxidising bacterial layer increases when advection is considered as opposed to solely eddy-diffusion transport. The thickness of the photoferrotrophic bacterial layer is quite sensitive to upwelling rates, especially at low rates of Fe(II) oxidation. At the conservatively estimated Fe(II)-oxidation rate of 1.4×10^{-5} M/day and an Fe(II) concentration of 0.1 mM, a 34 m- or > 100 m-thick layer of Fe(II)-oxidising bacteria is required to fully oxidise the Fe(II) input at upwelling rates of 0.5 and 5 m/day, respectively (Fig. 11). These estimates are significantly larger than the 17.6 m thickness calculated with eddy-diffusion alone by Kappler et al. (2005). Furthermore, when considering the expected range of upwelling conditions and reasonable rates of photoferrotrophic Fe(II) oxidation, this result indicates a wide scope in the extent of Fe(II) oxidation in Archaean water masses. In fact, given that upwelling is highly variable on a seasonal time scale (with shifts over an order of magnitude in some settings), a variable extent of oxidation is likely to characterise any Archaean setting where upwelling was an important transport mechanism.

2.6. Available reductants and diagenesis of iron formations

Oxidation of Fe(II), either indirectly via oxygenic photosynthesis, or directly via anoxygenic photoferrotrophy, would produce biomass that settled to the seafloor together with the Fe(III) minerals (e.g., Konhauser et al., 2005; Li et al., 2011; Posth et al., 2013a, 2013b). If, as today, the organic carbon was oxidised during burial by either diagenesis or metamorphism, the relevant question is which terminal

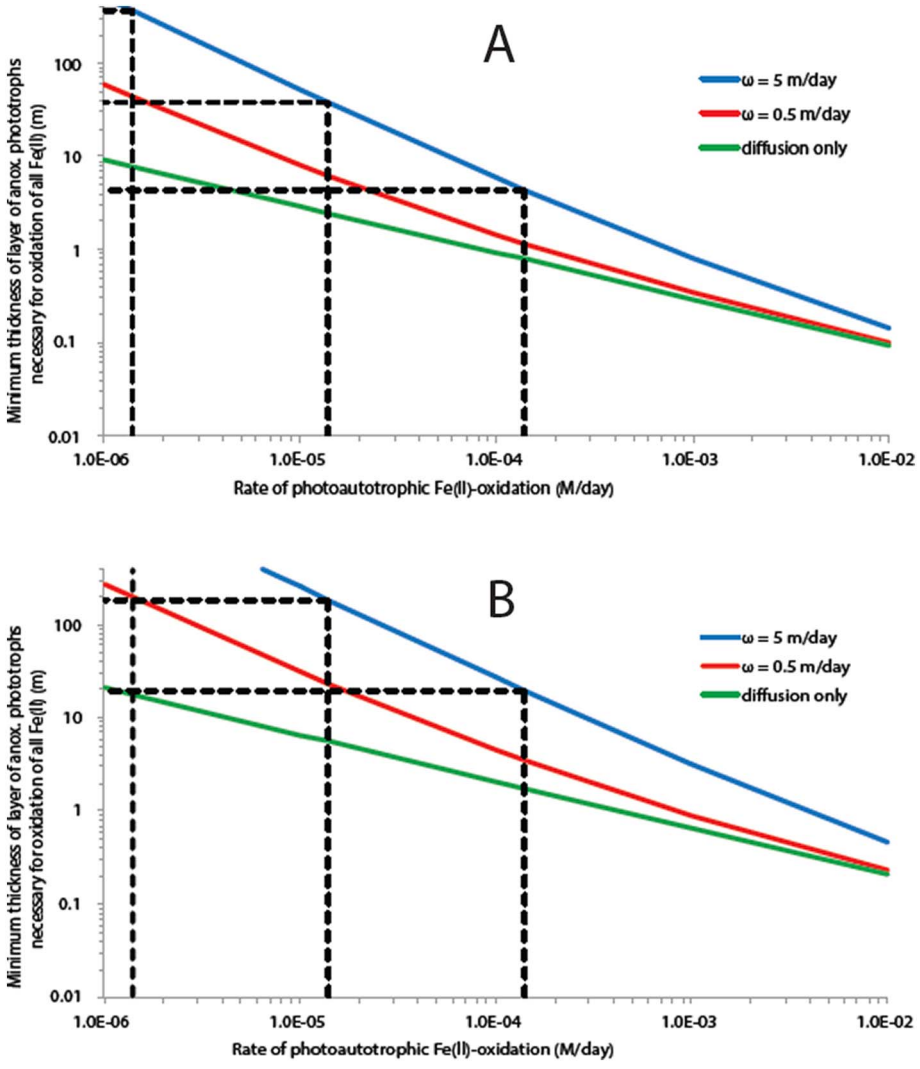

Fig. 11. Calculated thickness of a community of photoferrotrophs required to completely oxidise upwelling, Fe(II)-rich, hydrothermal waters with Fe(II) concentrations of (A) 100 uM and (B) 500 uM, at different rates of Fe(II) oxidation. Unless noted, advection and eddy-diffusion Fe supply rates are summed, with eddy-diffusion held constant at 0.1 $cm^2\,s^{-1}$ in all cases (cf., Kappler et al., 2005). Modelled advection rates are consistent with low and high annual averages for upwelling regimes on continental margins. Eddy-diffusivity value of 0.1 $cm^2\,s^{-1}$ is also shown on each plot. Dashed lines indicate the photoferrotrophic layer thickness required for Fe(II) oxidation at rates of 1.4×10^{-4}, 1.4×10^{-5}, and 1.4×10^{-6} M day^{-1}, with 1.4×10^{-5} M day^{-1} representing a conservative estimate as determined experimentally by Kappler et al. (2005). Thickness of photoferrotrophic layer increases dramatically with low Fe(II) oxidation rates when both advection and eddy-diffusional Fe transport are considered, as opposed to solely eddy-diffusional transport. At conservatively estimated Fe(II) oxidation rate for upwelling waters with Fe(II) concentration of 500 μM, photoferrotrophic layer thicknesses of 17.6 and 5.6 m are required when solely considering diffusion at rates of 1 $cm^2\,s^{-1}$ (not shown) and 0.1 $cm^2\,s^{-1}$, respectively. These thicknesses are distinctly different than > 100 m required when both advection at 5 m day^{-1} and diffusion at 0.1 $cm^2\,s^{-1}$ are considered for the same Fe concentrations in upwelling waters. More realistic layer thickness of ~35 m is required for Fe(II) oxidation rate of 1.4×10^{-5} M day^{-1} and advection rate and eddy-diffusivity of 5 m day^{-1} and 0.1 $cm^2\,s^{-1}$, respectively, at 100 μM Fe in upwelling waters.

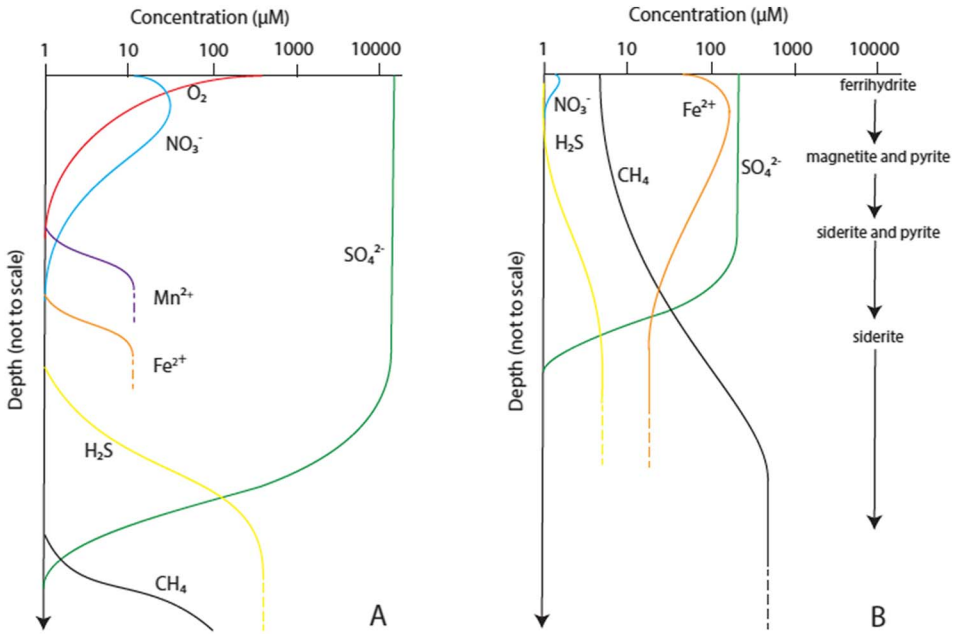

Fig. 12. Comparison of (A) typical sediment pore-water profile during early diagenesis in a modern continental marine setting (e.g., Froelich et al., 1979; modified from Konhauser, 2007), and (B) plausible Archaean pore-water profile during early diagenesis wherein minerals on right-hand side are dominant controls on pore-water Fe speciation. As shown in Fig. 9, delivery of $Fe(OH)_3$ to sediment is controlled by O_2 concentrations and/or metabolism of photoferrotrophic bacteria.

electron acceptor was present at the seafloor during times of IF deposition, and at what concentrations? Despite the possibility of some oxic surface waters being generated by cyanobacterial activity as early as 3.8 Ga (see discussion above), deep waters, and by extension the seafloor, remained anoxic, unlike today where sediment pore-waters can have dissolved oxygen at depths of several millimeters, and locally even greater depths (Fig. 12A). In the absence of O_2, the fermentation products in the bottom waters and/or shallow sediments would have been oxidised via some other form of anaerobic respiratory process. In terms of such pathways, the paucity of O_2 would also have meant minimal nitrate and sulfate availability, the former being evident from the lack of positive $\delta^{15}N$ values before ca. 2.7 Ga (Godfrey and Falkowski, 2009; Thomazo et al., 2011), and the latter being evident from negligible sulfur isotopic fractionations in the Archaean sedimentary sulfide record (e.g., Strauss, 2003). The supply of MnO_2 was likely also not significant until after the GOE, due to the oxidation of dissolved Mn(II) requiring the presence of free dissolved oxygen and an aerobic microbial catalyst (e.g., Tebo et al., 2005), although the plausibility of a Mn(II)-based photosynthesis pre-dating the rise of oxygen has been hypothesised (Johnson et al., 2016), but not confirmed in modern cultures.

By contrast, the ferric minerals in IF would have represented a favourable electron acceptor for the oxidation of organic matter (Walker, 1984; Nealson and Myers, 1990) through DIR by various bacteria and archaea (Fig. 12B). Significantly, coupling the reduction of some Fe(III) minerals to the oxidation of organic matter not only explains the low content of organic carbon in IFs (< 0.5 wt%; Gole and Klein, 1981), but it also explains highly negative $\delta^{13}C$ values of the early diagenetic Fe (II)–rich carbonates (Perry et al., 1973; Walker, 1984; Baur et al., 1985; Heimann et al., 2010; Craddock and Dauphas, 2011), the small-scale heterogeneity in $\delta^{56}Fe$ values (e.g., Steinhofel et al., 2010; Li et al., 2013a), the presence of Fe(II)-bearing minerals in IF (e.g., magnetite, siderite, greenalite – recall Section 2.3), and the general lack of microfossils preserved in the Fe-rich layers lacking silicification. Moreover, the reduction of ferric iron may also have been coupled to the anaerobic oxidation of methane (Konhauser et al., 2005), an observation supported by the reaction's likely occurrence in modern marine sediments (Riedinger et al., 2014) and lakes (Crowe et al., 2011), as well as in culture experiments (Ettwig et al., 2016; Bray et al., 2017).

An estimate of the organic carbon content (C_{org}) that may have been initially deposited with Fe(III) precipitates in IFs may be made by calculating the electron equivalents of the organic C tied in Fe-carbonates, based on their $\delta^{13}C$ values, as well as Fe(II) quantities required to make magnetite (Li et al., 2013a). Although measured C_{org} contents of the large Transvaal BIFs, correlative with the Hamersley BIFs, are quite low (~0.01 wt%), estimated initial C_{org} contents are much higher, ~5 wt% (Fig. 13), based on the C isotope and magnetite mass balances. Using C isotope data, CO_2 content, and Fe(II) and Fe(III) data from Beukes et al. (1990), Beukes and Klein (1990), and Kaufman (1996), the average initial C_{org} based on C isotope composition is 1.28 wt% for oxide-facies IF and 3.24 wt% for siderite-facies IF. For oxide-facies IF, based on Fe(II) abundances in magnetite, and assuming an equivalent electron balance was contained in organic carbon, an additional 3.42 wt% C_{org} is calculated, for a total of 4.70 wt% initial C_{org} in oxide-facies IF. Although this calculation assumes that magnetite was produced solely by reduction of hematite, stable isotope results discussed below support that interpretation. Such quantities of C_{org} are similar to those in Neoarchaean black shales, and highlight the possibility that significant organic carbon was buried with Fe(III) precipitates during IF deposition.

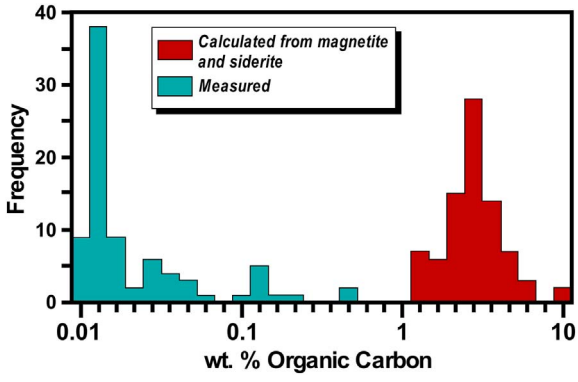

Fig. 13. Comparison of wt% organic carbon measured in ca. 2.5 Ga Transvaal IFs (Beukes et al., 1990; Beukes and Klein, 1990; Kaufman, 1996) with those estimated for the same samples based on organic carbon contents required to account for $\delta^{13}C$ values of siderite and Fe(II) concentrations in magnetite. Using this approach, average original organic carbon content was 4.70 wt% for oxide-facies IF, which is comparable to those measured in Neoarchaean black shales, indicating potentially large amounts of initial organic carbon deposition that was later respired to produce siderite and magnetite via DIR. See additional discussion in Li et al. (2013a).

The possibility of DIR producing the large Fe(II) inventory in IFs is supported by molecular phylogeny, specifically from the observation that many deeply-branching *Archaea* (i.e., some of the oldest purported species) can use H_2 to reduce Fe(III) to support chemolithoautotrophic growth (Vargas et al., 1998). Fe(III)-reducing bacteria can even use quinone moieties as electron shuttles between solid-phase iron minerals and H_2, thereby alleviating the need for direct contact between the cell and mineral surface (Lovley et al., 2000). Moreover, DIR has been shown to be broadly distributed among several known *Proteobacteria* genera, suggesting that this form of metabolism became widespread early in the course of evolution (Barns and Nierzwicki-Bauer, 1997).

Finding clear evidence of Fe(III) reduction in the mineralogical record of IFs, however, has been difficult, although a few possibilities exist. For instance, the spheroidal forms of siderite found in several IFs are similar to those of the siderite grains formed experimentally when ferrihydrite is reacted with organic carbon at pressure and temperature conditions commensurate with IF diagenesis (Köhler et al., 2013). Likewise, the large magnetite grains found in many IFs can be replicated experimentally through a three-stage sequence, beginning with DIR of an initial ferric iron-rich sediment coupled to the oxidation of dead phytoplankton biomass, followed by magnetite crystal aging, and ultimately by pressure- and temperature-induced abiotic alteration of the biogenic magnetite during metamorphism (Y.-L. Li et al., 2013). Such transformations, if they occurred at temperatures of > 100–150 °C, may explain magnetite that has positive $\delta^{18}O$ values (Fig. 8); inorganic reaction between Fe(III)-oxyhydroxides and organic matter is another possible explanation. However, as noted above, magnetite that has $\delta^{18}O$ values less than zero requires formation at lower temperature (Fig. 8), and, in such cases, direct, microbially-catalysed reduction seems the best explanation. The strongest proof of microbial Fe(III) reduction, therefore, lies in the isotopic compositions of IF minerals.

Although much of the discussion on microbial Fe(III) reduction in IFs has focused on processes within the sediment, it is possible that Fe(III) reduction occurred in the water column, or exported Fe(II) to the water column, which would have affected the efficiency of Fe and C recycling prior to final burial. In an attempt to test this possibility, Konhauser et al. (2005) modelled the ancient Fe cycle based simply on conservative experimental rates of photosynthetic Fe(II) oxidation in the photic zone. They showed that under ideal growth conditions, as much as 70% of the biologically produced Fe(III) could have been recycled back into the water column via fermentation and organic carbon oxidation coupled to DIR. By comparing the potential size of biomass generated phototrophically with the reducing equivalents required for Fe(III) reduction and magnetite formation, they also hypothesised that another anaerobic metabolic pathway might have been utilised in the surface sediment to oxidise organic carbon. Based on the premise that the deep ocean waters were anoxic, this role could have been fulfilled by a consortium of fermenters and methanogens (Konhauser et al., 2005).

Iron-rich carbonates (siderite and ankerite) in IFs have $\delta^{13}C$ values that are significantly lower than those expected for precipitation from seawater (as represented by limestone and dolostone) (Fig. 14). $\delta^{13}C$ values as low as −16‰ (Fischer et al., 2009) have been traditionally explained (e.g., Walker, 1984) as resulting from the mixing of dissolved inorganic carbon (DIC) from seawater and remineralised organic carbon via DIR [reaction 3], as opposed to further carbon inputs derived from Fe(III)-induced methane oxidation [reaction 4]. However, the latter possibility has yet to be tested with simple numerical models that account for the depositional setting of IFs and realistic Archaean seawater chemistry.

$$4Fe(OH)_3 + CH_2O + 3HCO_3^- \rightarrow 4FeCO_3 + 3OH^- + 7H_2O \quad (3)$$

$$4Fe(OH)_3 + 0.5CH_4 + 3.5HCO_3^- \rightarrow 4FeCO_3 + 3.5OH^- + 7H_2O \quad (4)$$

Using the equations in Konhauser et al. (2005), only 1 mol of carbonate is produced via organic carbon oxidation for 4 mol of Fe(III) reduced, requiring an additional 3 mol of carbonate, presumably from a seawater source; this is equivalent to a C_{org}:C_{sw} ratio of 1:3 (Fig. 14). In case of the Eq. (4), C_{meth}:C_{sw} ratio is 1:7. These ratios are consistent with the fact that IF carbonates are rarely pure siderite, but instead consist of magnesite-siderite and dolomite-ankerite solid solutions and hence require a seawater source of Ca and Mg. As discussed in Heimann et al. (2010), alternative proportions of external carbonate relative to organic carbon can also be envisioned [reactions 5 and 6]:

$$4Fe(OH)_3 + CH_2O + 2HCO_3^- \rightarrow 3FeCO_3 + Fe^{2+}{}_{aq} + 4OH^- + 6H_2O \quad (5)$$

$$4Fe(OH)_3 + CH_2O + HCO_3^- \rightarrow 2FeCO_3 + 2Fe^{2+}{}_{aq} + 5OH^- + 5H_2O \quad (6)$$

where reactions 5 and 6 have C_{org}:C_{sw} ratios of 1:2 and 1:1, respectively. As the C_{org}:C_{sw} ratio decreases, greater quantities of Fe^{2+}_{aq} are produced, which would be expected to produce increasing quantities of magnetite through the reaction of Fe^{2+}_{aq} and unreduced Fe(III)-oxyhydroxides.

Heimann et al. (2010) recognised that reactions 3, 5, and 6 predict changes in both the $\delta^{13}C$ and $\delta^{18}O$ values of IF carbonates, where a decreasing component of seawater carbonate (which has high $\delta^{13}C$ and $\delta^{18}O$ values) would produce decreases in both $\delta^{13}C$ and $\delta^{18}O$ values of carbonate that would also correlate with a shift from siderite-facies IF to oxide-facies IF, relations that are observed in the large ca. 2.5 Ga Transvaal IFs (Fig. 14). Such a model explains the long-standing puzzle of why IF carbonates have lower $\delta^{18}O$ values than coeval Ca-Mg carbonates, as well as the observation that the average $\delta^{13}C$ value of carbonates in oxide-facies IF are lower than those in siderite-facies IF (Fig. 14). This model also explains the observation that organic carbon contents are lowest in oxide-facies IF as compared to siderite-facies IF and the relation between $\delta^{13}C$ and wt% C_{org} (Fig. 14), where large proportions of electron equivalents from organic carbon lie in the magnetite inventory of oxide-facies IF. Finally, low $\delta^{18}O$ values of carbonates from oxide-facies IF likely reflect their formation at a later stage in diagenesis in deeply buried sediments that were disconnected from the water column.

To further explore the idea that the observed carbon isotope values result solely from the mixing of DIC from seawater and remineralised organic carbon, we use a basic mass-balance model to explore a range of environmental conditions. For simplicity, carbonate precipitation/dissolution, and accompanying buffering effects, linked with a dynamic DIC reservoir, are ignored. The $[DIC]_{total}$ was calculated using a modified version of the general diagenetic equation presented in Berner (1964) that was used in recent work to discuss the potential for sulfate reduction as a driver of the $\delta^{13}C$ values of authigenic carbonates from the Proterozoic Chuanlingguao Formation in North China (W. Li et al., 2015; C. Li et al., 2015); see equation below. The three terms of this equation describe the processes of ionic diffusion, deposition and compaction, and input of DIC into the pore-waters from organic matter remineralisation, respectively. In this equation, G_0 is the concentration of organic carbon at the sediment/water interface; D and ω are the diffusion coefficient in the whole sediment and the sum of deposition and compaction, respectively; k is the rate of organic carbon remineralisation (calculated from ω; Boudreau, 1997); z is depth in the sediment; C is [DIC]; t is time; and L is a stoichiometric coefficient that describes the ratio between the amount of Fe(III) moles reduced for every carbon mole oxidised. The model is tuned to have organic mineralisation generally describing conditions of anoxic remineralisation (Boudreau, 1997).

$$\frac{\partial C}{\partial t} = D\frac{\partial^2 C}{\partial z^2} - \omega\frac{\partial C}{\partial z} + kLG_0\exp\left[-\frac{k}{\omega}z\right] \quad (A)$$

The general solution for this expression was obtained assuming steady state, $\frac{\partial C}{\partial t} = 0$, and the boundary condition $C = C_\infty$, giving the

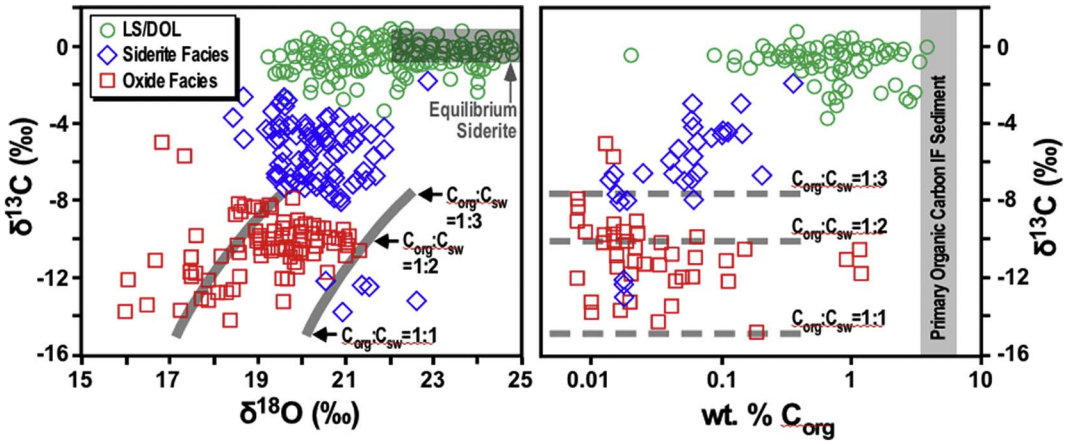

Fig. 14. Co-variation in C and O isotope compositions of carbonates from 2.6–2.5 Ga Kuruman IF and Campbellrand-Malmami carbonate platform in South Africa, and bulk-rock organic carbon contents. Ca-Mg carbonates (limestone and dolostone) shown by green circles, ankerite/siderite from siderite-facies IF by blue diamonds, and ankerite/siderite from oxide-facies IF by red squares. Data from Beukes et al. (1990), Beukes and Klein (1990), Kaufman (1996), and Heimann et al. (2010). Transparent grey box in left diagram shows C and O isotope compositions for siderite that would be in equilibrium with seawater, indicating that none of the siderite in either siderite-facies IF or oxide-facies IF is in C or O isotope equilibrium with seawater. Parallel grey curves in left diagram show mixing lines between seawater carbonate and carbonate produced by DIR at various ratios of organic C to seawater carbon (see reactions 3, 5, and 6 in main text). Estimate for primary organic carbon content of IF, prior to DIR, shown in right diagram from Fig. 13. See Heimann et al. (2010) for details. (For interpretation of the references to colour in this figure legend, the reader is referred to the web version of this article.)

following analytical solution (Eq. (B)):

$$C(z) = -\frac{\omega^2 L G_0}{Dk + \omega^2} exp\left[-\frac{k}{\omega}z\right] + C_\infty \quad (B)$$

A basic assumption of the model is that a constant DIC concentration, C_0, is contributed from seawater to the sediment profile and is equal to the DIC concentration of the overlying water column. Such an assumption allows for the use of the boundary condition, $C_0 = [DIC]_{SW}$, with Eq. (C) providing solution for C_∞. Substituting Eq. (C) into Eq. (B), the final solution for $[DIC]_{total}$ is obtained (Eq. (D)).

$$C_\infty = \frac{\omega^2 L G_0}{Dk + \omega^2} + C_0 \quad (C)$$

$$C(z) = -\frac{\omega^2 L G_0}{Dk + \omega^2} exp\left[-\frac{k}{\omega}z\right] + \frac{\omega^2 L G_0}{Dk + \omega^2} + C_0 \quad (D)$$

Simply taking the difference between $[DIC]_{total}$ and $[DIC]_{SW}$ to determine $[DIC]_{OM}$, the mass balance relationship can be implemented to determine the carbon isotope composition of the DIC pore-water reservoir (Eq. (E)). The model accounts for isotopic inputs of DIC from seawater ($\delta^{13}C_{sw}$ = 0‰) and the remineralisation of organic matter during DIR ($\delta^{13}C_{OM}$ = − 25‰), with the isotopic values held constant and only the fluxes of DIC from each source varied with depth. This basic approach is widely used to model modern marine carbon isotope profiles, despite the intrinsic simplifications of the model:

$$[DIC]_{Total}\,\delta^{13}C_{Total} = [DIC]_{OM}\,\delta^{13}C_{OM} + [DIC]_{SW}\,\delta^{13}C_{SW} \quad (E)$$

With this approach, it is straightforward to illustrate the main processes that will control pore-water DIC carbon isotope values. Importantly, decreasing the sedimentation rate and initial utilisable organic carbon concentrations, and increasing the size of the marine DIC reservoir will result in heavier $\delta^{13}C_{DIC}$ values. This result is relevant for Archaean IF because there is nearly unanimous agreement that (i) the size of the DIC reservoir was significantly larger in the Archaean than in the modern ocean, (ii) most IF precursor sediments were deposited in offshore environments with limited siliciclastic input and low sedimentation rates, and (iii) proportionally more Fe(III) existed than organic carbon buried with IF precursor sediments relative to typical modern continental margin sediments (Ridgwell and Zeebe, 2005; Bekker et al., 2010).

The effects of sedimentation rate, concentration of initial reactive organic carbon, and size of the marine DIC reservoir on pore-water profiles are illustrated here by comparing conditions likely to be characteristic of IF precursor sediments with those typical of modern continental-margin sediments. In this case, we use a site in the Santa Barbara Basin as representative of the continental margin sediment column. This site is noteworthy for its role in the development of early diagenetic modelling (Berner, 1964), but it is also a fair representation of modern marginal settings with high organic carbon loading and high rates of sulfate reduction. If we consider the modern DIC reservoir, as well as sedimentation rates and organic carbon loads characteristic of continental margin settings, $\delta^{13}C$ values of pore-water DIC quickly (within upper 20 cm) become highly depleted ($\delta^{13}C_{DIC} < -20$‰). However, with sedimentation rates and initial metabolisable organic carbon concentrations being an order of magnitude less than those typical of continental margin sediments, and a DIC reservoir an order of magnitude larger than the modern one, the pore-water DIC $\delta^{13}C$ values would stabilise at values heavier than − 6‰ (Fig. 15). This magnitude of offset, relative to modern marginal sediments, seems likely for IF precursor sediments. In addition, although IF sedimentation was likely highly pulsed and variable (Bekker et al., 2010; Haugaard et al., 2016a), slow net accumulation rates were probably linked to a low siliciclastic flux that allowed for accumulation of pure chemical sediments. Lastly, as mentioned above, it is generally accepted that the DIC reservoir was much larger in the Archaean relative to today; in this context, an estimated ten-fold greater size compared to that of the modern reservoir seems reasonable (Hotinski et al., 2004; Ridgwell and Zeebe, 2005; Higgins et al., 2009), although a commensurate reduction in organic carbon reservoir size is also required to explain the $\delta^{13}C$ values of Ca-Mg (non-IF) carbonates throughout the Archaean (e.g., Krissansen-Totton et al., 2015). Consequently, the carbonate carbon isotope record in IF is consistent with significant levels of methane cycling in the precursor sediments. In fact, the large spread in IF carbonate $\delta^{13}C$ values and markedly light values are exactly what would be expected in the presence of Fe(III)-mediated organic carbon and methane oxidation in the upper part of the sediment pile. The most distinct isotopic fingerprint of this process is the observation that neither the C or O isotope compositions of IF carbonates match those expected for equilibrium with seawater.

Detailed stable Fe isotope studies of hematite, magnetite, and siderite in IFs, including in situ or small-sample isotopic analysis, also demonstrate that these minerals did not form in Fe isotope equilibrium with each other or with seawater (Fig. 16). This result potentially provides further support for in situ reduction of Fe(III) oxyhydroxides

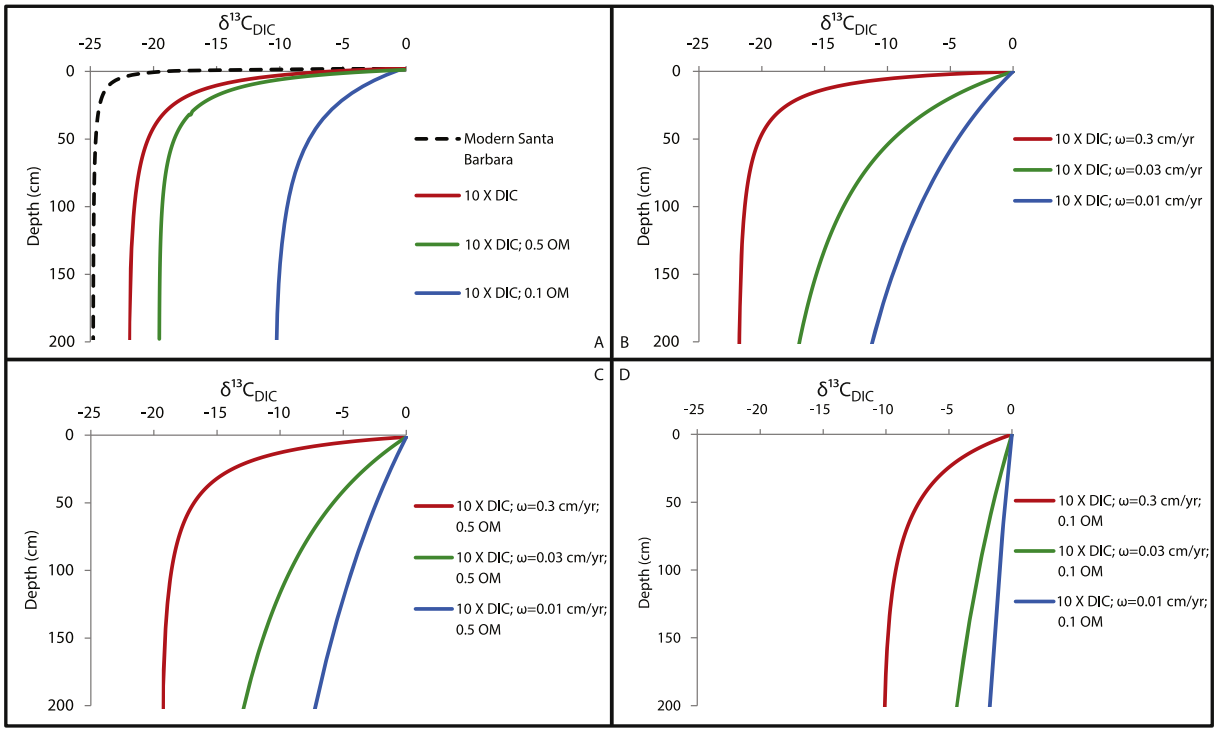

Fig. 15. Calculated $\delta^{13}C_{DIC}$ for sediments dominated by anaerobic organic matter remineralisation. Unless noted in legend, sediment and water column parameters are for Santa Barbara Basin (from Berner, 1964). Water column DIC concentration is taken from modern continental margin values; sedimentation rate and organic matter (OM) concentrations are varied at ranges typical of continental margin settings. A DIC concentration of 10 × modern one is used as estimate for Archaean oceans. (A) $\delta^{13}C_{DIC}$ vertical pore-water profiles for modern Santa Barbara Basin conditions compared with modelled Archaean settings with 10 × DIC and various organic matter fluxes. (B) $\delta^{13}C_{DIC}$ vertical pore-water profiles for modelled Archaean settings with DIC 10 × of modern seawater showing effect of variations in the sum of sedimentation and compaction (ω) from that in the modern Santa Barbara Basin. (C) Effect of variations in ω, at DIC 10 × that of modern seawater and OM loads at 0.5 × that of the modern Santa Barbara Basin, on $\delta^{13}C_{DIC}$ vertical pore-water profiles for modelled Archaean settings. (D) Effect of variations in ω, at DIC 10 × that of modern seawater and OM load at 0.1 × that of the modern Santa Barbara Basin, on $\delta^{13}C_{DIC}$ vertical pore-water profiles for modelled Archaean settings.

by DIR in the sediment prior to lithification, consistent with the C and O isotope data discussed above. The Fe isotope composition of Archaean seawater was likely temporally and spatially variable, reflecting, in part, variable extents of Fe(II) oxidation (e.g., Rouxel et al., 2005). IF minerals that formed in equilibrium with seawater should have $\delta^{56}Fe$ values offset from the seawater composition based on specific mineral-fluid Fe isotope fractionation factors. In contrast, the $\delta^{56}Fe$ values for coexisting oxides and carbonates, from the micron scale to bulk-sample analysis of gram-size quantities, show that Fe isotope compositions scatter closely about a 1:1 line, with some samples trending toward, but not reaching, Fe isotope equilibrium. The 1:1 line can be considered a common source of Fe for specific magnetite-hematite and magnetite-siderite pairs (e.g., Li et al., 2013a), taken to reflect authigenic formation of magnetite and siderite through reduction of Fe(III)-oxyhydroxide. Samples that display high $\delta^{56}Fe$ values for the initial Fe(III) precipitate are interpreted to reflect a hydrothermal source of Fe based

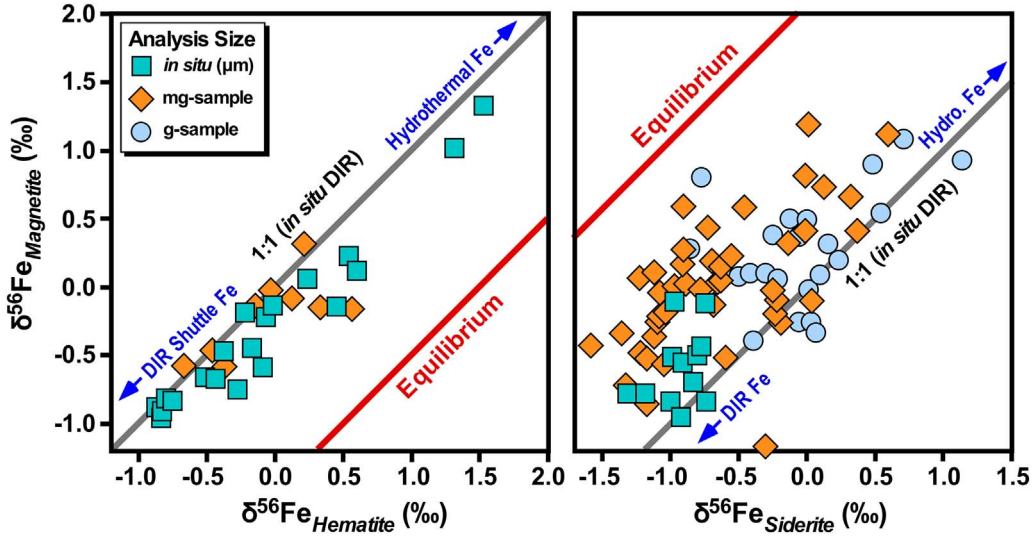

Fig. 16. Iron isotope variations among co-existing hematite, magnetite, and siderite (same sample) from the 2.48–2.47 Ga Dales Gorge Member and Kuruman Formation, respectively, as measured on various scales, from μm scale via in situ analysis by laser ablation, mg-size by bulk analysis, and g-size by bulk analysis. Equilibrium hematite-magnetite and siderite-magnetite Fe isotope fractionations at low temperature (~25 °C) are shown in red (Wiesli et al., 2004; Wu et al., 2010; Frierdich et al., 2014), indicating that none of the minerals are in Fe isotope equilibrium. Grey lines (marked "1:1") reflect origin through reduction of common precursor Fe(III) oxyhydroxide via "in situ" DIR in sediment prior to lithification. Broad variations in $\delta^{56}Fe$ values, from positive to negative values, is interpreted to reflect various Fe sources, ranging from hydrothermal (positive $\delta^{56}Fe$) to DIR shuttle from continental shelves (negative $\delta^{56}Fe$); see Fig. 6. (For interpretation of the references to colour in this figure legend, the reader is referred to the web version of this article.)

Sources: Johnson et al. (2003, 2008b); Steinhofel et al. (2010); Heimann et al. (2010); Craddock and Dauphas (2011).

on Fe-Nd isotope relations (Fig. 6), whereas samples that have low initial δ^{56}Fe values may reflect a microbial source of Fe(II) that was shuttled from a continental shelf environment (Fig. 6), assuming the Nd-Fe isotope interpretations outlined by W. Li et al. (2015) and C. Li et al., (2015) are correct (see above). If the relations shown in Fig. 6, which document basin-scale mixing of Fe sources, are considered alongside those in Fig. 16, which document in situ DIR at the site of IF deposition, the comparison seemingly indicates that DIR may operate on both large (basin-wide Fe-shuttle) and local (in situ microbial reduction) scales. Iron may be oxidised, deposited on continental shelves, reduced, shuttled to distal locations, oxidised, settled to the deep basin along with organic carbon, and then reduced in the final location of the sediment before being lithified into IF.

A seawater control on bulk-rock δ^{56}Fe trends is also seen across multiple drill cores of the Transvaal BIFs (Oonk, 2017). The mineral-fluid fractionation-specific δ^{56}Fe values of these samples indicate a similar, consistently lighter, source for carbonate and silicate bound-Fe, whereas the oxide-bound Fe tends to have more positive δ^{56}Fe values. The difference in the carbonate- versus oxide-bound δ^{56}Fe signals could be causally linked to DIR or to varying extents of oxidation on a basin-wide scale (e.g., Oonk, 2017).

2.7. Iron formations as tracers of seawater redox

Iron formations are among the most widely used lithologies to investigate the composition of the ancient oceans because their precursor minerals, such as Fe(III)-oxyhydroxides, are likely to retain the chemical signature of seawater (e.g., Bau and Dulski, 1996; Jacobsen and Pimentel-Klose, 1988b; Bjerrum and Canfield, 2002; Bolhar et al., 2004; Robbins et al., 2015, 2016). Moreover, many IFs contain low concentrations of crustal-sourced elements, such as Al, Ti, Zr, Th, Hf, and Sc, implying an authigenic origin and the preservation of geochemical signatures that are uncontaminated by continental detritus.

Manganese, the most abundant redox-sensitive element in IF after Fe (Klein, 2005), is potentially a very important candidate to use for tracking seawater redox changes across periods of IF deposition. To oxidise Mn(II), the oxidation state of the basin needs to be significantly higher than that required for Fe(II) oxidation. In the pre-GOE BIFs of the Transvaal Supergroup, Mn is only present in its divalent form in carbonate minerals and its concentration increases significantly stratigraphically upwards from the Kuruman to the Griquatown and Koegas IFs (Kurzweil et al., 2016; Oonk, 2017). This pattern indicates a relative Mn enrichment in the basin with time, either passively or due to effective reductive cycling of Mn(IV) oxyhydroxides during IF deposition. However, at present, there is no conclusive evidence in the Transvaal IF for either the primary oxidative mechanism for episodic Mn sequestration (i.e., aerobic versus photoferrotrophic), nor for the relative role of Mn(II) incorporation into carbonates directly as Mn(II) from pore-fluid or indirectly through diagenetic bacterial reduction of Mn(IV) oxyhydroxides.

In addition to constraining the secular trend in the magnitude of Eu anomaly in Superior-type IF (discussed above), REE + Y studies have also focused on Ce anomalies as tracers of water column redox behaviour. These studies have drawn from a sound understanding of REE + Y cycling in modern anoxic basins. In general, oxygenated marine settings display a strong negative Ce anomaly when normalised to a shale composite ($Ce_{(SN)}$), because oxidation of Ce(III) to Ce(IV) greatly reduces Ce solubility, resulting in its preferential removal onto Mn(IV)-Fe(III)-oxyhydroxides, organic matter, and clay particles (Byrne and Sholkovitz, 1996; Bau and Koschinsky, 2009). This process leaves the residual water column depleted in Ce, thus creating the characteristic negative Ce anomaly. In contrast, suboxic and anoxic waters lack significant negative $Ce_{(SN)}$ anomalies due to reductive dissolution of settling Mn(IV)-Fe(III)-oxyhydroxide particles (German et al., 1991; Byrne and Sholkovitz, 1996). Similarly, depletion of light REE + Y develops in oxygenated waters owing to preferential removal of LREE versus HREE onto Mn(IV)-Fe(III)-oxyhydroxides and other particle-reactive surfaces. As a result, the ratio of light to heavy REEs markedly increases across redox boundaries due to reductive dissolution of Mn(IV)-Fe(III)-oxyhydroxides (German et al., 1991; Byrne and Sholkovitz, 1996).

In many Archaean and early Palaeoproterozoic IFs there are no Ce anomalies (Planavsky et al., 2010a), and thus no deviation from trivalent Ce behaviour (e.g., Fryer, 1977a; Bau and Möller, 1993; Bau et al., 1997; Alexander et al., 2008; Frei et al., 2008). This suggests that the water column from which Fe(III) oxyhydroxides precipitated was relatively anoxic, or at least below the Eh of the Ce^{4+}/Ce^{3+} redox couple (Bau and Dulski, 1996). It is also important to consider the rates of Ce^{3+} oxidation and potential inhibition mechanisms, such as the presence of Fe^{2+} and Mn^{2+} (e.g., Moffett, 1994). Several studies have reported cases of Ce anomalies in Archaean IF (e.g., Kato et al., 2006), but many of these cases can be linked to analytical artefacts or the analysis of samples that have experienced supergene alteration (for details see Braun et al., 1990; Valeton et al., 1997). Additional work is needed to verify the existence of extensive Ce(III) oxidation in the Archaean. In this regard, a novel and potentially valuable tool for moving forward may be the use of Ce stable isotopes, which in combination with Ce anomalies, have recently been shown to provide a more nuanced understanding of redox conditions in modern hot springs and ferromanganese crusts, and hence, may be favourable for studies of strata pre- and contemporaneous to the GOE (Nakada et al., 2016). Additionally, it is important to note that Ce anomalies need not develop solely within the water column of a basin. For instance, Ce anomalies can develop in groundwater systems (Johanneson et al., 2006).

There also appear to be differences in trivalent REE + Y behaviour in IFs before and after the permanent rise of atmospheric oxygen (Fig. 17). Late Palaeoproterozoic IFs show significant ranges in light-to-heavy REE ($Pr/Yb_{(SN)}$) and Y/Ho ratios, which likely reflect variable fractionation of REE + Y by Mn(IV)-Fe(III)-oxyhydroxide precipitation and dissolution (Planavsky et al., 2010a). This interpretation implies deposition of late Palaeoproterozoic IF at ca. 1.88 Ga in basins having varied redox conditions and a strong redoxcline separating an upper oxic water column from deeper waters that were suboxic to anoxic (Planavsky et al., 2009). These ranges are similar to those seen in modern anoxic basins. In contrast, most Archaean and early Palaeoproterozoic IFs deposited before the rise of atmospheric oxygen are characterised by light REE + Y depletion (Planavsky et al., 2010a). This consistent depletion in LREE suggests the lack of a discrete redoxcline during this time period and points toward O_2-independent Fe (II) oxidation mechanisms.

3. Neoarchaean-Palaeoproterozoic iron formations

The Neoarchaean to middle Palaeoproterozoic (~2.8–1.9 Ga) marks one of the most important periods in Earth history, with several major interlinked environmental and biological evolutionary events. These include, among others, the oxygenation of the atmosphere – the GOE (Bekker et al., 2004; Konhauser et al., 2011; Gumsley et al., 2017). The GOE represents a transition from an atmosphere that was essentially devoid of free oxygen ($O_2 \ll 10^{-5}$ PAL) to one with O_2 concentrations $> 10^{-5}$ PAL, where estimates of oxygen levels are based on modelling mass-independent S isotope (S-MIF) variations (Pavlov and Kasting, 2002). In the rock record, this event is manifested by a number of changes (see Farquhar et al., 2011, 2014, for reviews), including (1) loss of easily oxidisable detrital uraninite, pyrite, and siderite from fluvial siliciclastic sediments at ca. 2.4 Ga (e.g., Rasmussen and Buick, 1999; England et al., 2002; Hofmann et al., 2009; Johnson et al., 2014); (2) loss of iron from ancient soil horizons (paleosols) older than ca. 2.4 Ga because of greater iron solubility under reducing conditions (e.g., Rye and Holland, 1998); (3) the appearance of red beds after ca. 2.3 Ga (e.g., Roscoe, 1969; Chandler, 1980; Melezhik et al., 2005; Bankole et al., 2016); (4) the loss of S-MIF in sulfide and sulfate minerals in sedimentary rocks deposited after 2.3 Ga (Farquhar et al.,

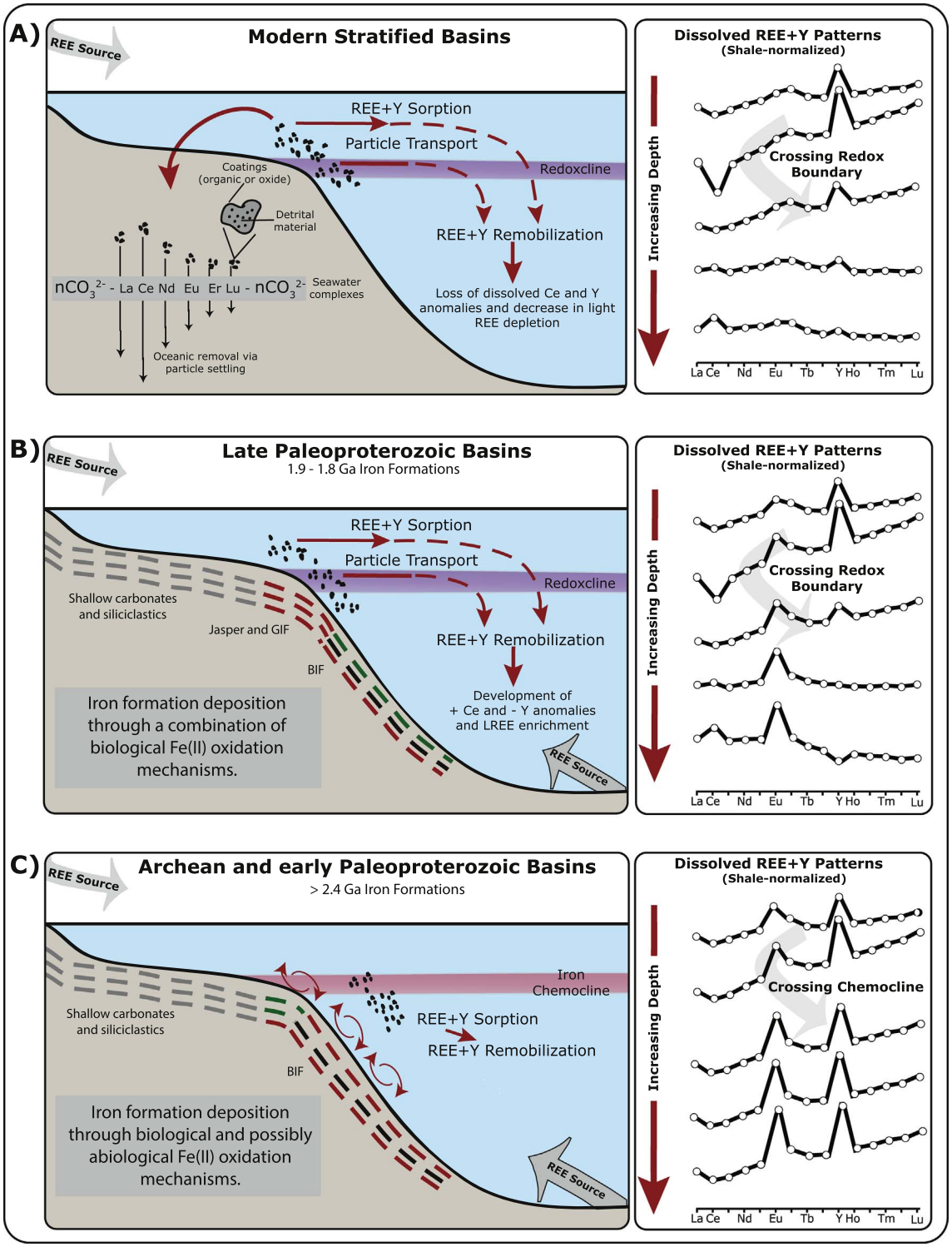

Fig. 17. Model for the evolution of ocean redox structure based on REE patterns in well-preserved IF. Mn(IV)-poor IF are likely to record seawater REE + Y patterns. Similar to modern redox-stratified basins (A), REE + Y pattern of late Paleoproterozoic IF (B) records evidence for a shuttle of metal and Ce oxides from oxic shallow seawater across the redoxcline. Mn(IV)-hydroxide dissolution in anoxic water column lowers Y/Ho ratios, raises LREE to HREE ratios, and increases Ce concentration relative to neighboring REE (La and Pr). In contrast, Archaean IF do not display REE + Y pattern indicative of a strong oxide shuttle (C), which implies a lack of significant Mn-cycling across a redoxcline in many Archaean IF-bearing basins. Absence of discrete redoxcline points toward microbial Fe(II) oxidation, rather than a direct reaction of Fe(II) with O_2. Modified from Planavsky et al. (2010a).

2000; Bekker et al., 2004; Papineau et al., 2007; Partridge et al., 2008; Guo et al., 2009; Williford et al., 2011; Luo et al., 2016; Gumsley et al., 2017); and (5) the increase in Cr and U contents in IF at 2.45 Ga that records the onset of oxidative continental weathering (Konhauser et al., 2011; Partin et al., 2013a).

3.1. Iron formations deposited before the GOE

Iron formations deposited between 2.60 and 2.45 Ga are the most laterally extensive and economically valuable of any in Earth history. The 2.60 Ga Marra Mamba Formation of the Hamersley Province in Western Australia is one of the thickest IFs in the geologic record. It was

deposited in a deep-water basinal setting adjacent to a passive margin during the sea-level highstand of the Marra Mamba basin, and has an average outcrop thickness of about 210 m (Trendall and Blockley, 1970; Krapež et al., 2003). The Marra Mamba IF carries a pronounced positive Eu anomaly (Alibert and McCulloch, 1993), suggesting a strong hydrothermal imprint on the REE systematics during its deposition, although, as noted above (Fig. 6), Nd isotope data suggest a mixture of continental and hydrothermal REE + Y sources. Further, the Marra Mamba IF is dominated by magnetite, ankerite, and fibrous silicate (Baur et al., 1985), which suggests excess organic carbon was present during diagenesis. Support for this interpretation is found in negative $\delta^{13}C$ values that increase with increasing magnetite abundance (Baur et al., 1985).

Major IF deposition occurred between 2.50 and 2.40 Ga in association with a series of mantle plume breakout events (e.g., Heaman, 1997) and was immediately preceded by the final stage in the supercontinent assembly of the Gawler Craton (South Australia), North China Craton, East Antarctica Craton, and in the central Indian tectonic zone of India (Barley et al., 2005). Deposition of these IFs occurred on a reactivated continental margin (Krapež et al., 2003), followed by a rise in sea level. Isley and Abbott (1999) estimated that during those 100 m.y., perhaps as much as 60% of the global volume of preserved IF was deposited.

The largest IFs by mass are associated with the Brockman Iron Formation in the Hamersley Group of the Pilbara Craton in Western Australia (Isley, 1995; Trendall and Blockley, 2004). The Brockman Iron Formation is divided into four lithostratigraphic units, namely the lowermost Dales Gorge Member (BIF), the Whaleback Shale Member, the Joffre Member (BIF), and the uppermost Yandicoogina Shale Member (Fig. 18). Overlying the Brockman Iron Formation are two more BIF units, the Weeli Wolli Formation and the Boolgeeda Iron Formation. The best age estimates for the deposition of the Dales Gorge and Joffre members are 2494–2464 Ma (Trendall et al., 2004) and 2454 ± 3 Ma (Pickard, 2002), respectively. The consensus view is that the Brockman Iron Formation was deposited on a large, stable, and clastic-starved continental platform, which was only influenced by episodic inputs of fine-grained tuffaceous detritus (e.g., Ewers and Morris, 1981; Gross, 1983). Barley et al. (1997) suggested that deposition of the Hamersley IFs was possibly linked to major submarine magmatic plume activity in the form of a large igneous province (LIP). Morris (1993) also proposed that the depositional environment for the Hamersley BIFs included a steady source of silica and iron, and a water depth shallow enough to form large carbonate platforms.

From a geochemical standpoint, the Brockman Iron Formation portrays characteristics common to pre-GOE IFs. Typical seawater REE + Y patterns are displayed by the Dales Gorge Member, including low Pr/Yb_{SN} (0.08–0.3), low Sm/Yb_{SN} (0.1–0.4), positive La anomalies, positive Eu anomalies, and superchondritic Y/Ho ratios (Pecoits et al., 2009). However, the Dales Gorge Member lacks a true negative Ce anomaly, suggesting low-oxygen conditions at the time of deposition. The Dales Gorge Member is also composed of relatively pure chemical precipitates, as supported by low Al, Ti, Th, Zr, Hf, and Sc concentrations (Pecoits et al., 2009). Based on bulk-sample analysis, Becker and Clayton (1976) noted isotopic exchange between minerals within the Dales Gorge Member at burial metamorphic temperatures of 270 to 310 °C, and suggested that oxygen isotopes in quartz and carbonate

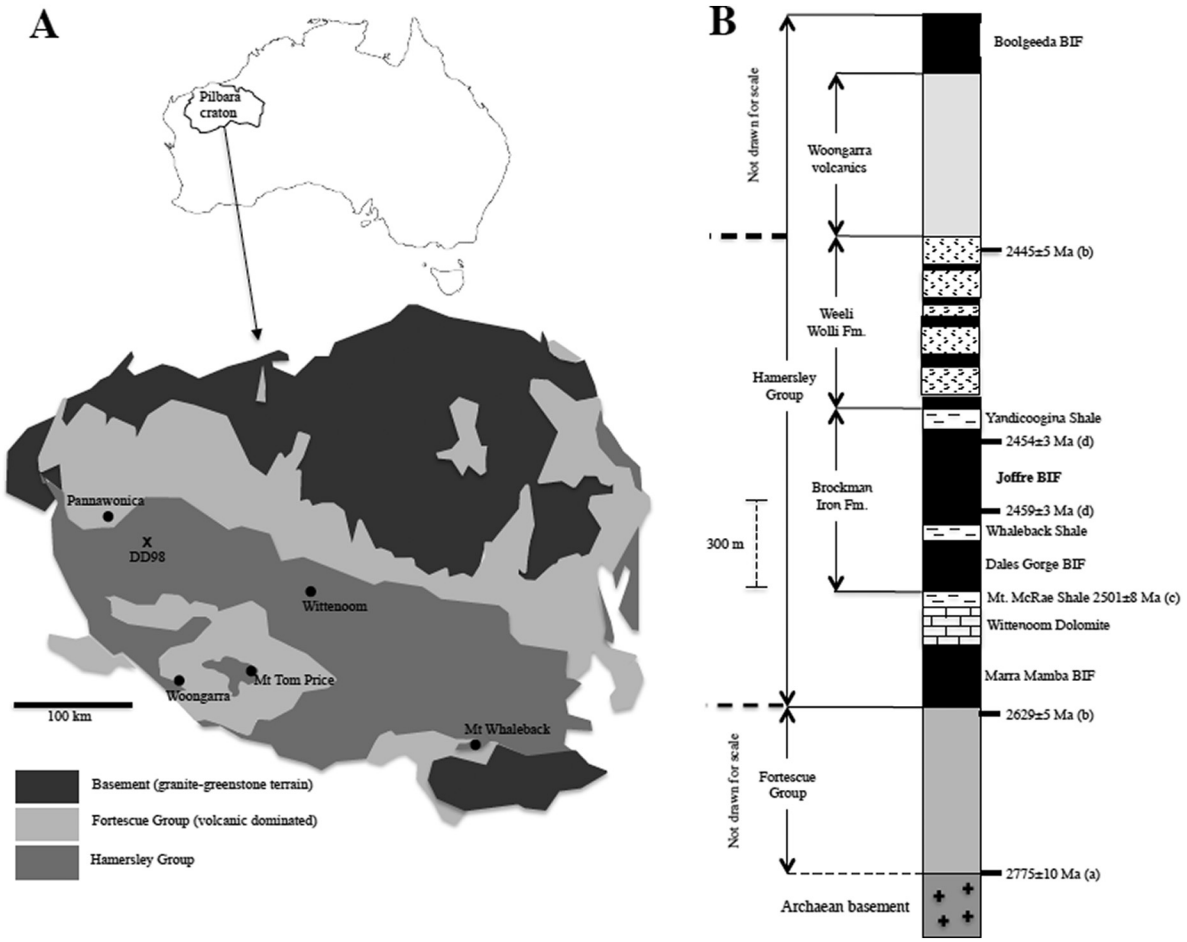

Fig. 18. (A) Regional geology and (B) stratigraphy of the Hamersley Group, Western Australia (modified from Haugaard et al., 2016b). Thickness and age data from: (a) Arndt et al., 1991; (b) Trendall et al., 2004; (c) Anbar et al., 2007; and (d) Pickard, 2002.

may have equilibrated completely. Hematite, on the other hand, underwent negligible change in oxygen isotopes. Detailed in situ oxygen isotope analysis (Li et al., 2013a), as discussed above (Fig. 8), documents multiple generations of oxides and suggests a primary precipitation temperature as low as ~25 °C.

The low abundance of Al_2O_3 and TiO_2 within the Joffre Member also suggests limited continental epiclastic input. However, the Joffre Member contains many stilpnomelane granules of compositions that appear to record a mixture of volcanic (pyroclastic) and chemical components, thus making it a poor chemical proxy for atmospheric conditions at the time of deposition (Haugaard et al., 2016b). Compared to the underlying Dales Gorge Member, the Joffre Member has significantly higher REE concentrations (Pecoits et al., 2009; Haugaard et al., 2016b). The two IFs display similar REE + Y patterns, including large Eu anomalies; however, the Joffre Member lacks a strong positive Y anomaly, which is typically associated with a seawater geochemical signature. A negative Ce anomaly is absent in the REE + Y plots of the Joffre Member as well, suggesting O_2 levels below the Ce(III)/Ce(IV) redox boundary. Iron isotope compositions in both the Joffre and the Dales Gorge members show a wide range in δ^{56}Fe values, indicating multiple Fe sources and pathways (Fig. 6), where average δ^{56}Fe values in the Joffre Member are heavier than those of the Dales Gorge Member (Johnson et al., 2008b; Pecoits et al., 2009; Li et al., 2013a; Haugaard et al., 2016b).

The Weeli Wolli Formation displays a marked increase in Cr concentrations, interpreted by Konhauser et al. (2011) as a remnant signature of bacterial pyrite oxidation and associated acid rock drainage. Aside from this work, few geochemical analyses have been carried out on this formation. A lack of geochemical data is also apparent for the Boolgeeda Iron Formation, which was deposited at ~2.45 Ga and represents the terminal IF deposit in the Hamersley Basin. High-resolution chemo-stratigraphic profiling of both the Weeli Wolli and the Boolgeeda IF are currently being persued, and it is anticipated that these data will help elucidate the transition from anoxic to oxic conditions on early Earth, and potentially develop geochemical ties to time-correlative basins worldwide.

The major IFs of South Africa are developed in the Griqualand West Basin of the 2–6-2.4 Ga Transvaal Supergroup, and comprise the Kuruman and Griquatown formations and BIFs of the Koegas Subgroup (Fig. 19). Beukes and Gutzmer (2008) presented detailed correlations between the Hamersley and Transvaal BIFs, and suggest that these sequences reflect deposition in the same basin, as originally proposed by Button (1976) and then Cheney (1996), although it cannot be ruled out that they were two separate, but coeval basins. The contact-metamorphosed Penge BIF of the eastern Transvaal Basin is considered to be the lithostratigraphic equivalent of the Kuruman BIF and is not discussed further here. In the Griqualand West Basin, the BIFs constitute the upper Ghaap Group of the lower Transvaal Supergroup (Asbestos Hills Subgroup), whereas carbonate rocks of the Campbellrand Subgroup dominate the lower Ghaap Group (Beukes and Gutzmer, 2008). The regional transition from the stromatolitic Gamohaan Formation upward into the Kuruman BIF is continuous and indicates a progressive deepening of the basin (Klein and Beukes, 1989; Sumner, 1997). The rhythmically micro-banded Kuruman BIF was deposited largely in an open-shelf environment below wave base and contains multiple cycles of shallowing-upward sequences (Beukes, 1984). A SHRIMP U/Pb zircon age, determined on stilpnomelane-rich tuffaceous mudrocks, constrains the age of the top part of the Kuruman BIF at ca. 2.46 Ga (Pickard, 2003), thus making it broadly contemporaneous with the Brockman IF in Australia.

The predominantly clastic-textured, granular Griquatown IF is interpreted to have formed in a shallow water, storm-dominated depositional environment (Beukes, 1984; Beukes and Klein, 1990). The transition from Kuruman to Griquatown IF is gradual, characterised by intercalated microbanded and granular facies, and in itself is intriguing given that transitions from microbanded BIF to granular GIFs are uncommon in the pre-GOE successions (Beukes and Klein, 1990). The clastic texture in the Griquatown Formation is manifested by mm-scale granules of varying composition, typically in the same bed, developed locally into well-sorted grainstones (Beukes and Gutzmer, 2008). Other characteristic textures include soft-sediment deformation features and dm-scale chert lenses and pods that contain sprays of riebeckite in lower stratigraphic portions of the Griquatown GIF.

The Koegas Subgroup only develops in the deeper, southwestern part of the Griqualand West Basin. Its absence in the shallower parts – where the Griquatown GIF is directly overlain by the Makganyene diamictite – is explained by palaeobathymetric considerations (Moore et al., 2001; Polteau et al., 2006). The Koegas BIF represents sea-level fluctuations with alternating regressive and transgressive cycles. Iron formation deposition is thought to have taken place during transgressions, punctuated by siliciclastic deposition during regressions (Schröder et al., 2011).

Magnetite and Fe carbonates are the major iron minerals within the South African IFs (Beukes and Klein, 1990; Kurzweil et al., 2016). Although hematite micro-particles are present, they are volumetrically extremely rare (Klein and Beukes, 1989). The IFs are also generally sulfur-poor and contain minimal detrital input as recorded in very low bulk Al and Ti abundances (Beukes, 1984; Beukes and Klein, 1990; Horstmann and Hälbich, 1995). Whole-rock REE + Y patterns and their interpretations are in good agreement with those of the aforementioned Hamersley IFs of Australia (Bau and Dulski, 1996; Planavsky et al., 2010a). Manganese – deposited as discrete Mn-oxide layers in the stratigraphically younger Hotazel Formation – is incorporated entirely in iron carbonate minerals in both the Griquatown and Koegas IFs, where its bulk-rock abundance locally reaches percent levels (Tsikos and Moore, 1997; Johnson et al., 2016; Kurzweil et al., 2016).

Major IF deposits in Canada are hosted in several 2.9–2.8 Ga and 2.7–2.6 Ga greenstone belts on the Superior, Slave, Rae, and Hearne cratons. Several of these are Algoma-type IF successions that contain major gold deposits, including the ~2.71 Ga Woodburn Lake greenstone belt, the ~2.97 North Caribou greenstone belt, the ~2.7 Ga Bearmore-Geraldton greenstone belt, the ~2.7–2.6 Ga Rankin Inlet greenstone belt (Gourcerol et al., 2016), the ~2.7 Ga Hope Bay greenstone belt (Sherlock et al., 2012), and the ~2.62 Ga BIF from Damoti Lake and Back River (Haugaard et al., 2017a, 2017b). Recently, important petrological and geochemical work was carried out on the Slave Craton IF that consists of Mesoarchaean BIF of the ~2.85 Ga Central Slave Cover Group deposited in a continental rift-setting (Haugaard et al., 2016a), and Neoarchaean BIF of the 2.62 Ga Slemon Group (Haugaard et al., 2017a) deposited in a back-arc basin (Haugaard et al., 2017b).

Iron formations in the Quadrilátero Ferrífero region in Brazil, Middleback Ridge (Gawler Craton) in South Australia, Nimba and Simandou Ranges in Liberia and Guinea, Krivoy Rog area in Ukraine, and Kursk Magnetic Anomaly (KMA) region in Russia are broadly similar in age based on available geochronological and chemostratigraphical constraints, and also display similar patterns of macrobanding (Prilutzky et al., 1992; Kulik and Korzhnev, 1997; Egal et al., 2002; Bekker et al., 2003; Phillips et al., 2006; Spier et al., 2007; Szpunar et al., 2011). These IFs were also deposited on reactivated continental margins, and are separated by prominent unconformities from overlying Palaeoproterozoic sequences, which correspond to a long gap in sedimentation following the supercontinent assembly at ca. 2.40 Ga.

3.2. Minor iron formation deposition after the GOE and before ca. 1.88 Ga

Giant IFs were not deposited between ca. 2.40 and 1.88 Ga, but oolitic hematitic ironstones of the 2.32 Ga lower Timeball Hill Formation in South Africa were deposited in shallow water, above fair-weather wave base (Schweigart, 1965; Dorland, 1999). Few geochemical data are available for this unit, partly because it contains significant

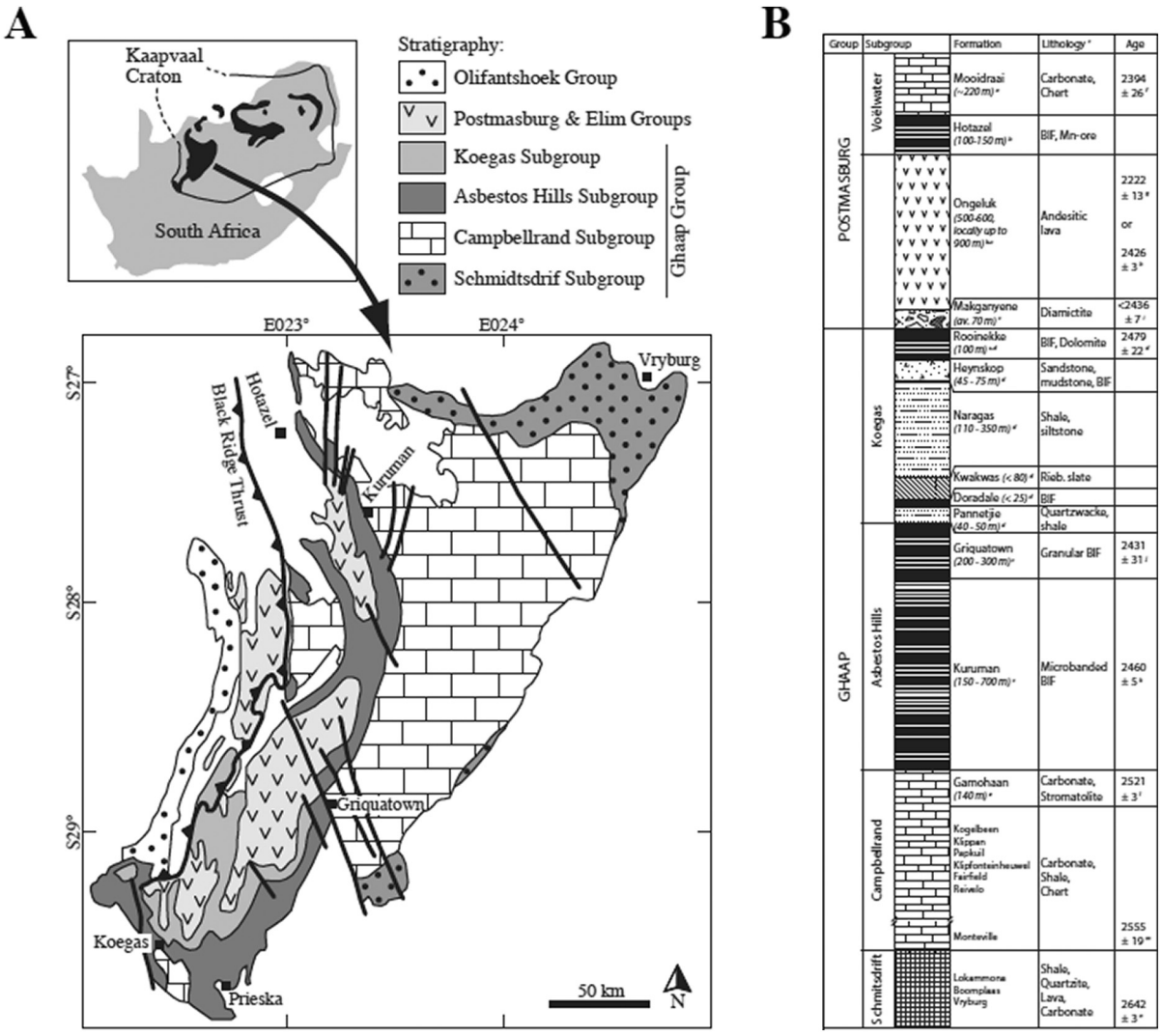

Fig. 19. (A) Regional geology and (B) stratigraphy of the Griqualand West Basin on the Kaapvaal Craton of South Africa (modified from Oonk, 2017). Thickness and age data from: (a) Kunzmann et al., 2014; (b) Tsikos et al., 2003; (c) Polteau et al., 2006; (d) Kendall et al., 2013; (e) Sumner, 1997; (f) Bau et al., 1999; (g) Cornell et al., 1996; (h) Gumsley et al., 2017; (i) Moore et al., 2012; (j) Trendall et al., 1990; (k) Pickard, 2003; (l) Sumner and Bowring, 1996; (m) Altermann and Nelson, 1998; and (n) Walraven and Martini, 1995.

amounts of siliciclastic material. Its deposition at ca. 2.32 Ga (Hannah et al., 2004) may coincide with a magmatic event at that time (e.g., Eriksson et al., 1994a, 1994b; Fetter et al., 2000; Berman et al., 2005; Hartlaub et al., 2007; Rasmussen et al., 2013; Partin et al., 2014). However, the significance of this magmatic event is poorly known. Correlative IFs are not documented on other continents.

The 2.43 Ga Hotazel Formation, whose date of formation has recently been revised from earlier estimates of 2.2 Ga (Gumsley et al., 2017), contains the largest known manganese deposit in the world (Tsikos et al., 2003). The manganese (and iron) formation lies above basaltic andesites of the Ongeluk Formation and has been interpreted previously as a volcanogenic deposit (Cornell and Schütte, 1995). The iron- and manganese-rich succession of the Hotazel Formation consists of three symmetric cycles of Mn-rich carbonate-braunite lutite, intercalated with magnetite-rich microbanded BIF (Tsikos and Moore, 1997). The entire sequence is thought to have been deposited in a continental shelf environment that was starved of terrigenous siliciclastic input (Schneiderhan et al., 2006). The Hotazel Mn-Fe deposits lack positive Eu anomalies, pointing to an extremely dilute hydrothermal signal at best. The significance of weak Ce anomalies remains contentious considering co-existing positive La anomalies (Tsikos and Moore, 1997). Whereas the Ongeluk volcanics cannot be discounted as a possible source of at least some of the Fe and Mn in the basin through low-temperature seafloor alteration, recent applications of combined iron isotope geochemistry and Mn/Fe ratios suggest that enrichment in the Hotazel palaeobasin in Mn and isotopically light Fe could have ensued progressively through prior protracted deposition of Mn-poor, high δ^{56}Fe BIF (Tsikos et al., 2010). Indeed, the new age constraints for the Hotazel Formation (Gumsley et al., 2017), and the Fe isotope and Mn-enriched signature of the uppermost Griquatown and Koegas IFs in the Transvaal Supergroup (Kurzweil et al., 2016; Oonk, 2017), lend strong support to this interpretation.

The 2.3–2.2 Ga Yuanjiacun BIF, located in Shanxi Province, is likely the most representative Superior-type IF in the North China Craton (NCC) and arguably the largest and most extensive IF (> 10 Gt) deposited during this time period (Li et al., 2010; Hou et al., 2014). The transition from deep-water carbonate facies to shallow-water oxide facies is accompanied by a change in mineralogical composition from siderite through magnetite-ankerite and magnetite-stilpnomelane-assemblages in the transition zone, to magnetite, and then hematite near the palaeoshore. The deposition of BIF immediately following the onset of the GOE confirms that deep marine waters were still episodically ferruginous at that time, but that shallow waters were sufficiently oxygenated such that Fe(II) oxidation no longer needed to be directly tied to proximal and in situ cyanobacterial activity (Wang et al., 2015, 2016).

Hematitic oolites and hematite-rich sandstones continued to be deposited in shallow-marine environments during the ca. 2.25 to 2.10 Ga Lomagundi carbon isotope excursion in South Africa (Silverton Formation; Schweigart, 1965) and on the Kola Peninsula in Russia (Kuetsjärvi Sedimentary Formation; Akhmedov, 1972a). The IFs deposited during the Lomagundi excursion include those within the Ijil Group, Mauritania (Bronner and Chauvel, 1979) and the Lomagundi Group, Zimbabwe (Master, 1991). The former belongs to the 2.20–2.10 Ga Birimian Basin in West Africa, which also contains iron and manganese formations in the Francevillian Basin, Gabon (Leclerc and Weber, 1980) and in the Nigerian schist belts (Mücke, 2005). The latter developed within the ca. 2.2–2.1 Ga Magondi Basin (Master, 1991; Master et al., 2010). Volcanic-hosted IFs deposited during the Lomagundi carbon isotope excursion are known in Brazil (e.g., Aimbė Formation, Guarinos Group; Resende and Jost, 2002; Itapicuru Complex of the Rio Itapicuru greenstone belt; Dalton de Souza et al., 2003), and Norway (Iddjajav'ri Group, Karasjok greenstone belt; Often, 1985).

Iron formations deposited between 2.40 and 2.10 Ga are distinctly different in scale, and in most cases, the depositional setting differs from those in the Archaean. It seems that either the deep-ocean redox state was too oxidised, relative to the strength of hydrothermal input, to form giant sedimentary iron deposits during this time interval, or that marine sulfate levels were high enough that the sulfide produced during bacterial sulfate reduction exceeded the hydrothermal Fe(II) supply – in this case iron sulfides would precipitate instead of iron oxides (see Kump and Seyfried, 2005 for further discussion). Several independent lines of evidence point toward high (mM) sulfate levels during the Lomagundi Event (Schröder et al., 2008; Planavsky et al., 2012; Scott et al., 2014), consistent with the idea that growth of the marine sulfate reservoir consumed the hydrothermal Fe(II) flux, which ultimately exerted a first-order control on the distribution and abundance of IF.

Following the end of the Lomagundi carbon isotope excursion at ca. 2.10 Ga, small Algoma-type IFs were deposited in several basins in North America (e.g., Homestake Iron Formation, Black Hills, South Dakota; Frei et al., 2008) and Finland (Paakola, 1971; Laajoki and Saikkonen, 1977). Oolitic hematitic ironstone is also present in the Kolasjoki Formation, Kola Peninsula, Russia (Akhmedov, 1972b). Finally, economic-grade, shallow-water IFs of the 2.05 Ga Costa Sena Group (underlying the Espinhaço Group) and likely correlative Serra do Sapo Formation of the Serra de Serpentina Group were deposited in an intracratonic basin in central Brazil (Rolim et al., 2016). Combined, these data tentatively suggest that dynamic ocean redox conditions were established in the aftermath of the GOE, with periodic upwelling of Fe(II) into shallow-water settings above storm and fair-weather wave base. However, it is also possible that these small, locally-developed IFs were linked to local, continental sources of iron (e.g., Fe-rich groundwater) rather than to upwelling of ferruginous waters. This alternative explanation has not been tested so far and requires further consideration.

An exciting, and perhaps unexpected, finding to come out of some recent studies on secular trends in trace metal contents of IFs (and black shales) is that Earth's redox state during the Precambrian may have been much more complex than previously thought. Partin et al. (2013a) and Partin et al. (2013b) recently showed that directly following a dramatic increase in the oceanic uranium reservoir during the GOE, the U reservoir decreased significantly after ca. 2.10 Ga, resulting in a U content in IFs and shales that was only marginally higher than pre-GOE levels. Given that the oxygen content of the oceans directly controls seawater U concentrations once oxidative continental weathering was established, the observed decrease could be due to a subsequent drop in the level of atmospheric and seawater oxygen following the Lomagundi event. It seems plausible that net organic carbon burial associated with oxygen production during the Lomagundi event later became an oxygen sink as organic matter became oxidised, driving oxygen to low levels that may have persisted for some hundreds of million years thereafter (Bekker and Holland, 2012; Canfield et al., 2013).

3.3. The ca. 1.88 Ga resurgence in iron formations

Extensive and large IFs reappeared after an approximately 500 m.y. gap, at about 1.88 Ga. These successions contain an abundance of GIF, relative to Archaean and early Palaeoproterozoic BIF. The most extensive 1.88 Ga GIF occur in North America along the southern and eastern margins of the Superior Craton (Animikie and Mistassini basins and Labrador Trough; Simonson, 2003) and in Western Australia (Nabberu Basin; Rasmussen et al., 2012). These GIFs are coeval with emplacement of a ca. 1.88 Ga ultramafic to mafic LIP (Heaman et al., 1986, 2009; Hulbert et al., 2005) that is potentially related to a mantle plume breakout event during the early assembly of the supercontinent Nuna/Columbia (Hamilton et al., 2009; for an opposing view, see Heaman et al., 2009). Recognised now to be correlative based on high-precision geochronology (Findlay et al., 1995; Machado et al., 1997; Fralick et al., 2002; Schneider et al., 2002; Stott et al., 2010), the North American GIFs extend discontinuously at the surface for > 3000 km along the southern and eastern margins of the Superior Craton, from Ontario, through Minnesota, Wisconsin, and Michigan, to Québec (Mistassini Basin) and the Labrador Trough. Despite poor exposure, these iron deposits are easily traceable by magnetic anomalies. Correlative and texturally similar GIF are also recognised in the northern part of the Superior Craton in the Hudson Bay region (Richmond Bay and Belchers islands) and in the Sutton Inliers, and are considered to have been deposited in extensional basins coeval with submarine basaltic volcanism (Fralick et al., 2002; Schulz and Cannon, 2007; Ricketts et al., 1982). Some workers have proposed a back-arc setting (Fralick et al., 2002; Schulz and Cannon, 2007), whereas others have advocated a foreland basin setting (Hoffman, 1987; Ojakangas et al., 2001; Schneider et al., 2002).

An intriguing question is whether deposition of these GIF represents local, basin-scale conditions or the global ocean composition and redox state. This is a critical issue because the occurrences and ages of these rocks have been used by some workers to infer deep-water anoxic conditions in the coeval global ocean (e.g., Poulton et al., 2004; Slack and Cannon, 2009). However, if deposition of these GIF reflects restricted, basin-scale conditions (Pufahl et al., 2010), our understanding of the ocean redox state may be incorrect. Present palaeogeographic reconstructions are insufficient to answer this question; although tidal signatures have been observed in GIF and interbedded sedimentary rocks in Minnesota and the Hudson Bay region (Ojakangas, 1983; Chandler, 1984), which is consistent with at least periodically open-marine conditions, albeit very shallow, during IF deposition.

The ca. 1.88 Ga Frere Iron Formation, part of the Yilgarn Craton of Western Australia (Goode et al., 1983; Rasmussen et al., 2012), and GIF of the Gibraltar Formation in the Kahochella Group, from the southeastern margin of the Slave Craton that is interbedded with the ~1.9 Ga Akaitcho Formation at its base (Bowring et al., 1984; Roscoe et al., 1987; Hoffman et al., 2011), are age equivalent to the Lake Superior GIF. Notably, a ~20-m-thick magnetite-hematite oolitic GIF is present in the middle member of the Watterson Formation (Hurwitz Group) on the Hearne Craton (Miller and Reading, 1993). The age of this oolitic unit is not well constrained, but ages of detrital zircons in the Hurwitz Group suggest that it is younger than 1.9 Ga (Davis et al., 2005). In addition, the presence of IF in the ca. 1.88 Ga Rochford Formation developed on the eastern margin of the Wyoming Craton supports synchronous deposition of IF on several cratons, even though this IF deposit is poorly dated and not granular (Frei et al., 2008).

Deposition of IF on the Superior Craton is coincident with a peak in tonnage for VMS deposits, some of which were positioned in island arcs. VMS deposits of this age are known in the hinterland to the south of the Animikie Basin (Schulz and Cannon, 2007), in the Labrador Trough (Barrett et al., 1988), and in the Trans-Hudson orogen (Syme and Bailes, 1993). Submarine volcanic rocks of the Pembine-Wausau terrane of northern Wisconsin were deposited at ca. 1.88 Ga, contemporaneously with GIF of the Animikie Basin (Schulz and Cannon,

2008). These data also suggest that the hydrothermal systems were likely the source of iron, consistent with earlier models (e.g., Isley, 1995). Iron-oxide exhalites are conspicuously absent at or near these deep-water VMS deposits that presumably formed under open-marine conditions. This observation is unlikely to reflect preservational bias because slightly younger 1.84, 1.79, and 1.78 Ga Cu-rich VMS deposits that similarly formed in arc settings contain abundant hematite and magnetite exhalites, jasper, and IF (Slack et al., 2007; Slack and Cannon, 2009; Bekker et al., 2010). This association points to an anoxic and ferruginous composition of deep waters in open-marine settings at ca. 1.88 Ga. Furthermore, assuming that the iron was hydrothermally derived, there must have been a crash, potentially to Archaean levels, of the marine sulfate reservoir, which would have fostered iron-rich rather than sulfide-rich hydrothermal fluids (Kump and Seyfried, 2005). Again, this conclusion is based on the premise that the redox state and chemical composition of seawater-derived hydrothermal fluids are strongly influenced by the concentration of the main oxidant in seawater—sulfate. Consistent with this interpretation, the ca. 1.88 Ga GIF are commonly overlain by black sulfidic shales, which record the later development of euxinic conditions in parts of the Animikie Basin (e.g., Poulton et al., 2004, 2010).

The Animikie Basin contains another stratigraphic level with regionally extensive IFs. This level is stratigraphically above the 1.85 Ga Sudbury impact ejecta layer and is older than the ca. 1.83 Ga regional metamorphic event related to the Penokean orogeny (Cannon et al., 2010). These IFs are mineralogically and texturally different from the ca. 1.88 Ga GIF and were likely deposited in deeper waters, below fair-weather wave base, and, probably, even below storm wave base. They are developed in the: (1) Marquette Iron Range, Michigan (~60-m-thick Bijiki Iron-Formation Member of the Michigamme Slate containing siderite, chert, iron oxides, and silicates; Ojakangas, 1994; Ojakangas et al., 2001; Cannon et al., 2010); (2) Iron River-Crystal Falls Iron Ranges in Michigan (~15-m-thick chert-siderite slate of the Stambaugh Formation; James et al., 1968); and (3) Gogebic Iron Range, Wisconsin (~47-m-thick IF of the Tyler Formation consisting of chert and siderite; Schmidt, 1980; Cannon et al., 2008). Deposition of these IFs might be genetically linked to submarine mafic volcanism in the Animikie Basin based on spatial association with, for example, the Badwater Greenstone, but this relationship has not been documented in detail. The presence of these units indicates that the conditions necessary for IF deposition in marine settings were re-established in the Animikie Basin after 1.85 Ga, in association with mafic volcanism.

3.4. Proterozoic age gap in Superior-type IF deposition

It is generally assumed that after ca. 1.85 Ga, Superior-type IFs were not deposited for approximately 1.1 b.y. until precipitation of Rapitan-type IF, associated with the Sturtian glaciation and extensional magmatism linked to the breakup of Rodinia (Isley and Abbott, 1999; Huston and Logan, 2004; Klein, 2005; Slack and Cannon, 2009). This gap has been explained by a shift to fully oxic (Holland, 1984), sulfidic (Canfield, 1998), or suboxic (Slack et al., 2007, 2009) deep-ocean conditions. The earlier suggestion of oxic deep-ocean conditions after ca. 1.88 Ga (Holland, 1984) was challenged by the proposal that deep-ocean conditions were predominantly euxinic (anoxic and sulfidic) until full ocean ventilation during the late Neoproterozoic or earliest Phanerozoic (e.g., Canfield, 1998; Poulton et al., 2004). This interpretation was grounded in a simple modelling approach suggesting that full-ocean ventilation would be difficult, given most current estimates for atmospheric oxygen levels in the Mesoproterozoic.

Although there are a few instances of locally developed mid-Proterozoic euxinia (e.g., Shen et al., 2003; Brocks et al., 2005; Lyons et al., 2009), the idea of global-scale deep euxinia has also recently fallen out of favour. All available data that constrain the marine landscape in the mid-Proterozoic ocean are consistent with only locally developed euxinic conditions along productive continental margins (e.g., in oxygen-minimum zones) or within intracratonic basins (Scott et al., 2008; Poulton et al., 2010; Planavsky et al., 2011; Lyons et al., 2012; Reinhard et al., 2013). The emerging consensus is that the redox state of the deep ocean was spatially and temporally variable during the mid-Proterozoic but was generally at a low oxidation state (e.g., Planavsky et al., 2011). Poulton et al. (2010) argued that euxinic shales deposited on continental margins in oxygen-minimum zones and in intracratonic basins could have been a major sink for the hydrothermal iron flux to the mid-Proterozoic oceans and were thus responsible for the absence or scarcity of mid-Proterozoic IFs. At present, this suggestion has not been quantitatively evaluated, but it predicts very high iron contents in euxinic shales during this time interval. Data in Kump and Holland (1992) and Bekker and Holland (2012) do show that the average Proterozoic shale has more iron than the average Phanerozoic shales but less than the average Archaean shale.

Large sedimentary iron deposits that formed during this time gap (1.85–0.75 Ga) are indeed absent, but several small IFs and Fe-rich lithologies in sedimentary rock-dominated successions are known (see Bekker et al., 2010). Examples within this age group include the ca. 1.7 Ga Freedom Formation of the Lower Baraboo Series, Wisconsin, which contains banded ferruginous chert in the lower part interlayered with siderite- and kaolinite-rich slate, collectively ranging from 60 to 160 m thick (Weidman, 1904; Leith, 1935; Van Wyck and Norman, 2004). The broadly correlative metasedimentary succession of the Tomiko terrane in Ontario contains a magnetite-chert IF (Easton, 2005). The ca. 1.7 Ga Canjica Formation of the Serra de São José Group of the Serpintina Range, and the correlative and economically important Morro Escuro Ridge Sequence of the Espinhaço Group (both in Brazil), were deposited in an intracratonic (rift) basin and contain alternations of hematite and magnetite with quartz (Braga et al., 2015; Rolim et al., 2016). Additionally, the Chuanlinggou Formation of the North China Craton, a classic GIF deposit, appears to be latest Palaeoproterozoic in age (ca. 1.7 Ga; Wan et al., 2003; Dai et al., 2004).

Even though the IFs deposited during this time interval are spatially limited, relative to giant Neoarchaean and Palaeoproterozoic deposits, their existence is significant. For example, these deposits may provide evidence for episodic upwelling of hydrothermal iron from deep-water oceanic settings from ca. 1.85 to 0.8 Ga. That said, these units are still poorly studied, and we cannot rule out alternative depositional models (e.g., Fe-rich groundwater, local shallow-water hydrothermal iron sources, and iron recycled from sediments deposited in inner-shelf mud belts). Between 1.85 and 0.8 Ga, open-marine, deep-water environments may, in some cases, have been sufficiently oxygenated to oxidise and precipitate Fe(II) from hydrothermal plumes as Fe(III) oxyhydroxides (e.g., Slack et al., 2007, 2009), whereas evidence for Mn(II) oxidation in the deep ocean is generally lacking. Although this record of the Fe cycle does not provide strong quantitative constraints on the deep-ocean redox state, it questions models invoking either fully oxic or fully sulfidic conditions throughout the deep ocean in the mid-Proterozoic. Again, in terms of time and space, a low but variable redox state in the deep ocean is most consistent with the record of Mesoproterozoic iron deposits.

4. Iron formations, primary productivity, and atmospheric oxygenation

Although there is still debate about the dynamics of initial atmospheric oxygenation, herein we present a coherent model for the rise of atmospheric O_2. Underpinning this transition was the evolution of cyanobacteria and the oxygen they generated. Importantly, it needs to be reiterated that oxygenation of the shallow oceans likely preceded that of the atmosphere. As discussed above, several lines of evidence tentatively point to their evolution by at least 3.0 Ga, and perhaps even earlier.

If cyanobacteria evolved by 3.0 Ga or before, the obvious question is why did it take several hundred million years for oxygen to accumulate

in the atmosphere? To maintain low atmospheric oxygen levels despite O_2 production in the oceans requires that oxygen sinks must have been much larger than they are now (including reduced solutes in seawater, volcanic gases, or crust), or the oxygen flux was greatly reduced (due to limited cyanobacterial productivity), or both. It is vital to remember that most organic matter produced in the upper water column will be remineralised before reaching the seafloor, even if there is a surge in productivity associated with the evolution of cyanobacteria. And, this relationship will likely hold even if marine sulfate levels were very low (e.g., 100 μM). Therefore, oxygen flux calculations on local or global scales need to consider the very large offset between export and primary production. That being said, there should be an oxygen flux to the atmosphere in the Archaean in the presence of cyanobacterial production; exactly how oxygen levels were buffered at very low levels remains an unresolved question. In this regard, there are several possibilities: (1) cyanobacteria were nutrient starved and hence failed to generate appreciable O_2; (2) cyanobacteria were marginalised by factors other than nutrients; (3) an overabundance of reductants consumed any O_2 produced; and (4) there was limited emergence of continental landmass, which may have limited land-based cyanobacterial activity, as well as affected consumption of oxygen during weathering.

(1) The extent to which phosphorous may have limited cyanobacterial productivity in the Archaean and Proterozoic oceans remains an area of active debate. Based on the low P/Fe ratios in Archaean and Palaeoproterozoic IFs, it was proposed that seawater at that time contained limited marine phosphorous. This, in turn, would have reduced levels of photosynthesis and carbon burial, thereby inhibiting long-term oxygen production on the early Earth (Bjerrum and Canfield, 2002). This model was based on partitioning coefficients (K_D) derived for P to Fe(III) oxyhydroxides associated with modern hydrothermal plumes. However, because the K_D value for P sorption to Fe(III) oxyhydroxides diminishes in the presence of dissolved silica, later workers suggested that IF P/Fe ratios suggest that Archaean phosphate concentrations may not have been limiting (Konhauser et al., 2007a; Planavsky et al., 2010b).

From a modelling perspective, Laakso and Schrag (2014) and Derry (2015) argued for low P levels in the Proterozoic through the establishment of an Fe trap – either through scavenging by Fe(III) particles or precipitation of ferrous phosphates, such as vivianite, $Fe_3(PO_4)_2$. Similarly, Reinhard et al. (2017) presented a large compilation of P data from siliciclastic sediments and identified a four-fold increase in P burial at the start of the Cryogenian (~720 Ma), which they linked to progressive oxygenation of the Earth and loss of the deep-sea Fe trap. Poulton (2017) countered that the record presented by Reinhard et al. (2017), and the large observed increase in P burial in the Neoproterozoic, may alternatively be explained by high P liberation and recycling from the sediment back into the water column. Accordingly, the extent to which P may have limited cyanobacterial productivity in the Proterozoic ocean remains unresolved.

Although P is likely to have been the ultimate limiting nutrient (e.g., Reinhard et al., 2017), limitation need not have been restricted to this element. With denitrification in the ocean interiors, N fixation in surface waters is needed to balance any P input to the oceans. Despite N isotopes having been used to argue for the antiquity of Mo-nitrogenase to a least 3.2 Ga (Stüeken et al., 2015a), prior to the Neoproterozoic rise in oxygen, the bulk marine Mo reservoir is likely to have been depressed owing to limited oxidative weathering, which in turn could have limited nitrogen fixation and overall primary productivity by oxygenic phototrophs in the Proterozoic (Anbar and Knoll, 2002; Scott et al., 2008; Reinhard et al., 2013). What role other biologically-essential nutrients played in ancient primary productivity is a current avenue of research (e.g., Robbins et al., 2013; Scott et al., 2013; Swanner et al., 2014). Overall, the possible suppression of cyanobacterial productivity by nutrient limitation in the Proterozoic is consistent with the current view of Earth's oxygenation history (e.g., Lyons et al., 2014) and with either limited or transient oxygen presence in the surface ocean (e.g., Hardisty et al., 2014, 2017).

(2) Instead of simply being starved, is it possible that other factors caused the marginalisation of cyanobacteria? One avenue worth considering is the analysis of nickel concentrations (expressed as molar Ni/Fe ratios) in IFs through time. The pattern shows a dramatic drop in Ni availability in the oceans around 2.7–2.6 Ga (Pecoits et al., 2009; Konhauser et al., 2009, 2015), although the timing of this dramatic decrease has been suggested to have occurred closer to the GOE, once the effects of cellular organic matter on Ni adsorption to ferrihydrite particles are considered (Eickhoff et al., 2014). The decrease in seawater Ni content after 2.7 Ga is consistent with a progressively cooling Archaean mantle, whereby the volume of ultramafic melts produced by partial mantle melting and the eruption of Ni-bearing ultramafic volcanic rocks (known as komatiites) decreased, and, subsequently, less Ni was dissolved into seawater. Since first identified, the decrease in Ni observed by Konhauser et al. (2009) has been suggested to be an artefact of limited IF sampling; however, after nearly doubling the number of IF analyses, the unidirectional decrease in Ni has remained stark and robust (Konhauser et al., 2015). This decrease in Ni availability could have had profound consequences for microorganisms that depended on it, specifically methane-producing bacteria or methanogens (Konhauser et al., 2009). These bacteria have a unique Ni requirement for their methane-producing enzymes, therefore, a limitation in this metal could have decreased their population in seawater. Compounding their plight, an increased supply of sulfate to the oceans after ca. 2.5 Ga (e.g., Cameron, 1983) would have fostered competition between the starving methanogens and the increasingly abundant sulfate-reducing bacteria, the latter having a competitive edge in terms of substrate utilisation (Lovley et al., 1982). It is thus possible that a Ni famine eventually led to a cascade of events that began with reduced methane production, the expansion of cyanobacteria into deep-water settings previously occupied by methanogens, and ultimately increased oxygenic photosynthesis that tipped the atmospheric redox balance in favour of oxygen, leading to the GOE. At the heart of this model is the simple idea that a decreased flux of methane led to greater oxygen concentrations in the atmosphere even if the marine O_2 flux to the atmosphere remained constant (Zahnle et al., 2006).

Is there any other evidence in the rock record to support a change in biological dynamics between methanogens and cyanobacteria? The answer may come from Neoarchaean shallow and deep-water sediments from the Hamersley Province that record 150 m.y. of Archaean history. As discussed above, Eigenbrode and Freeman (2006) observed highly negative $\delta^{13}C$ values in the organic carbon fraction, a feature of the Neoarchaean that has been known for some time, most likely representing microbial habitats influenced by the assimilation of methane, i.e., methanotrophy (e.g., Hayes, 1983). Intriguingly, there is a 10‰ increase in $\delta^{13}C$ values in kerogen in the post-2.7 Ga shallow-water facies relative to the deep-water settings, suggesting that the shallow waters became oxygenated (or oxidant-rich) as cyanobacteria became more abundant. At the same time, the deep waters remained a viable environment for the methanogens and methanotrophs. As populations of sulfate-reducing bacteria in the oceans increased, owing to the rise of atmospheric oxygen and concomitantly higher seawater sulfate concentrations, such bacteria would have continued to marginalise the methanogens and, indirectly, restrict the latter to even greater depths in the oceans, limiting their distribution to bottom sediments. Restricting methane production largely to the sediment pile would greatly increase the chances of anaerobic methane oxidation by either sulfate or solid-phase ferric iron, further reducing the methane flux to the atmosphere (Konhauser et al., 2005; Catling et al., 2007).

It is also possible that prior to the GOE cyanobacterial activity was depressed by high Fe(II) concentrations in surface waters. Swanner et al. (2015) recently discussed the implications of Fe toxicity to cyanobacteria in the range of 10s to 100 s of μM range of Fe(II). They suggested that elevated Fe(II) concentrations could have provided an external environmental stress on cyanobacterial populations, leading to increased production of intracellular reactive oxygen species, and attenuated growth rates and oxygen production. The potential for Fe(II) toxicity represents a previously unrecognised environmental limitation of planktonic cyanobacteria, and could conceivably have been important given estimates for marine Fe(II) concentrations from the low μM to mM range (e.g., Holland, 1984; Czaja et al., 2012; Tosca et al., 2016). As explored above, photoferrotrophs are likely to drive quantitative Fe(II) oxidation in an upwelling water mass in some, but not all, marine environments.

(3) It was hypothesised decades ago that the abundance of reduced solutes in the oceans could have served as a buffer to the increasing amounts of O_2 produced (e.g., Cloud, 1973). For instance, the oceans were rich in dissolved Fe(II), as testified by the global deposition of IFs between 2.60 and 2.45 Ga. Yet, as pointed out by Towe (1994, 1996), it is unlikely that ferrous iron buffering alone could balance a moderate oxygen flux because for every 1 mol of O_2 that reacts with ferrous iron in solution, 4 mol of Fe^{2+} are consumed [see reactions 7–8].

$$H_2O + CO_2 \rightarrow CH_2O + O_2 \quad (7)$$

$$4Fe^{2+} + O_2 + 10H_2O \rightarrow 4Fe(OH)_3 + 8H^+ \quad (8)$$

Other workers have proposed that the additional buffering capacity was provided by reduced volcanic and metamorphic gases (e.g., Kump et al., 2001). However, for these sinks to be larger in the Archaean than the Proterozoic, volcanic and metamorphic gases must have been more reducing unless the O_2 production flux was smaller. Kump and Barley (2007) proposed that in the Archaean volcanism was predominantly restricted to submarine settings and that volatiles released during submarine volcanism were more reducing than in subaerial settings (as they are today) because the former contain more CO, CH_4, and H_2S. Following the Archaean–Proterozoic transition, subaerial volcanism appears to have become more pervasive due to stabilisation of the continents. A shift from predominantly submarine to subaerial volcanism, releasing more oxidising volatiles such as H_2O, CO_2, and SO_2, would have reduced the overall sink for oxygen and led to the rise of atmospheric oxygen. Along similar lines, Gaillard et al. (2011) proposed that a decrease in the average pressure of volcanic degassing changed the oxidation state of sulfur in volcanic gases from predominantly H_2S to SO_2. Interestingly, the increased degassing of SO_2 over H_2S into the atmosphere was used by those same authors to not only explain the proliferation of S-MIF recorded in marine sediments between 2.7 and 2.5 Ga, but also that the production of SO_2 in the gas is accompanied by the formation and release of H_2 [reaction 9], which then escaped the atmosphere and aided in oxygenation of the planet (Catling et al., 2001).

$$H_2S + 2H_2O \rightarrow SO_2 + 3H_2 \quad (9)$$

(4) Another factor might have been the limited emergence of continental land masses. Signs of oxidative weathering likely reflect the ancient presence of cyanobacteria, which are rarely considered with respect to having formed terrestrial mats versus existence as marine phytoplankton. In this regard, Lalonde and Konhauser (2015) hypothesised that localised O_2 production within the confines of ancient biological communities on land could have generated sufficient oxidising power to mobilise trace metals and SO_4^{2-} from sulfide-bearing minerals in underlying substrata, without affecting the redox balance of the ocean-atmosphere system prior to the GOE. Under such a scenario, oxygen produced by the benthic microbial community would be consumed proximal to the mat, much as is observed in some modern mat systems (e.g., Gingras et al., 2011; Sumner et al., 2015).

New evidence that the early Archaean continents were greater in size and that a larger proportion was emergent than previously thought, highlights the potential importance of consumption of O_2 through oxidative weathering of the continents and suppression of atmospheric O_2 until the GOE (Satkoski et al., 2016, 2017). It has been recognised for some time that the volume of continental crust was substantial in the early Archaean (see review by Hawkesworth et al., 2010), but to date it has been unclear how continental freeboard controlled the amount of emergent continental landmasses. Continental freeboard depends more on mantle temperature, crustal composition, and continental hypsometry (also temperature-dependent) than on the growth of continental crust. Recent models suggest that continental landmasses did not reach modern level of emergence in the Archaean (Korenaga et al., 2017). Limited emergent continental crust would not only have severely limited the availability of continental crustal sources for weathering, but it would have compounded nutrient limitation for elements such as Mo supplied dominantly by oxidative weathering of crustal materials (see above discussion). Moreover, the amount of continental freeboard directly affects the relative proportions of submarine versus subaerial volcanism and thereby the reducing equivalents of volcanic gases, in the Kump and Barley (2007) model discussed above. Such conclusions, however, conflict with the growing evidence for elevated $^{87}Sr/^{86}Sr$ ratios in the early Archaean oceans that point to significant exposure of evolved continental crust at that time (Satkoski et al., 2016, 2017).

Irrespective of the causes for the delay in the rise of atmospheric O_2, by 2.5 Ga we see evidence for oxygen accumulation in the atmosphere from the Mt. McRae Shale in Western Australia, recording transient oxidised conditions now widely known as the 'whiff' of oxygen (Anbar et al., 2007). The whiff is recorded by spikes in Mo and Re concentrations, elevated nitrogen isotope values, and iron speciation data (Anbar et al., 2007; Reinhard et al., 2009; Garvin et al., 2009); based on Re-Os isotope analyses, these data can be confidently considered primary signals (Kendall et al., 2015). The shales lie near the middle of the 2.5-km-thick Hamersley Group (dated between 2.63 and 2.45 Ga), and directly underlie (in ascending order) the Brockman Iron Formation, Weeli Wolli Formation, Woongarra Volcanics, and Boolgeeda Iron Formation. Scott et al. (2011) have subsequently shown that euxinic conditions could develop under an Archaean anoxic atmosphere, and alternatives to the 'whiff' model have been proposed.

A recent compilation of the Cr contents in IFs has also contributed to our understanding of the GOE. For instance, a moderate enrichment in Cr (as expressed by the molar Cr/Ti ratio) beginning at 2.45 Ga in the Weeli Wolli Formation, as well as the similarly aged Cauê Iron Formation in Brazil, was followed by a spike in Cr enrichment in oolitic and pisolitic ironstone associated with the ca. 2.32 Ga Timeball Hill Formation (Konhauser et al., 2011). Cr enrichment in the face of muted Cr isotope fractionation at this time (Planavsky et al., 2014b) points to a supply mechanism that involved predominately the reduced Cr(III) form (Konhauser et al., 2011). Given the insolubility of Cr(III) minerals, mobilisation and incorporation of Cr into IF indicates enhanced chemical weathering at that time, most likely associated with the emergence of aerobic oxidation of continental pyrite.

Pyrite oxidation generates significant acidity [reaction 10]:

$$FeS_2 + 14Fe^{3+} + 8H_2O \rightarrow 15Fe^{2+} + 2SO_4^{2-} + 16H^+ \quad (10)$$

Such an acid-generated attack would have enhanced in-situ dissolution of Cr-bearing crustal minerals (including soils) that previously retained Cr under anoxic, but pH-neutral conditions, leading to increased continental Cr(III) supply to the oceans. Accordingly, it has been suggested that the Cr enrichment beginning at ca. 2.45 Ga reflects Earth's first acidic continental rock drainage, whereby acidity was

generated with rising O_2 at unprecedented scales via the oxidation of a previously untapped terrestrial pyrite reservoir. This process continued perhaps for 150–200 m.y. – the crustal half-life (Garrels and Mackenzie, 1972) - until the volume of easily oxidisable pyrite in the weathered crust was diminished (Konhauser et al., 2011; Bekker and Holland, 2012). Interestingly, not all IFs in this time window display elevated Cr enrichments (e.g., Dales Gorge and Joffre members of the Brockman Iron Formation). Considering the low solubility of Cr(III) at marine pH levels, the rapid reduction of Cr(VI) by aqueous Fe(II), and near-instantaneous co-precipitation of Cr(III) with Fe(III)-oxyhydroxide (e.g., Fendorf, 1995), dissolved Cr dispersal would be limited upon delivery to the oceans. In this regard, proximity of the depositional site to shore played a strong role in determining which IF would record a continental Cr input. Indeed, IFs having some of the highest Cr values, such as the Cauê and Timeball Hill formations, show evidence of sediment reworking and grade into GIF, indicative of shallow-water deposition (Eriksson, 1973; Spier et al., 2007). The oolitic and pisolitic Timeball Hill Formation records the highest degree of Cr enrichment among Palaeoproterozoic IF (Konhauser et al., 2011), which is not surprising considering its shallow-water depositional environment (pro-deltaic to offshore).

Evidence for increased oxidative weathering of the continents is also supported by a recent compilation of Cu isotopes in Precambrian marine sediments. Although the Cu concentration record presented by Chi Fru et al. (2016) for IFs and shales is relatively constant in terms of abundance – reminiscent of the Zn record raising the possibility of stabilisation of these trace metals by organic ligand complexation (see Robbins et al., 2013; Scott et al., 2013) – there is a clear trend in the stable isotopes values of Cu. Following the GOE, Cu isotopes in black shales become progressively heavier. This trend has been attributed to secular changes in seawater composition, due to the combined effect of waning IF deposition, which prior to the GOE would have preferentially removed ^{65}Cu with Fe(III)-oxyhydroxides, and increased oxidative supply of ^{65}Cu derived from continental weathering due to preferential leaching of the heavier Cu isotope. This ^{65}Cu, in turn, would have become incorporated into planktonic biomass that scavenged Cu from seawater.

The ability of cyanobacteria in the ocean's photic zones to remotely facilitate their own nutrient supply via O_2-enhanced chemical weathering may represent an unrecognised positive biological feedback (Konhauser et al., 2011). Thus the ca. 2.22–2.10 Ga Lomagundi carbon isotope excursion may, together with the Cr enrichment and Cu isotope changes in early Palaeoproterozoic sediments, be a manifestation of acid-driven dissolution and the first sedimentary cycle of oxidative weathering (Holland, 2002; Bekker and Holland, 2012).

Although multiple palaeoredox indicators point to a dramatic increase in surface oxygenation during the GOE, and in particular during its later part in association with the Lomagundi carbon isotope excursion (e.g., Bekker and Holland, 2012), we know surprisingly little regarding how high atmospheric and ocean oxygen contents rose. For instance, paleosol data from that time suggests that atmospheric oxygen might have risen to levels of 0.03 atm, and perhaps even as high as 0.1 atm Bekker and Holland (2012) (Fig. 10). The emerging picture from black shales indicates that Precambrian seawater reservoirs of redox-sensitive elements were nowhere close to those of the Phanerozoic (e.g., Scott et al., 2008; Partin et al., 2013b; Reinhard et al., 2013). Furthermore, Se isotope records of black shales suggest that while shallow-marine settings were suboxic and maintained enough oxygen for complex life to evolve, deep oceans remained at a low oxygenation state during the Lomagundi carbon isotope excursion, with euxinic conditions developed in intracratonic basins and on continental margins where nutrients were upwelled and high biological productivity was established (Kipp et al., 2017). It is unclear why IFs, especially GIFs that are consistent with shallow-water depositional environments, are not more abundant during > 100 m.y. of the Lomagundi carbon isotope excursion.

Following the end of the Lomagundi carbon isotope excursion, multiple redox indicators point to the collapse of seawater sulfate and atmospheric/oceanic oxygenation (e.g., Planavsky et al., 2012; Scott et al., 2008, 2014; Bekker and Holland, 2012; Partin et al., 2013a,b). In the case of oxygen, estimates range from values as high as 40% PAL to account for persistent anoxia in the oceans (Canfield, 2005) to values as low as 0.1% PAL based on Cr isotopes in various Proterozoic strata (Planavsky et al., 2014b) (Fig. 10). Consistent with these observations, IFs resurface, reaching their peak at ca. 1.88 Ga. At this time, shallow-marine GIFs were deposited above wave-base on several cratons (e.g., Rasmussen et al., 2012; Bekker et al., 2014) indicating a large flux of Fe (II) and Mn(II) from submarine-hydrothermal vents in association with an extensive LIP event. Deep oceans must have returned for a protracted period to the Archaean ferruginous (anoxic) state for the last time in Earth history, yet sedimentologically these ca. 1.88 Ga GIFs do not have equivalents in the Archaean. Although details remain unclear, it is certain that interplay of the strength of the hydrothermal flux linked to magmatic activity, ocean redox state, and palaeogeography (e.g., configuration of basins) led to this unprecedented rate of IF deposition for post-GOE time (Bekker et al., 2010, 2014). The extent and volume of these GIFs point to a rather peculiar state of the Earth System characterised by fully Fe-charged deep oceans like in the Archaean, and oxygenated nearshore conditions like in the Phanerozoic.

It is generally assumed that atmospheric and ocean oxygen levels remained low until ca. 1.2 Ga (Kah et al., 2004) or even ca. 800 Ma (Thomson et al., 2015; Turner and Bekker, 2016; Planavsky et al., 2014b). Similarly, the deep oceans are universally thought to have remained in a low-oxygen state, although debate continues on the exact level of deep-ocean oxygen concentrations with correspondingly anoxic (= ferruginous) and suboxic designations debated (Planavsky et al., 2011; Slack et al., 2007, 2009). Puzzlingly, economic-grade IFs are rather rare for this billion-year-long interval. However, a growing worldwide database for IFs and much more precise ages point to a dynamic redox state of the deep-oceans with IFs speaking to the water column's episodic anoxic (= ferruginous) state; for the rest of the time low, but substantial deep-ocean oxygen levels restricted Fe(II) transport in solution from hydrothermal vents. Similarly, Mn deposits are uncommon during this time period. This low-oxygen redox state in the deep oceans formed a prelude to Snowball glaciations, the rise of atmospheric and oceanic oxygen, and the emergence of complex life; the only return of massive IFs was in association with the Sturtian glaciation (e.g., Klein and Beukes, 1993; Hoffman et al., 1998). The Phanerozoic is a logical continuation of this trend during which higher atmospheric oxygen and a more intense biological pump restricted ironstones to relatively short time periods when the emplacement of LIPs resulted in greenhouse conditions, sea level rise, and extensive anoxic conditions in ocean basins.

5. Concluding remarks

Iron formations are a defining part of the Neoarchaean to Palaeoproterozoic marine sedimentary record. These deposits have been studied extensively, given their importance as ore bodies, for over a century. However, in the past decade alone there have been major advances in our understanding of their genesis. Some of these advances have come from revisiting the role that microbial metabolic reactions likely played in their deposition and diagenesis, in phase with equally rapid progress in our general understanding of microbial Fe cycling. Also, as expected, other advances have come from the application of novel isotope systems (e.g., Fe, Cr, U, Mo, Cu isotopes), as well as expansion of in situ isotopic analysis, which allows correlations to mineral paragenesis. With these new findings, there have been shifts from the 'textbook view' of IF genesis established during the pioneering work done in the 1970s and 1980s. Foremost, in contrast to the entrenched view, it is now generally accepted that microbial (i.e., enzymatic) Fe(II) oxidation was likely a key process in the deposition of many IFs. In

addition, evidence for extensive microbial Fe(III) reduction (e.g., DIR), on a basin-wide scale, as well as locally in the sediment, seems compelling. It is also clear that the deposition of IF was unlikely to have represented background marine sedimentation. Instead, a strong hydrothermal flux of iron, coupled with a low epiclastic input, was often the key factor that yielded IF rather than more typical marine sediments. Similarly, a complex set of factors – including the evolution of submarine-hydrothermal systems – is behind the secular distribution, rather than simply the deep marine redox evolution (i.e., ocean oxygenation) as was often imagined by early workers.

Our understanding of IF genesis has certainly moved forward at a rapid pace, as our use of these distinctive chemical sediments as palaeooceanographic archives has surged in recent years. One of the most exciting advances is an increased understanding of the co-evolution of Earth surface processes with microbial metabolism during the Archaean-Proterozoic transition. For example, the IF record has helped shape our view on the evolution of aerobic metabolisms tied to earlier expansion of cyanobacteria throughout the surface oceans during the Archaean. The emergence of an aerobic biosphere was likely brought on by an oxidative component to nutrient cycling and chemical weathering reactions, potentially altering nutrient fluxes to the oceans. Identification of widespread DIR, a deeply rooted metabolism in both bacteria and archaea, has also allowed us to understand the diversity of microbial ecology in the Archaean. Evidence for these processes is found in trace element and isotopic signatures contained within these Fe-rich chemical deposits as they continue to be the subject of intense study.

Acknowledgments

KOK, CAP and AB would like to thank the Natural Sciences and Engineering Research Council of Canada (NSERC) for its financial support (RGPIN-165831 to KOK; RGPIN-00062 to CAP; RGPIN-316500 to AB). LJR gratefully acknowledges the support of a Vanier Canada Graduate Scholarship. CMJ, DSH, NJP and TWL acknowledge support from the NASA Astrobiology Institute. SVL acknowledges support from the European Institute for Marine Studies (LabexMER, ANR-10-LABX-19). HT and PBHO thank ASSMANG Ltd. and SOUTH32 for providing research funding and access to drillcores, respectively. The authors thank Drs. Philip Fralick and John Slack for comments that greatly improved the manuscript, and Dr. André Strasser for his editorial efforts.

References

Abraham, K., Hofmann, A., Foley, S.F., Cardinal, D., Harris, C., Barth, M.G., André, L., 2011. Coupled silicon-oxygen isotope fractionation traces Archaean silicification. Earth Planet. Sci. Lett. 301, 222–230.
Ahn, J.H., Buseck, P.R., 1990. Hematite nanospheres of possible colloidal origin from a Precambrian banded iron formation. Science 250, 111–113.
Akhmedov, A.M., 1972a. Hematite oolites in sedimentary rocks of the Pechenga complex, materials on mineralogy of Kola Peninsula. Nauka 9, 135–137.
Akhmedov, A.M., 1972b. Iron-rich Metasedimentary Rock of Pechenga Complex and Their Genesis, Materials on Geology and Metallogeny of Kola Peninsula. Apatity. 4. pp. 125–131.
Alexander, B.W., Bau, M., Andersson, P., Dulski, P., 2008. Continentally-derived solutes in shallow Archean seawater: rare earth element and Nd isotope evidence in iron formation from the 2.9 Ga Pongola Supergroup, South Africa. Geochim. Cosmochim. Acta 72, 378–394.
Alexander, B.W., Bau, M., Andersson, P., 2009. Neodymium isotopes in Archean seawater and implications for the marine Nd cycle in Earth's early oceans. Earth Planet. Sci. Lett. 283, 144–155.
Alibert, C., 2016. Rare earth elements in Hamersley BIF minerals. Geochim. Cosmochim. Acta 184, 311–328.
Alibert, C., McCulloch, M.T., 1993. Rare element and neodymium isotopic compositions of the banded iron-formations and associated shales from Hamersley, Western Australia. Geochim. Cosmochim. Acta 57, 187–204.
Alibo, D.S., Nozaki, Y., 1999. Rare earth elements in seawater: particle association, shale-normalization, and Ce oxidation. Geochim. Cosmochim. Acta 63, 363–372.
Altermann, W., Nelson, D.R., 1998. Sedimentation rates, basin analysis and regional correlations of three Neoarchaean and Palaeoproterozoic sub-basins of the Kaapvaal craton as inferred from precise U-Pb zircon ages from volcaniclastic sediments. Sediment. Geol. 120, 225–256.
Altermann, W., Schopf, J.W., 1995. Microfossils from the Neoarchean Campbell Group, Griqualand West sequence of the Transvaal Supergroup, and their paleoenvironmental and evolutionary implications. Precambrian Res. 75, 65–90.
Amakawa, H., Nozakia, Y., Masuda, A., 1996. Precise determination of variations in the $^{138}Ce/^{142}Ce$ ratios of marine ferromanganese nodules. Chem. Geol. 131, 183–195.
Anbar, A.D., Holland, H.D., 1992. The photochemistry of manganese and the origin of banded iron formations. Geochim. Cosmochim. Acta 56, 2595–2603.
Anbar, A.D., Knoll, A.H., 2002. Proterozoic ocean chemistry and evolution: a bioinorganic bridge? Science 297, 1137–1142.
Anbar, A.D., Duan, Y., Lyons, T.W., Arnold, G.L., Kendall, B., Creaser, R.A., Kaufman, A.J., Gordon, G.W., Scott, C., Garvin, J., Buick, R., 2007. A whiff of oxygen before the Great Oxidation Event? Science 317, 1903–1906.
Anderson, T.F., Raiswell, R., 2004. Sources and mechanisms for the enrichment of highly reactive iron in euxinic Black Sea sediments. Am. J. Sci. 304, 203–233.
André, L., Cardinal, D., Alleman, L.Y., Moorbath, S., 2006. Silicon isotopes in ~3.8 Ga West Greenland rocks as clues to the Eoarchaean supracrustal Si cycle. Earth Planet. Sci. Lett. 245, 162–173.
Arndt, N.T., Nelson, D.R., Compston, W., Trendall, A.F., Thorne, A.M., 1991. The age of the Fortescue Group, Hamersley Basin, Western Australia, from iron microprobe zircon U-Pb results. Aust. J. Earth Sci. 38, 261–281.
Ayres, D., 1972. Genesis of iron-bearing minerals in banded iron formation mesobands in the Dales Gorge Member, Hamersley Group, Western Australia. Econ. Geol. 67, 1214–1233.
Bankole, A.M., El Albani, A., Meunier, A., Rouxel, O., Gauthier-Lafaye, F., Bekker, A., 2016. Origin of red beds in the Paleoproterozoic Franceville Basin, Gabon, and implications for sandstone-hosted uranium mineralization. Am. J. Sci. 316, 839–872.
Bao, H., Koch, P.L., 1999. Oxygen isotope fractionation in ferric oxide-water systems: low temperature synthesis. Geochim. Cosmochim. Acta 63, 599–613.
Barghoorn, E.S., Tyler, S.A., 1965. Microorganisms from Gunflint Chert. Science 147, 563–575.
Barley, M.E., Pickard, A.L., Sylvester, P.J., 1997. Emplacement of a large igneous province as a possible cause of banded iron formation 2.45 billion years ago. Nature 385, 55–58.
Barley, M.E., Bekker, A., Krapež, B., 2005. Late Archean to early Paleoproterozoic global tectonics, environmental change and the rise of atmospheric oxygen. Earth Planet. Sci. Lett. 238, 156–171.
Barns, S.M., Nierzwicki-Bauer, S.A., 1997. Microbial diversity in ocean, surface and subsurface environments. In: Banfield, J.F., Nealson, K.H. (Eds.), Geomicrobiology: Interactions Between Microbes and Minerals. Mineralogical Society of America, Washington, D.C., pp. 35–79.
Barrett, T.J., Wares, R.P., Fox, J.S., 1988. Two-stage hydrothermal formation of a Lower Proterozoic sediment-hosted massive sulfide deposit, northern Labrador Trough, Quebec. Can. Mineral. 26, 871–888.
Bau, M., 1991. Rare-earth element mobility during hydrothermal and metamorphic fluid-rock interaction and the significance of the oxidation state of europium. Chem. Geol. 93, 219–230.
Bau, M., 1996. Controls on the fractionation of isovalent trace elements in magmatic and aqueous systems: evidence from Y/Ho, Zr/Hf, and lanthanide tetrad effect. Contrib. Mineral. Petrol. 123, 323–333.
Bau, M., Dulski, P., 1996. Distribution of yttrium and rare-earth elements in the Penge and Kuruman iron-formations, Transvaal Supergroup, South Africa. Precambrian Res. 79, 37–55.
Bau, M., Koschinsky, A., 2009. Oxidative scavenging of cerium on hydrous Fe oxide: evidence from the distribution of rare earth elements and yttrium between Fe oxides and Mn oxides in hydrogenetic ferromanganese crusts. Geochem. J. 43, 37–47.
Bau, M., Möller, P., 1993. Rare-earth element systematics of the chemically precipitated component in early Precambrian iron formations and the evolution of the terrestrial atmosphere-hydrosphere-lithosphere system. Geochim. Cosmochim. Acta 57, 2239–2249.
Bau, M., Dulski, P., Möller, P., 1995. Yttrium and holmium in South Pacific seawater: vertical distribution and possible fractionation mechanisms. Chem. Erde 55, 1–15.
Bau, M., Hohndorf, A., Dulski, P., Beukes, N.J., 1997. Sources of rare-earth elements and iron in Paleoproterozoic iron-formations from the Transvaal Supergroup, South Africa: evidence from neodymium isotopes. J. Geol. 105, 121–129.
Bau, M., Romer, R.L., Lüders, V., Beukes, N.J., 1999. Pb, O, and C isotopes in silicified Mooidraai dolomite (Transvaal Supergroup, South Africa): implications for the composition of Paleoproterozoic seawater and 'dating' the increase in oxygen in the Precambrian atmosphere. Earth Planet. Sci. Lett. 174, 43–57.
Baur, M.E., Hayes, J.M., Studley, S.A., Walter, M.A., 1985. Millimeter-scale variations of stable isotope abundances in carbonates from banded iron-formations in the Hamersley Group of Western Australia. Econ. Geol. 80, 270–282.
Beal, E.J., House, C.H., Orphan, V.J., 2009. Manganese- and iron-dependent marine methane oxidation. Science 325, 184–187.
Beaumont, V., Robert, F., 1999. Nitrogen isotope ratios of kerogens in Precambrian cherts: a record of the evolution of atmosphere chemistry? Precambrian Res. 96, 63–82.
Becker, R.H., Clayton, R.N., 1976. Oxygen isotope study of a Precambrian banded iron-formation, Hamersley Range, Western Australia. Geochim. Cosmochim. Acta 40, 1153–1165.
Bekker, A., Holland, H.D., 2012. Oxygen overshoot and recovery during the early Paleoproterozoic. Earth Planet. Sci. Lett. 317, 295–304.
Bekker, A., Karhu, J.A., Eriksson, K.A., Kaufman, A.J., 2003. Chemostratigraphy of Paleoproterozoic carbonate successions of the Wyoming Craton: tectonic forcing of biogeochemical change? Precambrian Res. 120, 279–325.
Bekker, A., Holland, H.D., Wang, P.L., Rumble III, D., Stein, H.J., Hannah, J.L., Coetzee,

L.L., Beukes, N.J., 2004. Dating the rise of atmospheric oxygen. Nature 427, 117–120.
Bekker, A., Slack, J., Planavsky, N., Krapež, B., Hofmann, A., Konhauser, K.O., Rouxel, O.J., 2010. Iron formation: the sedimentary product of a complex interplay among mantle, tectonic, oceanic, and biospheric processes. Econ. Geol. 105, 467–508.
Bekker, A., Krapež, B., Slack, J., Planavsky, N., Hofmann, A., Konhauser, K.O., Rouxel, O.J., 2012. Iron formation: the sedimentary product of a complex interplay among mantle, tectonic, oceanic, and biospheric processes – a reply. Econ. Geol. 107, 379–380.
Bekker, A., Planavsky, N., Krapež, B., Rasmussen, B., Hofmann, A., Slack, J.F., Rouxel, O.J., Konhauser, K.O., 2014. Iron formations: their origins and implications for ancient seawater chemistry. In: Holland, H.D., Turekian, K.K. (Eds.), Treatise of Geochemistry, second ed. v. 9. Elsevier, pp. 561–628.
Berman, R.G., Sanborn-Barrie, M., Stern, R.A., Carson, C.J., 2005. Tectonometamorphism at ca. 2.35 and 1.85 Ga in the Rae Domain, western Churchill Province, Nunavut, Canada: Insight from structural, metamorphic, and in situ geochronologic analysis of the southwestern Committee Bay Belt. Can. Mineral. 43, 409–442.
Berner, R.A., 1964. An idealized model of dissolved sulfate distribution in recent sediments. Geochim. Cosmochim. Acta 28, 1497–1503.
Berner, R.A., 1984. Sedimentary pyrite formation: an update. Geochim. Cosmochim. Acta 48, 605–615.
Beukes, N.J., 1984. Sedimentology of the Kuruman and Griquatown iron-formations, Transvaal Supergroup, Griqualand West, South Africa. Precambrian Res. 24, 47–84.
Beukes, N.J., Cairncross, B., 1991. A lithostratigraphic-sedimentological reference profile for the Late Archaean Mozaan Group, Pongola Sequence: application to sequence stratigraphy and correlation with the Witwatersrand Supergroup. S. Afr. J. Geol. 94, 44–69.
Beukes, N.J., Gutzmer, J., 2008. Origin and paleoenvironmental significance of major iron formations at the Archean-Paleoproterozoic boundary. Rev. Econ. Geol. 15, 5–47.
Beukes, N.J., Klein, C., 1990. Geochemistry and sedimentology of a facies transition - from microbanded to granular iron-formation - in the early Proterozoic Transvaal Supergroup, South Africa. Precambrian Res. 47, 99–139.
Beukes, N.J., Klein, C., Kaufman, A.J., Hayes, J.M., 1990. Carbonate petrography, kerogen distribution, and carbon and oxygen isotope variations in an early Proterozoic transition from limestone to iron-formation deposition, Transvaal Supergroup, South Africa. Econ. Geol. 85, 663–690.
Bhattacharya, H., Chakraborty, I., Ghosh, K., 2007. Geochemistry of some banded iron-formations of the Archean supracrustals, Jharkhand-Orissa region, India. J. Earth Syst. Sci. 116, 245–259.
Bjerrum, C.J., Canfield, D.E., 2002. Ocean productivity before about 1.9 Ga ago limited by phosphorus adsorption onto iron oxides. Nature 417, 159–162.
Blättler, C.L., Kump, L.R., Fischer, W.W., Paris, G., Kasbohm, J.J., Higgins, J.A., 2016. Constraints on ocean carbonate chemistry and pCO_2 in the Archaean and Palaeoproterozoic. Nat. Geosci. 10, 41–45.
Bolhar, R., Kamber, B.S., Moorbath, S., Fedo, C.M., Whitehouse, M.J., 2004. Characterization of early Archaean chemical sediments by trace element signatures. Earth Planet. Sci. Lett. 222, 43–60.
Bosak, T., Greene, S.E., Newman, D.K., 2007. A possible role for anoxygenic photosynthetic microbes in the formation of ancient stromatolites. Geobiology 5, 119–126.
Boudreau, B., 1997. Diagenetic Models and Their Implementation: Modelling Transport and Reactions in Aquatic Sediments. Springer, New York, pp. 1–414.
Bowring, S.A., Schmus, W., Hoffman, P., 1984. U–Pb zircon ages from Athapuscow aulacogen, east arm of Great Slave Lake, NWT, Canada. Can. J. Earth Sci. 21, 1315–1324.
Braga, F.C.S., Rosiere, C.A., Queiroga, G.N., Rolim, V.K., Santos, J.O.S., McNaughton, N.J., 2015. The Statherian itabirite-bearing sequence from the Morro Escuro Ridge, Santa Maria de Itabira, Minas Gerais, Brazil. J. S. Am. Earth Sci. 58, 33–53.
Braterman, P.S., Cairns-Smith, A.G., Sloper, R.W., 1983. Photooxidation of hydrated Fe^{2+} - significance for banded iron formations. Nature 303, 163–164.
Braun, J.-J., Pagel, M., Muller, J.-P., Bilong, P., Michard, A., Guillet, B., 1990. Cerium anomalies in lateritic profiles. Geochim. Cosmochim. Acta 54, 781–795.
Bray, M.S., Wu, J., Reed, B.C., Kretz, C.B., Belli, K.M., Simister, R.L., Henny, C., Stewart, F.J., DiChristina, T.J., Brandes, J.A., Fowle, D.A., Crowe, S.A., Glass, J.B., 2017. Shifting microbial communities sustain multiyear iron reduction and methanogenesis in ferruginous sediment incubations. Geobiology 10. http://dx.doi.org/10.1111/gbi.12239.
Brocks, J.J., Love, G.D., Summons, R.E., Knoll, A.H., Logan, G.A., Bowden, S.A., 2005. Biomarker evidence for green and purple sulphur bacteria in a stratified Palaeoproterozoic sea. Nature 437, 866–870.
Bronner, G., Chauvel, J.J., 1979. Precambrian banded iron-formations of the Ijil Group (Kediat Ijil, Reguibat Shield, Mauritania). Econ. Geol. 74, 77–94.
Buick, R., 1992. The antiquity of oxygenic photosynthesis - evidence from stromatolites in sulfate-deficient Archean lakes. Science 255, 74–77.
Buick, R., 2008. When did oxygenic photosynthesis evolve? Philos. Trans. R. Soc. B 363, 2731–2743.
Busigny, V., Lebeau, O., Ader, M., Krapež, B., Bekker, A., 2013. Nitrogen cycle in the Late Archean ferruginous ocean. Chem. Geol. 362, 115–130.
Busigny, V., Planavsky, N.J., Jézéquel, D., Crowe, S., Louvat, P., Moureau, J., Viollier, E., Lyons, T.W., 2014. Iron isotopes in an Archean ocean analogue. Geochim. Cosmochim. Acta 133, 443–462.
Button, A., 1976. Transvaal and Hamersley basins—review of basin development and mineral deposits. Miner. Sci. Eng. 8, 262–293.
Byrne, R., Sholkovitz, E., 1996. Marine chemistry and geochemistry of the lanthanides. In: Gschneider Jr.K.A., Eyring, L. (Eds.), Handbook on the Physics and Chemistry of the Rare Earths. Elsevier, Amsterdam, pp. 497–593.
Cairns-Smith, A.G., 1978. Precambrian solution photochemistry, inverse segregation, and banded iron formations. Nature 276, 807–808.
Cameron, E.M., 1983. Evidence from early Proterozoic anhydrite for sulfur isotopic partitioning in Precambrian oceans. Nature 304, 54–56.
Canfield, D.E., 1998. A new model for Proterozoic ocean chemistry. Nature 396, 450–453.
Canfield, D.E., 2005. The early history of atmospheric oxygen: homage to Robert M Garrels. Annu. Rev. Earth Planet. Sci. 33, 1–36.
Canfield, D.E., 2006. Models of oxic respiration, denitrification and sulfate reduction in zones of coastal upwelling. Geochim. Cosmochim. Acta 70, 5753–5765.
Canfield, D.E., Ngombi-Pemba, L., Hammarlund, E.U., Bengston, S., Chaussidon, M., Gautheir-Lafaye, F., Meunier, A., Riboulleau, A., Rollion-Bard, C., Rouxel, O., Asael, D., Pierson-Wickmann, A.C., El Albani, A., 2013. Oxygen dynamics in the aftermath of the Great Oxidation of Earth's atmosphere. Proc. Natl. Acad. Sci. U. S. A. 110, 16736–16741.
Cannon, W.F., LaBerge, G.L., Klasner, J.S., Schulz, K.J., 2008. The Gogebic Iron Range - a sample of the northern margin of the Penokean fold and thrust belt. In: U.S. Geological Survey Professional Paper 1730, pp. 1–44.
Cannon, W.F., Schulz, K.J., Horton Jr., J.W., Kring, D.A., 2010. The Sudbury impact layer in the Paleoproterozoic iron ranges of northern Michigan, USA. Geol. Soc. Am. Bull. 122, 50–75.
Carazzo, G., Jellinek, A.M., Turchyn, A.V., 2013. The remarkable longevity of submarine plumes: implications for the hydrothermal input of iron to the deep-ocean. Earth Planet. Sci. Lett. 382, 66–76.
Carrigan, W.J., Cameron, E.M., 1991. Petrological and stable isotope studies of carbonate and sulfide minerals from the Gunflint Formation, Ontario: evidence for the origin of early Proterozoic iron-formation. Precambrian Res. 52, 347–380.
Catling, D., Zahnle, K., McKay, C., 2001. Biogenic methane, hydrogen escape, and the irreversible oxidation of early Earth. Science 293, 839–843.
Catling, D., Claire, M., Zahnle, K., 2007. Anaerobic methanotrophy and the rise of atmospheric oxygen. Philos. Trans. R. Soc. A Math. Phys. Eng. Sci. 365, 1867.
Chakrabarti, R., Knoll, A.H., Jacobsen, S.B., Fischer, W.W., 2012. Si isotope variability in Proterozoic cherts. Geochim. Cosmochim. Acta 91, 187–201.
Chan, C.S., Emerson, D., Luther, G.W., 2016. The role of microaerophilic Fe-oxidizing micro-organisms in producing banded iron formations. Geobiology 14, 509–528.
Chandler, F.W., 1980. Proterozoic redbed sequences of Canada. In: Canadian Geological Survey Bulletin. 311. pp. 1–53.
Chandler, F.W., 1984. Metallogenesis of an early Proterozoic foreland sequence, eastern Hudson Bay, Canada. J. Geol. Soc. 141, 299–313.
Cheney, E.S., 1996. Sequence stratigraphy and plate tectonic significance of the Transvaal succession of southern Africa and its equivalent in Western Australia. Precambrian Res. 79, 3–24.
Chi Fru, E., Ivarsson, M., Kilias, S.P., Bengtson, S., Belivanova, V., Marone, F., Fortin, D., Broman, C., Stampanoni, M., 2013. Fossilized iron bacteria reveal a pathway to the biological origin of banded iron formation. Nat. Commun. 4, 2050.
Chi Fru, E., Rodríguez, N.P., Partin, C.A., Lalonde, S.V., Andersson, P.S., Weiss, D.J., El Albani, A., Rodushkin, I., Konhauser, K.O., 2016. Cu isotopes in marine black shales record the Great Oxidation Event. Proc. Natl. Acad. Sci. U. S. A. 113, 4941–4946.
Chou, I.M., Eugster, H.P., 1977. Solubility of magnetite in supercritical chloride solutions. Am. J. Sci. 277, 1296–1314.
Cloud, P.E., 1965. Significance of Gunflint (Precambrian) microflora. Science 148, 27–35.
Cloud, P., 1973. Paleoecological significance of banded iron-formation. Econ. Geol. 68, 1135–1143.
Coffin, M.F., Eldholm, O., 1994. Large igneous provinces: crustal structure, dimensions, and external consequences. Rev. Geophys. 32, 1–36.
Condie, K.C., 1993. Chemical composition and evolution of the upper continental crust: contrasting results from surface samples and shales. Chem. Geol. 104, 1–37.
Condie, K.C., Des Marais, D.J., Abbott, D., 2001. Precambrian superplumes and supercontinents: a record in black shales, carbon isotopes and paleoclimates? Precambrian Res. 106, 239–260.
Corliss, J.B., Lyle, M., Dymond, J., Crane, K., 1978. Chemistry of hydrothermal mounds near Galapagos Rift. Earth Planet. Sci. Lett. 40, 12–24.
Cornell, D.H., Schütte, S.S., 1995. A volcanic-exhalative origin for the world's largest (Kalahari) manganese field. Mineral. Deposita 30, 146–151.
Cornell, D., Schütte, S., Eglington, B., 1996. The Ongeluk basaltic andesite formation in Griqualand West, South Africa: submarine alteration in a 2222 Ma Proterozoic sea. Precambrian Res. 79, 101–123.
Craddock, P.R., Dauphas, N., 2011. Iron and carbon isotope evidence for microbial iron respiration throughout the Archean. Earth Planet. Sci. Lett. 303, 121–132.
Crowe, S.A., Jones, C., Katsev, S., Magen, C., O'Neill, A.H., Sturm, A., Canfield, D.E., Haffner, G.D., Mucci, A., Sundby, B., Fowle, D.A., 2008. Photoferrotrophs thrive in an Archean ocean analogue. Proc. Natl. Acad. Sci. U. S. A. 105, 15938–15943.
Crowe, S.A., Katsev, S., Leslie, K., Sturm, A., Magen, C., Nomosatryo, S., Pack, M.A., Kessler, J.D., Reeburgh, W.S., Roberts, J.A., González, L., Douglas Haffner, G., Mucci, A., Sundby, B., Fowle, D.A., 2011. The methane cycle in ferruginous Lake Matano. Geobiology 9, 61–78.
Crowe, S.A., Døssing, L.N., Beukes, N.J., Bau, M., Kruger, S.J., Frei, R., Canfield, D.E., 2013. Atmospheric oxygenation three billion years ago. Nature 501, 535–538.
Czaja, A.D., Johnson, C.M., Roden, E.E., Beard, B.L., Voegelin, A.R., Nägler, T.F., Beukes, N.J., Wille, M., 2012. Evidence for free oxygen in the Neoarchean ocean based on coupled iron–molybdenum isotope fractionation. Geochim. Cosmochim. Acta 86, 118–137.
Czaja, A.D., Johnson, C.M., Beard, B.L., Roden, E.E., Li, W., Moorbath, S., 2013. Biological Fe oxidation controlled deposition of banded iron formation in the ca. 3370 Ma Isua Supracrustal Belt (West Greenland). Earth Planet. Sci. Lett. 363, 192–203.
Dai, Y.-D., Song, H.-M., Shen, J.-Y., 2004. Fossil bacteria in Xuanlong iron ore deposits of Hebei Province. Sci. China Ser. D Earth Sci. 47, 347–356.
Dalton de Souza, J., Kosin, M., Melo, R.C., Oliveira, E.P., Carvalho, M.J., Leite, C.M.,

2003. Guia de excursão - geologia do segmento norte do orógeno Itabuna-Salvador-Curaçá. Rev. Bras. Geosci. 33, 27–32.
Danielson, A., Möller, P., Dulski, P., 1992. The europium anomalies in banded iron formations and the thermal history of the oceanic crust. Chem. Geol. 97, 89–100.
Davis, W.J., Rainbird, R.H., Aspler, L.B., Chiarenzelli, J.R., 2005. Detrital zircon geochronology of the Paleoproterozoic Hurwitz and Kiyuk groups, western Churchill Province, Nunavut. In: Geological Survey of Canada Current Research-2005-F1, pp. 1–13.
de Baar, H.J.W., de Jong, J.T.M., 2001. Distributions, sources and sinks of iron in seawater. In: Turner, D., Hunter, K.A. (Eds.), The Biogeochemistry of Iron in Seawater. John Wiley & Sons, New York, pp. 123–253.
de Baar, H.J.W., Bacon, M.P., Brewer, P.G., 1985. Rare earth elements in the Pacific and Atlantic Oceans. Geochim. Cosmochim. Acta 49, 1943–1959.
Delstanche, S., Opfergelt, S., Cardinal, D., Elsass, F., André, L., Delvaux, B., 2009. Silicon isotopic fractionation during adsorption of aqueous monosilicic acid onto iron oxide. Geochim. Cosmochim. Acta 73, 923–934.
Delvigne, C., Cardinal, D., Hofmann, A., André, L., 2012. Stratigraphic changes of Ge/Si, REE + Y and silicon isotopes as insights into the deposition of a Mesoarchaean banded iron formation. Earth Planet. Sci. Lett. 355–356, 109–118.
Derry, L.A., 2015. Causes and consequences of mid-Proterozoic anoxia. Geophys. Res. Lett. 42, 8538–8546.
Derry, L.A., Jacobsen, S.B., 1988. The Nd and Sr isotopic evolution of Proterozoic seawater. Geophys. Res. Lett. 15, 397–400.
Derry, L.A., Jacobsen, S.B., 1990. The chemical evolution of Precambrian seawater: evidence from REEs in banded iron formations. Geochim. Cosmochim. Acta 54, 2965–2977.
Dhuime, B., Wuestefeld, A., Hawkesworth, C.J., 2015. Emergence of continental crust about 3 billion years ago. Nat. Geosci. 8, 552–555.
Ding, T., Gao, J., Tian, S., Fan, C., Zhao, Y., Wan, D., Zhou, J., 2017. The $\delta^{30}Si$ peak value discovered in middle Proterozoic chert and its implication for environmental variations in the ancient ocean. Sci Rep 7, 44000.
Dodd, M.S., Papineau, D., Grenne, T., Slack, J.F., Rittner, M., Pirajno, F., O'Neil, J., Little, C.T.S., 2017. Evidence for early life in Earth's oldest hydrothermal vent precipitates. Nature 543, 60–64.
Doelsch, E., Rose, J., Masion, A., Bottero, J.Y., Nahon, D., Bertsch, P.M., 2000. Speciation and crystal chemistry of iron(III) chloride hydrolyzed in the presence of SiO_4 ligands. 1. An Fe K-edge EXAFS study. Langmuir 16, 4726–4731.
Doelsch, E., Stone, W.E.E., Petit, S., Masion, A., Rose, J., Bottero, J.-Y., Nahon, D., 2001. Speciation and crystal chemistry of Fe(III) chloride hydrolyzed in the presence of SiO_4 ligands. 2. Characterization of SiFe aggregates by FTIR and ^{29}Si solid-state NMR. Langmuir 17, 1399–1405.
Doelsch, E., Masion, A., Rose, J., Stone, W.E.E., Bottero, J.Y., Bertsch, P.M., 2003. Chemistry and structure of colloids obtained by hydrolysis of Fe(III) in the presence of SiO_4 ligands. Colloids Surf. A Physicochem. Eng. Asp. 217, 121–128.
Dorland, H.C., 1999. Paleoproterozoic Laterites, Red Beds and Ironstones of the Pretoria Group With Reference to the History of Atmospheric Oxygen. Rand Afrikaans University, Johannesburg, South Africa, pp. 1–147.
Dymek, R., Klein, C., 1988. Chemistry, petrology and origin of banded iron-formation lithologies from the 3800 Ma Isua Supracrustal Belt, West Greenland. Precambrian Res. 39, 247–302.
Easton, R.M., 2005. The Grenvillian Tomiko quartzites of Ontario: Correlatives of the Baraboo quartzites of Wisconsin, the Mazatzal orogen of New Mexico, or unique? Implications for the tectonic architecture of Laurentia in the Great Lakes region. In: Institute on Lake Superior Geology, 51th Annual Meeting, Proceedings, Volume 51, Part 1 - Proceedings and Abstracts, pp. 15–16.
Egal, E., Thieblemont, D., Lahondere, D., Guerrot, C., Costea, C.A., Iliescu, D., Delor, C., Goujou, J.C., Lafon, J.M., Tegyey, M., Diaby, S., Kolie, P., 2002. Late Eburnean granitization and tectonics along the western and northwestern margin of the Archean Kenema-Man domain (Guinea, West African Craton). Precambrian Res. 117, 57–84.
Eickhoff, M., Obst, M., Schröder, C., Hitchcock, A.P., Tyliszczak, T., Martinez, R.E., Robbins, L.J., Konhauser, K.O., Kappler, A., 2014. Nickel partitioning in biogenic and abiogenic ferrihydrite: the influence of silica and implications for ancient environments. Geochim. Cosmochim. Acta 140, 65–79.
Eigenbrode, J.L., Freeman, K.H., 2006. Late Archean rise of aerobic microbial ecosystems. Proc. Natl. Acad. Sci. U. S. A. 103, 15759–15764.
Elderfield, H., Greaves, M.J., 1982. The rare earth elements in seawater. Nature 296, 214–219.
England, G.L., Rasmussen, B., Krapež, B., Groves, D.I., 2002. Paleoenvironmental significance of rounded pyrite in siliciclastic sequences of the Late Archean Witwatersrand Basin: oxygen-deficient atmosphere or hydrothermal alteration? Sedimentology 49, 1133–1156.
Eriksson, K.A., 1973. The Timeball Hill Formation: a fossil delta. J. Sediment. Res. 43, 1046–1053.
Eriksson, P.G., Engelbrecht, J.P., Res, M., Harmer, R.E., 1994a. The Bushy Bend lavas, a new volcanic member of the Pretoria Group, Transvaal Sequence. S. Afr. J. Geol. 97, 1–7.
Eriksson, P.G., Reczko, B.F.F., Merkle, R.K.W., Schreiber, U.M., Engelbrecht, J.P., Res, M., Snyman, C.P., 1994b. Early Proterozoic black shales of the Timeball Hill Formation, South Africa: volcanogenic and palaeoenvironmental influences. J. Afr. Earth Sci. 18, 325–337.
Ernst, R.E., Buchan, K.L., 2001. Large mafic magmatic events through time and links to mantle-plume heads. In: Ernst, R.E., Buchan, K.L. (Eds.), Mantle Plume: Their Identification Through Time. Geological Society of America Special Paper 352, pp. 483–575.
Etique, M., Jorand, F.P.A., Ruby, C., 2015. Magnetite as a precursor for green rust through the hydrogenotrophic activity of the iron-reducing bacteria Shewanella putrefaciens. Geobiology 14, 237–254.
Ettwig, K.F., Zhu, B., Speth, D., Keltjens, J.T., Jetten, M.S.M., Kartal, B., 2016. Archaea catalyze iron-dependent anaerobic oxidation of methane. Proc. Natl. Acad. Sci. U. S. A. 113, 12792–12796.
Eugster, H.P., Chou, I.M., 1973. The depositional environments of Precambrian banded iron-formations. Econ. Geol. 68, 1144–1168.
Ewers, W., Morris, R., 1981. Studies of the Dales Gorge Member of the Brockman Iron Formation, Western Australia. Econ. Geol. 76, 1929–1953.
Farquhar, J., Bao, H., Thiemens, M., 2000. Atmospheric influence of Earth's earliest sulfur cycle. Science 289, 756–758.
Farquhar, J., Zerkle, A.L., Bekker, A., 2011. Geological constraints on the origin of oxygenic photosynthesis. Photosynth. Res. 107, 11–36.
Farquhar, J., Zerkle, A.L., Bekker, A., 2014. Geological and geochemical constraints on Earth's early atmosphere. In: Holland, H.D., Turekian, K.K. (Eds.), Treatise of Geochemistry, second ed. v. 6. Elsevier, pp. 91–138.
Fendorf, S.E., 1995. Surface reactions of chromium in soils and waters. Geoderma 67, 55–71.
Fetter, A.H., Van Schmus, W.R., Santos, T.J.S., Neto, J.A.N., Henriarthaud, M., 2000. U-Pb and Sm-Nd geochronological constraints on the crustal evolution and basement architecture of Ceará state, NW Borborema Province, NE Brazil: implications for the existence of the Paleoproterozoic supercontinent “Atlantica”. Rev. Bras. Geosci. 30, 102–106.
Field, E.K., Kato, S., Findlay, A.J., MacDonald, D.J., Luther, G.W., Chan, C.S., 2016. Planktonic marine iron-oxidizers drive iron mineralization under low oxygen conditions. Geobiology 15, 499–508.
Findlay, J.M., Parrish, R.R., Birkett, T.C., Watanabe, D.H., 1995. U-Pb ages from the Nimish Formation and Montagnais glomeroporphyritic gabbro of the central new Québec orogen, Canada. Can. J. Earth Sci. 32, 1208–1220.
Fischer, W.W., Knoll, A.H., 2009. An iron shuttle for deepwater silica in Late Archean and early Paleoproterozoic iron formation. Geol. Soc. Am. Bull. 121, 222–235.
Fischer, W.W., Schröder, S., Lacassie, J.P., Beukes, N.J., Goldberg, T., Strauss, H., Horstmann, U.E., Schrag, D.P., Knoll, A.H., 2009. Isotopic constraints on the Late Archean carbon cycle from the Transvaal Supergroup along the western margin of the Kaapvaal Craton, South Africa. Precambrian Res. 169, 15–27.
Fitzsimmons, J.N., John, S.G., Marsay, C.M., Hoffman, C.L., Nicholas, S.L., Toner, B.M., German, C.R., Sherrell, R.M., 2017. Iron persistence in a distal hydrothermal plume supported by dissolved–particulate exchange. Nat. Geosci. 10, 195–201.
Fralick, P.W., Pufahl, P.K., 2006. Iron formation in Neoarchean deltaic successions and the microbially mediated deposition of transgressive systems tracts. J. Sediment. Res. 76, 1057–1066.
Fralick, P., Davis, D.W., Kissin, S.A., 2002. The age of the Gunflint Formation, Ontario, Canada: single zircon U-Pb age determinations from reworked volcanic ash. Can. J. Earth Sci. 39, 1085–1091.
Frei, R., Polat, A., 2007. Source heterogeneity for the major components of ~ 3.7 Ga banded iron formations (Isua Greenstone Belt, western Greenland): tracing the nature of interacting water masses in BIF formation. Earth Planet. Sci. Lett. 253, 266–281.
Frei, R., Dahl, P.S., Duke, E.F., Frei, K.M., Hansen, T.R., Frandsson, M.M., Jensen, L.A., 2008. Trace element and isotopic characterization of Neoarchean and Paleoproterozoic iron formations in the Black Hills (South Dakota, USA): assessment of chemical change during 2.9-1.9 Ga deposition bracketing the 2.4-2.2 Ga first rise of atmospheric oxygen. Precambrian Res. 162, 441–474.
Frei, R., Crowe, S.A., Bau, M., Polat, A., Fowle, D.A., Døssing, L.N., 2016. Oxidative elemental cycling under the low O_2 Eoarchean atmosphere. Sci Rep 6, 21058.
Frierdich, A.J., Beard, B.L., Scherer, M.M., Johnson, C.M., 2014. Determination of the Fe $(II)_{aq}$-magnetite equilibrium iron isotope fractionation factor using the three-isotope method and a multi-direction approach to equilibrium. Earth Planet. Sci. Lett. 391, 77–86.
Froelich, P.N., Klinkhammer, G.P., Bender, M.L., Luedtke, N.A., Heath, G.R., Cullen, D., Dauphin, P., Hammond, D., Hartman, B., Maynard, V., 1979. Early oxidation of organic matter in pelagic sediments of the eastern equatorial Atlantic: Suboxic diagenesis. Geochim. Cosmochim. Acta 43, 1075–1090.
Frost, C.D., von Blanckenburg, F., Schoenberg, R., Frost, B.R., Swapp, S.M., 2007. Preservation of Fe isotope heterogeneities during diagenesis and metamorphism of banded iron formation. Contrib. Mineral. Petrol. 153, 211–235.
Fryer, B., 1977a. Rare earth evidence in iron-formations for changing Precambrian oxidation states. Geochim. Cosmochim. Acta 41, 361–367.
Fryer, B., 1977b. Trace-element geochemistry of Sokoman Iron Formation. Can. J. Earth Sci. 14, 1598–1610.
Fryer, B.J., Fyfe, W.S., Kerrich, R., 1979. Archaean volcanogenic oceans. Chem. Geol. 24, 25–33.
Gaillard, F., Scaillet, B., Arndt, N.T., 2011. Atmospheric oxygenation caused by a change in volcanic degassing pressure. Nature 478, 229–233.
Garrels, R.M., Mackenzie, F.T., 1972. A quantitative model for the sedimentary rock cycle. Mar. Chem. 1, 27–41.
Garrels, R.M., Perry, E.A., Mackenzie, F.T., 1973. Genesis of Precambrian iron-formations and development of atmospheric oxygen. Econ. Geol. 68, 1173–1179.
Garvin, J., Buick, R., Anbar, A.D., Arnold, G.L., Kaufman, A.J., 2009. Isotopic evidence for an aerobic nitrogen cycle in the latest Archean. Science 323, 1045–1048.
Gauger, T., Konhauser, K.O., Kappler, A., 2015. Protection of phototrophic iron (II)-oxidizing bacteria from UV irradiation by biogenic iron (III) minerals: implications for early Archean banded iron formation. Geology 43, 1067–1070.
Gauger, T., Konhauser, K.O., Kappler, A., 2016. Protection of nitrate-reducing Fe(II)-oxidizing bacteria from UV radiation by biogenic Fe(III) minerals. Astrobiology 16, 301–310.
Geilert, S., Vroon, P.Z., van Bergen, M.J., 2014. Silicon isotopes and trace elements in

chert record early Archean basin evolution. Chem. Geol. 386, 133–142.
German, C.R., Seyfried Jr., W.E., 2014. Hydrothermal processes. In: Holland, H.D., Turekian, K.K. (Eds.), Treatise of Geochemistry, second ed. v. 8. Elsevier, pp. 191–233.
German, C.R., Von Damm, K.L., 2003. Hydrothermal processes. In: Holland, H.D., Turekian, K.K. (Eds.), Treatise of Geochemistry. v. 6. Elsevier, pp. 181–222.
German, C.R., Holliday, B.P., Elderfield, H., 1991. Redox cycling of rare earth elements in the suboxic zone of the Black Sea. Geochim. Cosmochim. Acta 55, 3553–3558.
German, C.R., Thurnherr, A.M., Knoery, J., Charlou, J.-L., Jean-Baptise, P., Edmonds, H.N., 2010. Heat, volume and chemical fluxes from submarine venting: a synthesis of results from the Rainbow hydrothermal field, 36°N MAR. Deep-Sea Res. I 57, 518–527.
Gingras, M.K., Hagadorn, J.W., Seilacher, A., Lalonde, S.V., Pecoits, E., Petrash, D., Konhauser, K.O., 2011. Possible evolution of mobile animals in association with microbial mats. Nat. Geosci. 4, 372–375.
Godfrey, L.V., Falkowski, P.G., 2009. The cycling and redox state of nitrogen in the Archaean ocean. Nat. Geosci. 2, 725–729.
Gole, M.J., Klein, C., 1981. Banded iron-formation through much of Precambrian time. J. Geol. 89, 169–183.
Golubic, S., Lee, S.J., 1999. Early cyanobacterial fossil record: preservation, palaeoenvironments and identification. Eur. J. Phycol. 34, 339–348.
Goode, A.D.T., Hall, W.D.M., Bunting, J.A., 1983. The Nabberu basin of Western Australia. In: Trendall, A.F., Morris, R.C. (Eds.), Iron-formation: Facts and Problems. Elsevier Science Publishers, Amsterdam, pp. 295–323.
Goodwin, A.M., 1962. Structure, stratigraphy, an origin of iron formations, Michipicoten area, Algoma District, Ontario, Canada. Geol. Soc. Am. Bull. 73, 561–586.
Gourcerol, B., Thurston, P.C., Kontak, D.J., Côté-Mantha, O., Biczok, J., 2016. Depositional setting of Algoma-type banded iron formation. Precambrian Res. 281, 47–79.
Graf, J.L., 1977. Rare earth elements as hydrothermal tracers during the formation of massive sulfide deposits in volcanic rocks. Econ. Geol. 72, 527–548.
Graf, J.L., 1978. Rare earth elements, iron formations and sea water. Geochim. Cosmochim. Acta 42, 1845–1850.
Gross, G.A., 1980. A classification of iron-formation based on depositional environments. Can. Mineral. 18, 215–222.
Gross, G., 1983. Tectonic systems and the deposition of iron-formation. Precambrian Res. 20, 171–187.
Grotzinger, J.P., Kasting, J.F., 1993. New constraints on Precambrian ocean composition. J. Geol. 101, 235–243.
Gruner, J.W., 1922. The origin of sedimentary iron-formations: the Biwabik Formation of the Mesabi Range. Econ. Geol. 22, 407–460.
Guan, N., Wang, Y., Sun, D., Xu, J., 2009. A simple one-pot synthesis of single-crystalline magnetite hollow spheres from a single iron precursor. Nanotechnology 20, 105603.
Gumsley, A.P., Chamberlain, K.R., Bleeker, W., Söderlund, U., de Kock, M.O., Larsson, E.R., Bekker, A., 2017. Timing and tempo of the Great Oxidation Event. Proc. Natl. Acad. Sci. U. S. A. 114, 1811–1816.
Guo, Q., Strauss, H., Kaufman, A.J., Schröder, S., Gutzmer, J., Wing, B., Baker, M.A., Bekker, A., Kim, S.-T., Farquhar, J., 2009. Reconstructing Earth's surface oxidation across the Archean-Proterozoic transition. Geology 37, 399–402.
Halama, M., Swanner, E.D., Konhauser, K.O., Kappler, A., 2016. Evaluation of siderite and magnetite formation in BIFs by pressure–temperature experiments of Fe(III) minerals and microbial biomass. Earth Planet. Sci. Lett. 450, 243–253.
Halevy, I., Bachan, A., 2017. The geologic history of seawater pH. Science 355, 1069–1071.
Halevy, I., Alesker, M., Schuster, E.M., Popovitz-Biro, R., Feldman, Y., 2017. A key role for green rust in the Precambrian oceans and the genesis of iron formations. Nat. Geosci. 10, 135–139.
Haley, B.A., Klinkhammer, G.P., McManus, J., 2004. Rare earth elements in pore waters of marine sediments. Geochim. Cosmochim. Acta 68, 1265–1279.
Hallstrom, S., Hoglund, L., Agren, J., 2011. Modelling of iron diffusion in the iron oxides magnetite and hematite with variable stoichiometry. Acta Mater. 59, 53–60.
Halverson, P., Poitrasson, F., Hoffman, P.F., Nédélec, A., Montel, J.M., Kirby, J., 2011. Fe isotope and trace element geochemistry of the Neoproterozoic syn-glacial Rapitan Iron Formation. Earth Planet. Sci. Lett. 309, 100–112.
Hamilton, M.A., Buchan, K.L., Ernst, R.E., Stott, G.M., 2009. Wide-spread and short-lived 1870 Ma mafic magmatism along the northern Superior Craton margin. In: EOS Transactions, American Geophysical Union, 2009 Joint Assembly, Toronto, Canada, (Abstract GA11A-01).
Hannah, J.L., Bekker, A., Stein, H.J., Markey, R.J., Holland, H.D., 2004. Primitive Os and 2316 Ma age for marine shale: implications for Paleoproterozoic glacial events and the rise of atmospheric oxygen. Earth Planet. Sci. Lett. 225, 43–52.
Hardisty, D.S., Lu, Z., Planavsky, N.J., Bekker, A., Philippot, P., Zhou, X., Lyons, T.W., 2014. An iodine record of Paleoproterozoic surface ocean oxygenation. Geology 42, 619–622.
Hardisty, D.S., Lu, Z., Bekker, A., Diamond, C.W., Gill, B.C., Jiang, G., Kah, L.C., Knoll, A.H., Loyd, S.J., Osburn, M.R., Planavsky, N.J., Wang, C., Zhou, X., Lyons, T.W., 2017. Perspectives on Proterozoic surface ocean redox from iodine contents in ancient and recent carbonate. Earth Planet. Sci. Lett. 463, 159–170.
Hartlaub, R.P., Heaman, L.M., Chacko, T., Ashton, K.E., 2007. Circa 2.3 Ga magmatism of the Arrowsmith Orogeny, Uranium City Region, Western Churchill Craton. Can. J. Earth Sci. 115, 181–195.
Hartman, H., 1984. The evolution of photosynthesis and microbial mats: a speculation on the banded iron formations. In: Cohen, Y., Castenholz, R.W., Halvorson, H.O. (Eds.), Microbial Mats: Stromatolites. Alan R. Liss, New York, pp. 449–453.
Haugaard, R., Frei, R., Stendald, H., Konhauser, K.O., 2013. Petrology and geochemistry of the ~2.9 Ga Itilliarsuk banded iron formation and associated supracrustal rocks, West Greenland: source characteristics and depositional environment. Precambrian Res. 229, 150–176.
Haugaard, R., Ootes, L., Creaser, R.A., Konhauser, K.O., 2016a. The nature of Mesoarchaean seawater and continental weathering in 2.85 Ga banded iron formation, Slave Craton, NW Canada. Geochim. Cosmochim. Acta 194, 34–56.
Haugaard, R., Pecoits, E., Lalonde, S., Rouxel, O., Konhauser, K.O., 2016b. The Joffre Banded Iron Formation, Hamersley Group, Western Australia: assessing the palaeoenvironment through detailed petrology and chemostratigraphy. Precambrian Res. 273, 12–37.
Haugaard, R., Ootes, L., Heaman, L.M., Hamilton, M.A., Shaulis, B.J., Konhauser, K.O., 2017a. Depositional timing of Neoarchean turbidites of the Slave Craton—recommended nomenclature and type localities. Can. J. Earth Sci. 54, 15–32.
Haugaard, R., Ootes, L., Creaser, R.A., Konhauser, K.O., 2017b. Neoarchaean banded iron formation within a 2620 Ma turbidite-dominated deep-water basin, Slave craton, NW Canada. Precambrian Res. 292, 130–151.
Hawkesworth, C.J., Dhuime, B., Pietranik, A.B., Cawood, P.A., Kemp, A.I.S., Storey, C.D., 2010. The generation and evolution of the continental crust. J. Geol. Soc. Lond. 167, 229–248.
Hayashi, T., Tanimizu, M., Tanaka, T., 2004. Origin of negative Ce anomalies in Barberton sedimentary rocks, deduced from La–Ce and Sm–Nd isotope systematics. Precambrian Res. 135, 345–357.
Hayes, J.M., 1983. Geochemical evidence bearing on the origin of aerobiosis, a speculative hypothesis. In: Schopf, J.W. (Ed.), Earth's Earliest Biosphere, Its Origins and Evolution. Princeton University Press, Princeton, pp. 291–301.
Heaman, L.M., 1997. Global mafic volcanism at 2.45 Ga: remnants of an ancient large igneous province? Geology 25, 299–302.
Heaman, L.M., Machado, N., Krogh, T.E., Weber, W., 1986. Precise U-Pb zircon ages for the Molson dyke swarm and the Fox River sill: constraints for Early Proterozoic crustal evolution in northeastern Manitoba, Canada. Contrib. Mineral. Petrol. 94, 82–89.
Heaman, L.M., Peck, D., Toope, K., 2009. Timing and geochemistry of 1.88 Ga Molson igneous events, Manitoba: insights into the formation of a craton-scale magmatic and metallogenic province. Precambrian Res. 172, 143–162.
Heck, P.R., Huberty, J.M., Kita, N.T., Ushikubo, T., Kozdon, R., Valley, J.W., 2011. SIMS analyses of silicon and oxygen isotope ratios for quartz from Archean and Paleoproterozoic banded iron formations. Geochim. Cosmochim. Acta 75, 5879–5891.
Heimann, A., Johnson, C.M., Beard, B.L., Valley, J.W., Roden, E.E., Spicuzza, M.J., Beukes, N.J., 2010. Fe, C, and O isotope compositions of banded iron formation carbonates demonstrate a major role for dissimilatory iron reduction in ~2.5 Ga marine environments. Earth Planet. Sci. Lett. 294, 8–18.
Heising, S., Richter, L., Ludwig, W., Schink, B., 1999. Chlorobium ferrooxidans sp. nov., a phototrophic green sulfur bacterium that oxidizes ferrous iron in co-culture with a "Geospirillum" sp. strain. Arch. Microbiol. 172, 116–124.
Heubeck, C., 2009. An early ecosystem of Archean tidal microbial mats (Moodies Group, South Africa, ca. 3.2 Ga). Geology 37, 931–934.
Higgins, J.A., Fischer, W.W., Schrag, D.P., 2009. Oxygenation of the ocean and sediments: consequences for the seafloor carbonate factory. Earth Planet. Sci. Lett. 284, 25–33.
Hoffman, P.F., 1987. Early Proterozoic foredeeps, foredeep magmatism, and Superior-type iron formations of the Canadian Shield. In: Kröner, A. (Ed.), Proterozoic Lithospheric Evolution. American Geophysical Union/Geological Society of America, Washington, DC; Boulder, CO, pp. 85–98.
Hoffman, P.F., Kaufman, A.J., Halverson, G.P., Schrag, D.P., 1998. A Neo-proterozoic snowball Earth. Science 281, 1342–1346.
Hoffman, P.F., Bowring, S.A., Buchwaldt, R., 2011. Birthdate for the Coronation paleocean: age of initial rifting in Wopmay orogen, Canada. Can. J. Earth Sci. 48, 281–293.
Hofmann, A., 2005. The geochemistry of sedimentary rocks from the Fig Tree Group, Barberton greenstone belt: implications for tectonic, hydrothermal and surface processes during mid-Archaean times. Precambrian Res. 143, 23–49.
Hofmann, A., Bekker, A., Rouxel, O.J., Rumble, D., Master, S., 2009. Multiple sulphur and iron isotope composition of detrital pyrite in Archaean sedimentary rocks: a new tool for provenance analysis. Earth Planet. Sci. Lett. 286, 436–445.
Holland, H.D., 1973. Oceans - possible source of iron in iron-formations. Econ. Geol. 68, 1169–1172.
Holland, H.D., 1978. The Chemistry of the Atmosphere and Oceans. Wiley, New York, pp. 1–369.
Holland, H.D., 1984. The Chemical Evolution of the Atmosphere and Oceans. Princeton University Press, Princeton, NJ, pp. 1–598.
Holland, H.D., 2002. Volcanic gases, black smokers, and the Great Oxidation Event. Geochim. Cosmochim. Acta 66, 3811–3826.
Holm, N.G., 1989. The $^{13}C/^{12}C$ ratios of siderite and organic matter of a modern metalliferous hydrothermal sediment and their implications for banded iron formations. Chem. Geol. 77, 41–45.
Homann, M., Heubeck, C., Airo, A., Tice, M.M., 2015. Morphological adaptations of 3.22 Ga-old tufted microbial mats to Archean coastal habitats (Moodies Group, Barberton Greenstone Belt, South Africa). Precambrian Res. 266, 47–64.
Horner, T.J., Williams, H.M., Hein, J.R., Saito, M.A., Burton, K.W., Halliday, A.N., Nielsen, S.G., 2015. Persistence of deeply sourced iron in the Pacific Ocean. Proc. Natl. Acad. Sci. U. S. A. 112, 1292–1297.
Horstmann, U.E., Hälbich, I.W., 1995. Chemical composition of banded iron-formations of the Griqualand West Sequence, Northern Cape Province, South Africa, in comparison with other Precambrian iron formations. Precambrian Res. 72, 109–145.
Hotinski, R.M., Kump, L.R., Arthur, M.A., 2004. The effectiveness of the Paleoproterozoic biological pump: a $\delta^{13}C$ gradient from platform carbonates of the Pethei Group (Great Slave Lake Supergroup, NWT). Geol. Soc. Am. Bull. 116, 539–554.

Hou, K., Li, Y., Gao, J., Liu, F., Qin, Y., 2014. Geochemistry and Si–O–Fe isotope constraints on the origin of banded iron formations of the Yuanjiacun Formation, Lvliang Group, Shanxi, China. Ore Geol. Rev. 57, 288–298.
Huberty, J.M., Konishi, H., Heck, P.R., Fournelle, J.H., Valley, J.W., Xu, H., 2012. Silician magnetite from the Dales Gorge Member of the Brockman Iron Formation, Hamersley Group, Western Australia. Am. Mineral. 97, 26–37.
Hulbert, L.J., Hamilton, M.A., Horan, M.F., Scoates, R.F.J., 2005. U-Pb zircon and Re-Os isotope geochronology of mineralized ultramafic intrusions and associated nickel ores from the Thompson nickel belt, Manitoba, Canada. Econ. Geol. 100, 29–41.
Huston, D.L., Logan, B.W., 2004. Barite, BIFs and bugs: evidence for the evolution of the Earth's early hydrosphere. Earth Planet. Sci. Lett. 220, 41–55.
Isley, A.E., 1995. Hydrothermal plumes and the delivery of iron to banded iron formation. J. Geol. 103, 169–185.
Isley, A.E., Abbott, D.H., 1999. Plume-related mafic volcanism and the deposition of banded iron formation. J. Geophys. Res. 104, 15461–15477.
Jacobsen, S.B., Pimentel-Klose, M.R., 1988a. A Nd isotopic study of the Hamersley and Michipicoten banded iron formations: the source of REE and Fe in Archean oceans. Earth Planet. Sci. Lett. 87, 29–44.
Jacobsen, S.B., Pimentel-Klose, M.R., 1988b. Nd isotopic variations in Precambrian banded iron formations. Geophys. Res. Lett. 15, 393–396.
James, H.L., 1951. Iron formation and associated rocks in the Iron River district, Michigan. Bull. Geol. Soc. Am. 62, 251–266.
James, H.L., 1954. Sedimentary facies of iron-formation. Econ. Geol. 49, 235–293.
James, H.L., Dutton, C.E., Pettijohn, F.J., Wier, K.L., 1968. Geology and ore deposits of the Iron River-Crystal Falls district, Iron County, Michigan. U. S. Geol. Surv. Prof. Pap. 570, 1–134.
Johanneson, K.H., Hawkins Jr., D.L., Cortés, A., 2006. Do Archean chemical sediments record ancient seawater rare earth element patterns? Geochim. Cosmochim. Acta 70, 871–890.
Johnson, C.M., Beard, B.L., Beukes, N.J., Klein, C., O'Leary, J.M., 2003. Ancient geochemical cycling in the Earth as inferred from Fe isotope studies of banded iron formations from the Transvaal Craton. Contrib. Mineral. Petrol. 144, 523–547.
Johnson, C.M., Roden, E.E., Welch, S.A., Beard, B.L., 2005. Experimental constraints on Fe isotope fractionation during magnetite and Fe carbonate formation coupled to dissimilatory hydrous ferric oxide reduction. Geochim. Cosmochim. Acta 69, 963–993.
Johnson, C.M., Beard, B.L., Roden, E.E., 2008a. The iron isotope fingerprints of redox and biogeochemical cycling in the modern and ancient Earth. Annu. Rev. Earth Planet. Sci. 36, 457–493.
Johnson, C.M., Beard, B.L., Klein, C., Beukes, N.J., Roden, E.E., 2008b. Iron isotopes constrain biologic and abiologic processes in banded iron formation genesis. Geochim. Cosmochim. Acta 72, 151–169.
Johnson, C.M., Ludois, J.M., Beard, B.L., Beukes, N.J., Heimann, A., 2013. Iron formation carbonates: paleoceanographic proxy or recorder of microbial diagenesis? Geology 41, 1147–1150.
Johnson, J.E., Gerpheide, A., Lamb, M.P., Fischer, W.W., 2014. O_2 constraints from Paleoproterozoic detrital pyrite and uraninite. Geol. Soc. Am. Bull. 126, 813–830.
Johnson, J.E., Webb, S.M., Ma, C., Fischer, W.W., 2016. Manganese mineralogy and diagenesis in the sedimentary rock record. Geochim. Cosmochim. Acta 173, 210–231.
Jones, C., Nomosatryo, S., Crowe, S.A., Bjerrum, C.J., Canfield, D.E., 2015. Iron oxides, divalent cations, silica, and the early Earth phosphorus crisis. Geology 43, 135–138.
Kah, L.C., Lyons, T.W., Frank, T.D., 2004. Low marine sulphate and protracted oxygenation of the Proterozoic biosphere. Nature 431, 834–838.
Kamber, B.S., Webb, G.E., 2001. The geochemistry of late Archaean microbial carbonate: implications for ocean chemistry and continental erosion history. Geochim. Cosmochim. Acta 65, 2509–2525.
Kappler, A., Newman, D.K., 2004. Formation of Fe (III) minerals by Fe(II) oxidizing photoautotrophic bacteria. Geochim. Cosmochim. Acta 68, 1217–1226.
Kappler, A., Pasquero, C., Konhauser, K.O., Newman, D.K., 2005. Deposition of banded iron formations by anoxygenic phototrophic Fe(II)-oxidizing bacteria. Geology 33, 865–868.
Kato, Y., Yamaguchi, K.E., Ohmoto, H., 2006. Rare earth elements in Precambrian banded iron formations: secular changes of Ce and Eu anomalies and evolution of atmospheric oxygen. In: Ohmoto, H., Kessler, S.K. (Eds.), Chemical and Biological Evolution of Early Earth: Constraints From Banded Iron-formations. 198. Geological Society of America Memoirs, pp. 269–289.
Kaufman, A.J., 1996. Geochemical and mineralogic effects of contact metamorphism on banded iron-formation: an example from the Transvaal Basin, South Africa. Precambrian Res. 79, 171–194.
Kaufman, A.J., Hayes, J.M., Klein, C., 1990. Primary and diagenetic controls of isotopic compositions of iron-formation carbonates. Geochim. Cosmochim. Acta 54, 3461–3473.
Kendall, B., Reinhard, C.T., Lyons, T.W., Kaufman, A.J., Poulton, S.W., Anbar, A.D., 2010. Pervasive oxygenation along late Archaean ocean margins. Nat. Geosci. 3, 647–652.
Kendall, B., van Acken, D., Creaser, R.A., 2013. Depositional age of the early Paleoproterozoic Klipputs Member, Nelani Formation (Ghaap Group, Transvaal Supergroup, South Africa) and implications for low-level Re-Os geochronology and Paleoproterozoic global correlations. Precambrian Res. 237, 1–12.
Kendall, B., Creaser, R.A., Reinhard, C.T., Lyons, T.W., Anbar, A.D., 2015. Transient episodes of mild environmental oxygenation and oxidative continental weathering during the late Archean. Sci. Adv. 1, e1500777.
Kipp, M.A., Stüeken, E.E., Bekker, A., Buick, R., 2017. Selenium isotopes record extensive marine suboxia during the Great Oxidation Event. Proc. Natl. Acad. Sci. U. S. A. 114, 875–880.
Kita, I., Taguchi, S., Matsubaya, O., 1985. Oxygen isotope fractionation between amorphous silica and water at 34–93° C. Nature 314, 83–84.
Klein, C., 2005. Some Precambrian banded iron-formations (BIFs) from around the world: their age, geologic setting, mineralogy, metamorphism, geochemistry, and origin. Am. Mineral. 90, 1473–1499.
Klein, C., Beukes, N.J., 1989. Geochemistry and sedimentology of a facies transition from limestone to iron-formation deposition in the early Proterozoic Transvaal Supergroup, South Africa. Econ. Geol. 84, 1733–1774.
Klein, C., Beukes, N.J., 1992. Time distribution, stratigraphy, and sedimentologic setting, and geochemistry of Precambrian iron-formation. In: Schopf, J.W., Klein, C. (Eds.), The Proterozoic Biosphere. Cambridge University Press, Cambridge, pp. 139–146.
Klein, C., Beukes, N.J., 1993. Sedimentology and geochemistry of the glaciogenic Late Proterozoic Rapitan Iron Formation in Canada. Econ. Geol. 88, 542–565.
Klinkhammer, G., Elderfield, H., Hudson, A., 1983. Rare-earth elements in seawater near hydrothermal vents. Nature 305, 185–188.
Koeksoy, E., Halama, M., Konhauser, K.O., Kappler, A., 2016. Using modern ferruginous habitats to interpret Precambrian banded iron formation deposition. Int. J. Astrobiol. 15, 205–217.
Koeppenkastrop, D., De Carlo, E.H., 1992. Sorption of rare-earth elements from seawater onto synthetic mineral particles: an experimental approach. Chem. Geol. 95, 251–263.
Köhler, I., Konhauser, K.O., Papineau, D., Bekker, A., Kappler, A., 2013. Biological carbon precursor to diagenetic siderite with spherical structures in iron formations. Nat. Commun. 4, 1741.
Konhauser, K.O., 2007. Introduction to Geomicrobiology. Blackwell, Oxford, pp. 1–425.
Konhauser, K.O., Hamade, T., Raiswell, R., Morris, R., Ferris, F., Southam, G., Canfield, D., 2002. Could bacteria have formed the Precambrian banded iron formations? Geology 30, 1079–1082.
Konhauser, K.O., Newman, D.K., Kappler, A., 2005. The potential significance of microbial Fe(III) reduction during deposition of Precambrian banded iron formations. Geobiology 3, 167–177.
Konhauser, K.O., Lalonde, S.V., Amskold, L., Holland, H.D., 2007a. Was there really an Archean phosphate crisis? Science 315, 1234.
Konhauser, K.O., Amskold, L., Lalonde, S.V., Posth, N.R., Kappler, A., Anbar, A., 2007b. Decoupling photochemical Fe(II) oxidation from shallow-water BIF deposition. Earth Planet. Sci. Lett. 258, 87–100.
Konhauser, K.O., Pecoits, E., Lalonde, S.V., Papineau, D., Nisbet, E.G., Barley, M.A., Arndt, N.T., Zahnle, K., Kamber, B.S., 2009. Oceanic nickel depletion and a methanogen famine before the Great Oxidation Event. Nature 458, 750–753.
Konhauser, K., Lalonde, S., Planavsky, N., Pecoits, E., Lyons, T., Mojzsis, S., Rouxel, O., Fralick, P., Barley, M., Kump, L., Bekker, A., 2011. Aerobic bacterial pyrite oxidation and acid rock drainage during the Great Oxidation Event. Nature 478, 369–373.
Konhauser, K.O., Robbins, L.J., Pecoits, E., Peacock, C., Kappler, A., Lalonde, S.V., 2015. The Archean nickel famine revisited. Astrobiology 15, 804–815.
Korenaga, J., Planavsky, N.J., Evans, D.A.D., 2017. Global water cycle and the coevolution of the Earth's interior and surface environment. Phil. Trans. R. Soc. A 375, 20150393.
Krapež, B., Barley, M.E., Pickard, A.L., 2003. Hydrothermal and resedimented origins of the precursor sediments to banded iron formations: sedimentological evidence from the early Palaeoproterozoic Brockman Supersequence of Western Australia. Sedimentology 50, 979–1011.
Krissansen-Totton, J., Buick, R., Catling, D.C., 2015. A statistical analysis of the carbon isotope record from the Archean to Phanerozoic and implications for the rise of oxygen. Am. J. Sci. 315, 275–316.
Kulik, D.A., Korzhnev, M.N., 1997. Lithological and geochemical evidence of Fe and Mn pathways during deposition of Lower Proterozoic banded iron formation in the Krivoy Rog Basin (Ukraine). In: Nicholson, K., Hein, J.R., Bühn, B., Dasgupta, S. (Eds.), Manganese Mineralization: Geochemistry and Mineralogy of Terrestrial and Marine Deposits. 119. Geological Society Special Publication, pp. 43–80.
Kump, L.R., Barley, M.E., 2007. Increased subaerial volcanism and the rise of atmospheric oxygen 2.5 billion years ago. Nature 448, 1033–1036.
Kump, L.R., Holland, H.D., 1992. Iron in Precambrian rocks: implications for the global oxygen budget of the ancient earth. Geochim. Cosmochim. Acta 56, 3217–3223.
Kump, L.R., Seyfried, W.E., 2005. Hydrothermal Fe fluxes during the Precambrian: effect of low oceanic sulfate concentrations and low hydrostatic pressure on the composition of black smokers. Earth Planet. Sci. Lett. 235, 654–662.
Kump, L.R., Barley, M.E., Kasting, J.F., 2001. Rise of atmospheric oxygen and the "upside-down" Archean mantle. Geochem. Geophys. Geosyst. 2, 2000GC000114.
Kunzmann, M., Gutzmer, J., Beukes, N.J., Halverson, G.P., 2014. Depositional environment and lithostratigraphy of the Paleoproterozoic Mooidraai Formation, Kalahari manganese field, South Africa. S. Afr. J. Geol. 117, 173–192.
Kurzweil, F., Wille, M., Gantert, N., Beukes, N.J., Schoenberg, R., 2016. Manganese oxide shuttling in pre-GOE oceans–evidence from molybdenum and iron isotopes. Earth Planet. Sci. Lett. 452, 69–78.
Laajoki, K., 1975. Rare-earth elements in Precambrian iron formations in Vaydankyla, South Puolanka area, Finland. Bull. Geol. Soc. Finl. 47, 93–107.
Laajoki, K., Saikkonen, R., 1977. On the geology and geochemistry of the Precambrian iron formations in Väyrylänkylä, South Puolanka area, Finland. Bull. Geol. Soc. Finl. 292, 1–137.
Laakso, T.A., Schrag, D.P., 2014. Regulation of atmospheric oxygen during the Proterozoic. Earth Planet. Sci. Lett. 388, 81–91.
LaBerge, G.L., Robbins, E.I., Han, T.-M., 1987. A model for the biological precipitation of Precambrian iron-formations-A: geological evidence. In: Appel, P.W.U., LaBerge, G.L. (Eds.), Precambrian Iron Formation. Precambrian Iron Formation Theophrastus, Athens, pp. 69–97.
Lalonde, S.V., Konhauser, K.O., 2015. Benthic perspective on Earth's oldest evidence for oxygenic photosynthesis. Proc. Natl. Acad. Sci. U. S. A. 112, 995–1000.
Lalonde, S., Konhauser, K.O., Amskold, L., McDermott, T., Inskeep, B.P., 2007. Chemical

reactivity of microbe and mineral surfaces in hydrous ferric oxide depositing hydrothermal springs. Geobiology 5, 219–234.
Leclerc, J., Weber, F., 1980. Geology and genesis of the Moanda manganese deposits, Republic of Gabon. In: Varentsov, I.M., Grasselly, G. (Eds.), Geology and Geochemistry of Manganese. Schweizerbart'sche Verlagsbuchhandlung, Stuttgart, pp. 89–109.
Lee, C.-T.A., Yeung, L.Y., McKenzie, N.R., Yokoyama, Y., Ozaki, K., Lenardic, A., 2016. Two-step rise in atmospheric oxygen linked to the growth of continents. Nat. Geosci. 9, 417–424.
Leith, C.K., 1903. The Mesabi iron-bearing district of Minnesota. In: Monographs. 43. U.S. Geological Survey, pp. 1–324.
Leith, A., 1935. The pre-Cambrian of the Lake Superior region, the Baraboo district, and other isolated areas in the upper Mississippi Valley. In: Kansas Geological Society Guide Books. 9. pp. 329–332.
Lepot, K., Addad, A., Knoll, A.H., Wang, J., Troadec, D., Béché, A., Javaux, E.J., 2017. Iron minerals within specific microfossil morphospecies of the 1.88 Ga Gunflint Formation. Nat. Commun. 8, 14890.
Lepp, H., Goldich, S.S., 1964. Origin of Precambrian iron formations. Econ. Geol. 59, 1025–1060.
Li, Z.H., Zhu, X.K., Tang, S.H., Li, J., Liu, H., 2010. Characteristics of rare earth elements and geological significations of BIFs from Jidong, Wutai and Lüliang area. Geoscience 24, 840–846.
Li, Y.-L., Konhauser, K.O., Cole, D.R., Phelps, T.J., 2011. Mineral ecophysiological data provide growing evidence for microbial activity in banded-iron formations. Geology 39, 707–710.
Li, Y.-L., Konhauser, K.O., Kappler, A., Hao, X.-L., 2013a. Experimental low-grade alteration of biogenic magnetite indicates microbial involvement in generation of banded iron formations. Earth Planet. Sci. Lett. 361, 229–237.
Li, W., Huberty, J., Beard, B., Valley, J., Johnson, C., 2013b. Contrasting behavior of oxygen and iron isotopes in banded iron formations as determined by *in situ* isotopic analysis. Earth Planet. Sci. Lett. 384, 132–143.
Li, W., Czaja, A.D., Van Kranendonk, M.J., Beard, B.L., Roden, E.E., Johnson, C.M., 2013c. An anoxic, Fe(II)-rich, U-poor ocean 3.46 billion years ago. Geochim. Cosmochim. Acta 120, 65–79.
Li, Y., Hou, K., Wan, D., Zhang, Z., Yue, G., 2014. Precambrian banded iron formations in the North China Craton: silicon and oxygen isotopes and genetic implications. Ore Geol. Rev. 57, 299–307.
Li, W., Beard, B.L., Johnson, C.M., 2015. Biologically-recycled continental iron: a major component in banded iron formations. Proc. Natl. Acad. Sci. U. S. A. 112, 8193–8198.
Li, C., Planavsky, N.J., Love, G.D., Reinhard, C.T., Hardisty, D., Feng, L., Bates, S.M., Huang, J., Zhang, Q., Chu, X., Lyons, T.W., 2015. Marine redox conditions in the middle Proterozoic ocean and isotopic constraints on authigenic carbonate formation: insights from the Chuanlinggou Formation, Yanshan Basin, North China. Geochim. Cosmochim. Acta 150, 90–105.
Li, Y.-L., Konhauser, K.O., Zhai, M., 2017. The formation of magnetite in the early Archean oceans. Earth Planet. Sci. Lett. 466, 103–114.
Llirós, M., Armisen, T.G., Darchambeau, F., Morana, C., Margarit, X.T., Inceoğlu, Ö., Borrego, C.M., Bouillon, S., Servais, P., Borges, A.V., Descy, J.P., Canfield, D.E., Crowe, S.A., 2015. Pelagic photoferrotrophy and iron cycling in a modern ferruginous basin. Sci Rep 5, 13803.
Lottermoser, B.G., Ashley, P.M., 2000. Geochemistry, petrology and origin of Neoproterozoic ironstones in the eastern part of the Adelaide Geosyncline, South Australia. Precambrian Res. 101, 49–67.
Lovley, D.R., Dwyer, D.F., Klug, M.J., 1982. Kinetic analysis of competition between sulfate reducers and methanogens for hydrogen in sediments. Appl. Environ. Microbiol. 43, 1373–1379.
Lovley, D.R., Kashefi, K., Vargas, M., Tor, J.M., Blunt-Harris, E.L., 2000. Reduction of humic substances and Fe(III) by hyperthermophilic microorganisms. Chem. Geol. 169, 289–298.
Luo, G., Ono, S., Beukes, N.J., Wang, D.T., Xie, S., Summons, R.E., 2016. Rapid oxygenation of Earth's atmosphere 2.33 billion years ago. Sci. Adv. 2, e1600134.
Lyons, T.W., Anbar, A.D., Severmann, S., Scott, C., Gill, B.C., 2009. Tracking euxinia in the ancient ocean: a multiproxy perspective and Proterozoic case study. Annu. Rev. Earth Planet. Sci. 37, 507–534.
Lyons, T.W., Reinhard, C.T., Love, G.D., Xiao, S., 2012. Geobiology of the Proterozoic eon. In: Knoll, A.H., Canfield, D.E., Konhauser, K.O. (Eds.), Fundamentals of Geobiology. Blackwell Publishing, Oxford, pp. 371–402.
Lyons, T.W., Reinhard, C.T., Planavsky, N.J., 2014. The rise of oxygen in Earth's early ocean and atmosphere. Nature 506, 307–315.
Machado, N., Clark, T., David, J., Goulet, N., 1997. U-Pb ages for magmatism and deformation in the New Québec Orogen. Can. J. Earth Sci. 34, 716–723.
Maliva, R.G., Knoll, A.H., Simonson, B.M., 2005. Secular change in the Precambrian silica cycle: insights from chert petrology. Geol. Soc. Am. Bull. 117, 835–845.
Mandernack, K.W., Bazylinski, D.A., Shanks, W.C., Bullen, T.D., 1999. Oxygen and iron isotope studies of magnetite produced by magnetotactic bacteria. Science 285, 1892–1896.
Marin-Carbonne, J., Robert, F., Chaussidon, M., 2014. The silicon and oxygen isotope compositions of Precambrian cherts: a record of oceanic paleo-temperatures? Precambrian Res. 247, 223–234.
Master, S., 1991. Stratigraphy, tectonic setting, and mineralization of the Early Proterozoic Magondi Supergroup, Zimbabwe: a review. 238. Economic Geology Research Unit Information Circular, Johannesburg, pp. 1–75.
Master, S., Bekker, A., Hofmann, A., 2010. A review of the stratigraphy and geological setting of the Palaeoproterozoic Magondi Supergroup, Zimbabwe - type locality for the “Lomagundi” carbon isotope excursion. Precambrian Res. 182, 254–273.
McLellan, J.G., Oliver, N.H.S., Schaubs, P.M., 2004. Fluid flow in extensional environments; numerical modelling with an application to Hamersley iron ores. J. Struct. Geol. 26, 1157–1171.
McLennan, S.M., 1989. Rare earth elements in sedimentary rocks: influence of provenance and sedimentary processes. In: Lipin, B.R., McKay, G.A. (Eds.), Geochemistry and Mineralogy of Rare Earth Elements. Reviews in Mineralogy 21. pp. 169–200.
Melezhik, V.A., Fallick, A.E., Hanski, E.J., Kump, L.R., Lepland, A., Prave, A.R., Strauss, H., 2005. Emergence of the aerobic biosphere during the Archean-Proterozoic transition: challenges of future research today. GSA Today 15, 4–11.
Michard, A., Albarède, F., 1986. The REE content of some hydrothermal fluids. Chem. Geol. 55, 51–60.
Miller, R.G., O'Nions, R.K., 1985. Sources of Precambrian chemical and clastic sediments. Nature 314, 325–330.
Miller, A.R., Reading, K.L., 1993. Iron-formation, evaporite, and possible metallogenetic implications for the Lower Proterozoic Hurwitz Group, District of Keewatin, Northwest Territories. In: Current Research Part C, Geological Survey of Canada, Paper 93-1C, pp. 179–185.
Mloszewska, A., Pecoits, E., Cates, N., Mojzsis, S.J., O'Neil, J., Robbins, L.J., Konhauser, K.O., 2012. The composition of Earth's oldest iron formations: the Nuvvuagittuq Supracrustal Belt (Québec, Canada). Earth Planet. Sci. Lett. 317-318, 331–342.
Mloszewska, A.M., Mojzsis, S.J., Pecoits, E., Papineau, D., Dauphas, N., Konhauser, K.O., 2013. Chemical sedimentary protoliths of the > 3.75 Ga Nuvvuagittuq Supracrustal Belt (Québec, Canada). Gondwana Res. 23, 574–594.
Moffett, J.W., 1994. The relationship between cerium and manganese oxidation in the marine environment. Limnol. Oceanogr. 39, 1309–1318.
Moore, J.M., Tsikos, H., Polteau, S., 2001. Deconstructing the Transvaal Supergroup, South Africa: implications for Palaeoproterozoic palaeoclimate models. J. Afr. Earth Sci. 33, 437–444.
Moore, J.M., Polteau, S., Armstrong, R., Corfu, F., Tsikos, H., 2012. The age and correlation of the Postmasburg Group, southern Africa: constraints from detrital zircon grains. J. Afr. Earth Sci. 64, 9–19.
Morris, R.C., 1993. Genetic modelling for banded iron-formations of the Hamersley Group, Pilbara Craton, Western Australia. Precambrian Res. 60, 243–286.
Mücke, A., 2005. The Nigerian manganese-rich iron-formations and their host rocks-from sedimentation to metamorphism. J. Afr. Earth Sci. 41, 407–436.
Nakada, R., Takahashi, Y., Tanimizu, M., 2016. Cerium stable isotope ratios in ferromanganese deposits and their potential as a paleo-redox proxy. Geochim. Cosmochim. Acta 181, 89–100.
Nealson, K.H., Myers, C.R., 1990. Iron reduction by bacteria: a potential role in the genesis of banded iron formations. Am. J. Sci. 290, 35–45.
Nie, N.X., Dauphas, N., Greenwood, R.C., 2017. Iron and oxygen isotope fractionation during iron UV photo-oxidation: implications for early Earth and Mars. Earth Planet. Sci. Lett. 458, 179–191.
Noffke, N., Hazen, R., Nhelko, N., 2003. Earth's earliest microbial mats in a siliciclastic marine environment (2.9 Ga Mozaan Group, South Africa). Geology 31, 673–676.
Noffke, N., Eriksson, K.A., Hazen, R.M., Simpson, E.L., 2006. A new window into early Archean life: microbial mats in Earth's oldest siliciclastic tidal deposit (3.2 Ga Moodies Group, South Africa). Geology 34, 253–256.
Nozaki, Y., Zhang, J., Amakawa, H., 1997. The fractionation between Y and Ho in the marine environment. Earth Planet. Sci. Lett. 148, 329–340.
Nutman, A.P., Bennett, V.C., Friend, C.R.L., Van Kranendonk, M.J., Chivas, A.R., 2016. Rapid emergence of life shown by discovery of 3,700-million-year-old microbial structures. Nature 537, 535–538.
Often, M., 1985. The early Proterozoic Karasjok Greenstone Belt, Norway: a preliminary description of lithology, stratigraphy and mineralization. Norges Geol. Unders. Bull. 403, 75–88.
Ojakangas, R.W., 1983. Tidal deposits in the Early Proterozoic basin of the Lake Superior region – the Palms and the Pokegama Formations: Evidence for subtidal shelf deposition of Superior type banded iron formation. In: Medaris Jr.L.G. (Ed.), Early Proterozoic Geology of the Great Lakes Region. 160. Geological Society of America Memoirs, pp. 49–66.
Ojakangas, R.W., 1994. Sedimentology and provenance of the Early Proterozoic Michigamme Formation and Goodrich Quartzite, Northern Michigan—regional stratigraphic implications and suggested correlations. U.S. Geol. Surv. Bull. 1904-R, R1–R31.
Ojakangas, R.W., Marmo, J.S., Heiskanen, K.I., 2001. Basin evolution of the Paleoproterozoic Karelian Supergroup of the Fennoscandian (Baltic) Shield. Sediment. Geol. 141–142, 255–285.
Olivarez, A.M., Owen, R.M., 1991. The europium anomaly of seawater: implications for fluvial versus hydrothermal REE inputs to the oceans. Chem. Geol. 92, 317–328.
Olson, S.L., Kump, L.R., Kasting, J.F., 2013. Quantifying the areal extent and dissolved oxygen concentrations of Archean oxygen oases. Chem. Geol. 362, 35–43.
Oonk, P.B.H., 2017. Fraction-specific Geochemistry Across the Asbestos Hills BIF of the Transvaal Supergroup, South Africa: Implications for the Origin of BIF and the History of Atmospheric Oxygen. (PhD Thesis) Rhodes University, Grahamstown, South Africa, pp. 1–209.
Paakola, J., 1971. The volcanic complex and associated manganiferous iron formation of the Porkonen-Pahtavaara area in Finnish Lapland. In: Bulletin de la Commission Géologique de Finlande. 247. pp. 1–83.
Papineau, D., Mojzsis, S.J., Schmitt, A.K., 2007. Multiple sulfur isotopes from Paleoproterozoic Huronian interglacial sediments and the rise of atmospheric oxygen. Earth Planet. Sci. Lett. 255, 188–212.
Partin, C.A., Lalonde, S.V., Planavsky, N.J., Bekker, A., Rouxel, O.J., Lyons, T.W., Konhauser, K.O., 2013a. Uranium in iron formations and the rise of atmospheric oxygen. Chem. Geol. 362, 82–90.
Partin, C.A., Bekker, A., Planavsky, N., Scott, C.T., Gill, B.C., Li, C., Podkovyrov, V., Maslov, V., Konhauser, K.O., Lalonde, S.V., Love, G.D., Poulton, S.W., Lyons, T.W.,

2013b. Large-scale fluctuations in Precambrian atmospheric and oceanic oxygen levels from the record of U in shales. Earth Planet. Sci. Lett. 369, 284–293.
Partin, C.A., Bekker, A., Sylvester, P.J., Wodicka, N., Stern, R.A., Chacko, T., Heaman, L.M., 2014. Filling in the juvenile magmatic gap: evidence for uninterrupted Paleoproterozoic plate tectonics. Earth Planet. Sci. Lett. 388, 123–133.
Partridge, M.A., Golding, S.D., Baublys, K.A., Young, E., 2008. Pyrite paragenesis and multiple sulfur isotope distribution in late Archean and early Paleoproterozoic Hamersley Basin sediments. Earth Planet. Sci. Lett. 272, 41–49.
Pavlov, A.A., Kasting, J.F., 2002. Mass-independent fractionation of sulfur isotopes in Archean sediments: strong evidence for an anoxic Archean atmosphere. Astrobiology 2, 27–41.
Pecoits, E., Gingras, M.K., Barley, M.E., Kappler, A., Posth, N.R., Konhauser, K.O., 2009. Petrography and geochemistry of the Dales Gorge banded iron formation: paragenetic sequence, source and implications for palaeo-ocean chemistry. Precambrian Res. 172, 163–187.
Pecoits, E., Smith, M.L., Catling, D.C., Philippot, P., Kappler, A., Konhauser, K.O., 2015. Atmospheric hydrogen peroxide and Eoarchean iron formations. Geobiology 13, 1–14.
Percak-Dennett, L., Roden, E.E., Beard, B.L., Johnson, C.M., 2011. Iron isotope fractionation during dissimilatory iron reduction under simulated Archean conditions. Geobiology 9, 205–220.
Perry, E.C., Tan, F.C., Morey, G.B., 1973. Geology and stable isotope geochemistry of Biwabik Iron Formation, northern Minnesota. Econ. Geol. 68, 1110–1125.
Phillips, G., Wilson, C.J.L., Campbell, I.H., Allen, C.M., 2006. U-Th-Pb detrital zircon geochronology from the southern Prince Charles Mountains, East Antarctica - defining the Archaean to Neoproterozoic Ruker Province. Precambrian Res. 148, 292–306.
Pickard, A., 2002. SHRIMP U–Pb zircon ages of tuffaceous mudrocks in the Brockman Iron Formation of the Hamersley Range, Western Australia. Aust. J. Earth Sci. 49, 491–507.
Pickard, A., 2003. SHRIMP U–Pb zircon ages for the Palaeoproterozoic Kuruman Iron Formation, Northern Cape Province, South Africa: evidence for simultaneous BIF deposition on Kaapvaal and Pilbara Cratons. Precambrian Res. 125, 275–315.
Piepgras, D.J., Jacobsen, S.B., 1992. The behavior of rare earth elements in seawater: precise determination of variations in the North Pacific water column. Geochim. Cosmochim. Acta 56, 1851–1862.
Piepgras, D.J., Wasserburg, G.J., 1980. Neodymium isotopic variations in seawater. Earth Planet. Sci. Lett. 50, 128–138.
Planavsky, N., Rouxel, O., Bekker, A., Shapiro, R., Fralick, P., Knudsen, A., 2009. Iron-oxidizing microbial ecosystems thrived in late Paleoproterozoic redox-stratified oceans. Earth Planet. Sci. Lett. 286, 230–242.
Planavsky, N., Bekker, A., Rouxel, O., Knudsen, A., Lyons, T.W., 2010a. Rare earth element and yttrium compositions of Archean and Paleoproterozoic iron formations revisited: new perspectives on the significance and mechanisms of deposition. Geochim. Cosmochim. Acta 74, 6387–6405.
Planavsky, N., Rouxel, O., Bekker, A., Lalonde, S., Konhauser, K.O., Reinhard, C.T., Lyons, T.W., 2010b. The evolution of the marine phosphate reservoir. Nature 467, 1088–1090.
Planavsky, N.J., McGoldrick, P., Scott, C.T., Li, C., Reinhard, C.T., Kelly, A.E., Chu, X.L., Bekker, A., Love, G.D., Lyons, T.W., 2011. Widespread iron-rich conditions in the mid-Proterozoic ocean. Nature 477, 448–495.
Planavsky, N.J., Bekker, A., Hofmann, A., Owens, J.D., Lyons, T.W., 2012. Sulfur record of rising and falling marine oxygen and sulfate levels during the Lomagundi Event. Proc. Natl. Acad. Sci. U. S. A. 109, 18300–18305.
Planavsky, N.J., Asael, D., Hofmann, A., Reinhard, C.T., Lalonde, S.V., Knudsen, A., Wang, X., Ossa Ossa, F., Pecoits, E., Smith, A.J.B., Beukes, N.J., Bekker, A., Johnson, T.M., Konhauser, K.O., Lyons, T.W., Rouxel, O.J., 2014a. Evidence for oxygenic photosynthesis half a billion years before the Great Oxidation Event. Nat. Geosci. 7, 283–286.
Planavsky, N.J., Reinhard, C.T., Wang, X., Thomson, D., McGoldrick, P., Rainbird, R.H., Johnson, T., Fischer, W.W., Lyons, T.W., 2014b. Low Mid-Proterozoic atmospheric oxygen levels and the delayed rise of animals. Science 346, 635–638.
Polteau, S., Moore, J.M., Tsikos, H., 2006. The geology and geochemistry of the Palaeoproterozoic Makganyene diamictite. Precambrian Res. 148, 257–274.
Posth, N.R., Hegler, F., Konhauser, K.O., Kappler, A., 2008. Alternating Si and Fe deposition caused by temperature fluctuations in Precambrian oceans. Nat. Geosci. 1, 703–708.
Posth, N.R., Huelin, S., Konhauser, K.O., Kappler, A., 2010. Size, density and composition of cell-mineral aggregates formed during anoxygenic phototrophic Fe(II) oxidation: impact on modern and ancient environments. Geochim. Cosmochim. Acta 74, 3476–3493.
Posth, N.R., Konhauser, K.O., Kappler, A., 2013a. Microbiological processes in banded iron formation deposition. Sedimentology 60, 1733–1754.
Posth, N.R., Köhler, I., Swanner, E.D., Schröder, C., Wellmann, E., Binder, B., Konhauser, K.O., Neumann, U., Berthold, C., Nowak, M., Kappler, A., 2013b. Simulating Precambrian banded iron formation diagenesis. Chem. Geol. 362, 66–73.
Posth, N.R., Canfield, D.E., Kappler, A., 2014. Biogenic Fe(III) minerals: from formation to diagenesis and preservation in the rock record. Earth Sci. Rev. 135, 103–121.
Poulton, S.W., 2017. Biogeochemistry: early phosphorus redigested. Nat. Geosci. 10, 75–76.
Poulton, S.W., Canfield, D.E., 2011. Ferruginous conditions: a dominant feature of the ocean through Earth's history. Elements 7 (2), 107–112.
Poulton, S.W., Fralick, P.W., Canfield, D.E., 2004. The transition to a sulphidic ocean ~1.84 billion years ago. Nature 431, 173–177.
Poulton, S.W., Fralick, P.W., Canfield, D.E., 2010. Spatial variability in oceanic redox structure 1.8 billion years ago. Nat. Geosci. 3, 486–490.
Prilutzky, R.E., Suslova, S.N., Nalivkina, Y.B., 1992. Reconstruction of environmental conditions of early Proterozoic carbonate deposits of the Ukrainian and Baltic Shields based on isotopic studies. Lithol. Miner. Deposits 5, 76–88.
Pufahl, P.K., Fralick, P.W., 2004. Depositional controls on Palaeoproterozoic iron formation accumulation, Gogebic Range, Lake Superior region, USA. Sedimentology 51, 791–808.
Pufahl, P.K., Hiatt, E.E., Kyser, T.K., 2010. Does the Paleoproterozoic Animikie Basin record the sulfidic ocean transition? Geology 38, 659–662.
Rasmussen, B., Buick, R., 1999. Redox state of the Archean atmosphere: evidence from detrital heavy metals in ca. 3250-2750 Ma sandstones from the Pilbara Craton, Australia. Geology 27, 115–118.
Rasmussen, B., Fletcher, I.R., Sheppard, S., 2005. Isotopic dating of the migration of low-grade metamorphic front during orogenesis. Geology 33, 773–776.
Rasmussen, B., Fletcher, I., Muhling, J., Thorne, W., Broadbent, G., 2007. Prolonged history of episodic fluid flow in giant hematite ore bodies: evidence from in situ U-Pb geochronology of hydrothermal xenotime. Earth Planet. Sci. Lett. 258, 249–259.
Rasmussen, B., Fletcher, I.R., Bekker, A., Muhling, J.R., Gregory, C.J., Thorne, A.M., 2012. Deposition of 1.88-billion-year-old iron formations as a consequence of rapid crustal growth. Nature 484, 498–501.
Rasmussen, B., Bekker, A., Fletcher, I.R., 2013. Correlation of Paleoproterozoic glaciations based on U-Pb zircon ages for tuff beds in the Transvaal and Huronian supergroups. Earth Planet. Sci. Lett. 382, 173–180.
Rasmussen, B., Krapež, B., Meier, D.B., 2014. Replacement origin for hematite in 2.5 Ga banded iron formation: evidence for postdepositional oxidation of iron-bearing minerals. Geol. Soc. Am. Bull. 126, 438–446.
Rasmussen, B., Krapež, B., Muhling, J.R., Suvorova, A., 2015. Precipitation of iron silicate nanoparticles in early Precambrian oceans marks Earth's first iron age. Geology 43, 303–306.
Rasmussen, B., Muhling, J.R., Suvorova, A., Krapež, B., 2016. Dust to dust: evidence for the formation of “primary” hematite dust in banded iron formations via oxidation of iron silicate nanoparticles. Precambrian Res. 284, 49–63.
Rasmussen, B., Muhling, J.R., Suvorova, A., Krapež, B., 2017. Greenalite precipitation linked to the deposition of banded iron formations downslope from a late Archean carbonate platform. Precambrian Res. 290, 49–62.
Reddy, T.R., Zheng, X.-Y., Roden, E.E., Beard, B.L., Johnson, C.M., 2016. Silicon isotope fractionation during microbial reduction of Fe(III)-Si gels under Archean seawater conditions and implications for iron formation genesis. Geochim. Cosmochim. Acta 190, 85–99.
Reinhard, C.T., Raiswell, R., Scott, C., Anbar, A.D., Lyons, T.W., 2009. A Late Archean sulfidic sea stimulated by early oxidative weathering of the continents. Science 326, 713–716.
Reinhard, C.T., Planavsky, N.J., Robbins, L.J., Partin, C., Gill, B.C., Lalonde, S.V., Bekker, A., Konhauser, K.O., Lyons, T.W., 2013. Proterozoic ocean redox and biogeochemical stasis. Proc. Natl. Acad. Sci. U. S. A. 110, 5357–5362.
Reinhard, C.T., Planavsky, N.J., Gill, B.C., Ozaki, K., Robbins, L.J., Lyons, T.W., Fischer, W.W., Wang, C., Cole, D.B., Konhauser, K.O., 2017. Evolution of the global phosphorus cycle. Nature 541, 386–389.
Resende, M.G., Jost, H., 2002. Petrogenese de formacoes ferriferas e methahidrotermalitos da formacao aimbe, Grupo Guarinos (Arqueano), Goias. Rev. Bras. Geosci. 25, 41–50.
Rickard, D., Luther III, G.W., 2007. Chemistry of iron sulfides. Chem. Rev. 107, 514–562.
Ricketts, B.D., Ware, M.J., Donaldson, J.A., 1982. Volcaniclastic rocks and volcaniclastic facies in the middle Precambrian (Aphebian) Belcher Group, Northwest Territories, Canada. Can. J. Earth Sci. 19, 1275–1294.
Ridgwell, A., Zeebe, R.E., 2005. The role of the global carbonate cycle in the regulation and evolution of the Earth system. Earth Planet. Sci. Lett. 234, 299–315.
Riedinger, N., Formolo, M.J., Lyons, T.W., Henkel, S., Beck, A., Kasten, S., 2014. An inorganic geochemical argument for coupled anaerobic oxidation of methane and iron reduction in marine sediments. Geobiology 12, 172–181.
Robbins, L.J., Lalonde, S.V., Saito, M.A., Planavsky, N.J., Mloszewska, A.M., Pecoits, E., Scott, C., Dupont, C.L., Kappler, A., Konhauser, K.O., 2013. Authigenic iron oxide proxies for marine zinc over geological time and implications for eukaryotic metallome evolution. Geobiology 11, 295–306.
Robbins, L.J., Swanner, E.D., Lalonde, S.V., Eickhoff, M., Paranich, M.L., Reinhard, C.T., Peacock, C.L., Kappler, A., Konhauser, K.O., 2015. Limited Zn and Ni mobility during simulated iron formation diagenesis. Chem. Geol. 402, 30–39.
Robbins, L.J., Lalonde, S.V., Planavsky, N.J., Partin, C.A., Reinhard, C.T., Kendall, B., Scott, C., Hardisty, D.S., Gill, B.C., Alessi, D.S., Dupont, C.L., Saito, M.A., Crowe, S.A., Poulton, S.W., Bekker, A., Lyons, T.W., Konhauser, K.O., 2016. Trace elements at the intersection of marine biological and geochemical evolution. Earth Sci. Rev. 163, 323–348.
Robert, F., Chaussidon, M., 2006. A palaeotemperature curve for the Precambrian oceans based on silicon isotopes in cherts. Nature 443, 969–972.
Rolim, V.K., Rosiere, C.A., Santos, J.O.S., McNaughton, N.J., 2016. The Orosirian-Statherian banded iron formation-bearing sequences of the southern border of the Espinhaco Range, southeast Brazil. J. S. Am. Earth Sci. 65, 43–66.
Roscoe, S.M., 1969. Huronian rocks and uraniferous conglomerates in the Canadian Shield. Geol. Surv. Can. Pap. 68-40, 1–205.
Roscoe, S.M., Gandhi, S.S., Charbonneau, B.W., Maurice, Y.T., Gibb, R.A., 1987. Mineral resource assessment of the area in the East Arm (Great Slave Lake) and Artillery Lake region, N.W.T. proposed as a National Park. In: Geological Survey of Canada, Open File 1434, pp. 1–92.
Rouxel, O.J., Bekker, A., Edwards, K.J., 2005. Iron isotope constraints on the Archean and Paleoproterozoic ocean redox state. Science 307, 1088–1091.
Rye, R., Holland, H.D., 1998. Paleosols and the evolution of atmospheric oxygen: a critical review. Am. J. Sci. 298, 621–672.

Saito, M.A., Noble, A.E., Tagliabue, A., Goepfert, T.J., Lamborg, C.H., Jenkins, W.J., 2013. Slow-spreading submarine ridges in the South Atlantic as a significant oceanic iron source. Nat. Geosci. 6, 775–779.
Satkoski, A., Beukes, N.J., Li, W., Beard, B.L., Johnson, C.M., 2015. A redox-stratified ocean 3.2 billion years ago. Earth Planet. Sci. Lett. 430, 43–53.
Satkoski, A., Lowe, D.R., Beard, B.L., Coleman, M.L., Johnson, C.M., 2016. A high continental weathering flux into Paleoarchean seawater revealed by strontium isotope analysis of 3.26 Ga barite. Earth Planet. Sci. Lett. 45, 28–35.
Satkoski, A.M., Fralick, P., Beard, B.L., Johnson, C.M., 2017. Initiation of modern-style plate tectonics recorded in Mesoarchean marine chemical sediments. Geochim. Cosmochim. Acta 209, 216–232.
Schmidt, R.G., 1980. The Marquette Range Supergroup in the Gogebic iron district, Michigan and Wisconsin. In: U.S. Geological Survey Bulletin 1460, (96 pp.).
Schneider, D.A., Bickford, M.E., Cannon, W.F., Schulz, K.J., Hamilton, M.A., 2002. Age of volcanic rocks and syndepositional iron formations, Marquette Range Supergroup: implications for the tectonic setting of Paleoproterozoic iron formations of the Lake Superior region. Can. J. Earth Sci. 39, 999–1012.
Schneiderhan, E.A., Gutzmer, J., Strauss, H., Mezger, K., Beukes, N.J., 2006. The chemostratigraphy of a Paleoproterozoic MnFe- and BIF succession - the Voëlwater Subgroup of the Transvaal Supergroup in Griqualand West, South Africa. S. Afr. J. Geol. 109, 63–80.
Schnetzler, C.C., Philpotts, J.A., 1970. Partition coefficients of rare-earth elements between igneous matrix material and rock-forming mineral phenocrysts—II. Geochim. Cosmochim. Acta 34, 331–340.
Schröder, S., Bekker, A., Beukes, N.J., Strauss, H., van Niekerk, H.S., 2008. Rise in seawater sulphate concentration associated with the Paleoproterozoic positive carbon isotope excursion: evidence from sulphate evaporites in the ~2.2-2.1 Gyr shallow-marine Lucknow Formation, South Africa. Terra Nova 2, 108–117.
Schröder, S., Bedorf, D., Beukes, N.J., Gutzmer, J., 2011. From BIF to red beds: sedimentology and sequence stratigraphy of the Paleoproterozoic Koegas Subgroup (South Africa). Sediment. Geol. 236, 25–44.
Schulz, K.J., Cannon, W.F., 2007. The Penokean orogeny in the Lake Superior region. Precambrian Res. 157, 4–25.
Schulz, K.J., Cannon, W.F., 2008. Synchronous deposition of Paleoproterozoic Superior-type banded iron-formations and volcanogenic massive sulfides in the Lake Superior region: implications for the tectonic evolution of the Penokeon orogen [abs.]. In: Geological Society of America Abstracts with Programs. 40. pp. 385.
Schweigart, H., 1965. Genesis of the iron ores of the Pretoria Series, South Africa. Econ. Geol. 60, 269–298.
Scott, C., Lyons, T.W., Bekker, A., Shen, Y., Poulton, S., Chu, X., Anbar, A., 2008. Tracing the stepwise oxygenation of the Proterozoic ocean. Nature 452, 456–459.
Scott, C., Bekker, A., Reinhard, C.T., Schnetger, B., Krapež, B., Rumble III, D., Lyons, T.W., 2011. Late Archean euxinic conditions before the rise of atmospheric oxygen. Geology 39, 119–122.
Scott, C., Planavsky, N.J., Dupont, C.L., Kendall, B., Gill, B.C., Robbins, L.J., Husband, K.F., Arnold, G.L., Wing, B.A., Poulton, S.W., Bekker, A., Anbar, A.D., Konhauser, K.O., Lyons, T.W., 2013. Bioavailability of zinc in marine systems through time. Nat. Geosci. 6, 125–128.
Scott, C., Wing, B.A., Bekker, A., Planavsky, N.J., Medvedev, P., Bates, S.M., Yun, M., Lyons, T.W., 2014. Pyrite multiple-sulfur isotope evidence for rapid expansion and contraction of the early Paleoproterozoic seawater sulfate reservoir. Earth Planet. Sci. Lett. 389, 95–104.
Severmann, S., Lyons, T.W., Anbar, A., McManus, J., Gordon, G., 2008. Modern iron isotope perspective on the benthic iron shuttle and the redox evolution of ancient oceans. Geology 36, 487–490.
Shapiro, R.S., Konhauser, K.O., 2015. Hematite-coated microfossils: primary ecological fingerprint or taphonomic oddity of the Paleoproterozoic? Geobiology 13, 209–224.
Shen, Y., Knoll, A.H., Walter, M.R., 2003. Evidence for low sulphate and anoxia in a mid-Proterozoic marine basin. Nature 423, 632–635.
Sherlock, R.L., Shannon, A., Hebel, M., Lindsay, D., Madsen, J., Sandeman, H., Hrabi, B., Mortensen, J.K., Tosdal, R.M., Friedman, R., 2012. Volcanic stratigraphy, geochronology, and gold deposits of the Archean Hope Bay Greenstone Belt, Nunavut, Canada. Econ. Geol. 107, 991–1042.
Shih, P.M., Hemp, J., Ward, L.M., Matzke, N.J., Fischer, W.W., 2016. Crown group Oxyphotobacteria postdate the rise of oxygen. Geobiology 15, 19–29.
Shimizu, H., Umemoto, N., Masuda, A., Appel, P.W.U., 1990. Sources of iron formations in the Archean Isua and Malene supracrustals, West Greenland: evidence from La-Ce and Sm-Nd isotopic data and REE abundances. Geochim. Cosmochim. Acta 54, 1147–1154.
Shimizu, H., Amano, M., Masuda, A., 1991. La-Ce and Sm-Nd systematics of siliceous sedimentary rocks: a clue to marine environment in their deposition. Geology 19, 369–371.
Siahi, M., Hofmann, A., Sharad, M., Mueller, C., Gerdes, A., 2017. Carbonate ooids of the Mesoarchean Pongola Supergroup, South Africa. Geobiology (in press).
Siever, R., 1992. The silica cycle in the Precambrian. Geochim. Cosmochim. Acta 56, 3265–3272.
Simon, A.C., Pettke, T., Candela, P.A., Piccoli, P.M., Heinrich, C.A., 2004. Magnetite solubility and iron transport in magmatic-hydrothermal environments. Geochim. Cosmochim. Acta 68, 4905–4914.
Simonson, B.M., 1985. Sedimentology of cherts in the Early Proterozoic Wishart Formation, Quebec-Newfoundland, Canada. Sedimentology 32, 23–40.
Simonson, B.M., 2003. Origin and evolution of large Precambrian iron formations. In: Chan, M.A., Archer, A.W. (Eds.), Extreme Depositional Environments: Mega End Members in Geologic Time. Geological Society of America Special Paper 370, Boulder, CO, pp. 231–244.
Simonson, B.M., Goode, A.D.T., 1989. First discovery of ferruginous chert arenites in the early Precambrian Hamersley Group of Western Australia. Geology 17, 269–272.
Simonson, B.M., Hassler, S.W., 1996. Was the deposition of large Precambrian iron formations linked to major marine transgressions? J. Geol. 104, 665–676.
Slack, J.F., Cannon, W.F., 2009. Extraterrestrial demise of banded iron formations 1.85 billion years ago. Geology 37, 1011–1014.
Slack, J.F., Grenne, T., Bekker, A., Rouxel, O.J., Lindberg, P.A., 2007. Suboxic deep seawater in the late Paleoproterozoic: evidence from hematitic chert and iron formation related to seafloor-hydrothermal sulfide deposits, central Arizona, USA. Earth Planet. Sci. Lett. 255, 243–256.
Slack, J.F., Grenne, T., Bekker, A., 2009. Seafloor-hydrothermal Si-Fe-Mn exhalites in the Pecos greenstone belt, New Mexico, and the redox state of ca. 1720 Ma deep seawater. Geosphere 5, 302–314.
Søgaard, E.G., Medenwaldt, R., Abraham-Peskir, J.V., 2000. Conditions and rates of biotic and abiotic iron precipitation in selected Danish freshwater plants and microscopic analysis of precipitate morphology. Water Res. 34, 2675–2682.
Spier, C.A., de Oliveira, S.M.B., Sial, A.N., Rios, F.J., 2007. Geochemistry and genesis of the banded iron formations of the Cauê Formation, Quadrilátero Ferrífero, Minas Gerais, Brazil. Precambrian Res. 152, 170–206.
Sreenivas, B., Murakami, T., 2005. Emerging views on the evolution of atmospheric oxygen during the Precambrian. J. Mineral. Petrol. Sci. 100, 184–201.
Stefurak, E.J.T., Fischer, W.W., Lowe, D.R., 2015. Texture-specific Si isotope variations in Barberton Greenstone Belt cherts record low temperature fractionations in early Archean seawater. Geochim. Cosmochim. Acta 150, 26–52.
Steinhofel, G., Horn, I., von Blackenburg, F., 2009. Micro-scale tracing of Fe and Si isotope signatures in banded iron formation using femtosecond laser ablation. Geochim. Cosmochim. Acta 73, 5343–5360.
Steinhofel, G., von Blackenburg, F., Horn, I., Konhauser, K.O., Beukes, N.J., Gutzmer, J., 2010. Deciphering formation processes of banded iron formations from the Transvaal and the Hamersley successions by combined Si and Fe isotope analysis using UV femtosecond laser ablation. Geochim. Cosmochim. Acta 74, 2677–2696.
Stott, G.M., Hamilton, M.A., Kamo, S.L., 2010. Archean granitoid geochronology and interpretations, Hudson Bay Lowland. In: Summary of Field Work and Other Activities 2010. 6260. Ontario Geological Survey, pp. 21–27 (Open File Report).
Straub, K.L., Rainey, F.A., Widdel, F., 1999. Rhodovulum iodosum sp. nov., and Rhodovulum religious sp. nov., two new marine phototrophic ferrous-iron-oxidizing purple bacteria. Int. J. Syst. Bacteriol. 49, 729–735.
Strauss, H., 2003. Sulphur isotopes and the early Archaean sulphur cycle. Precambrian Res. 126, 349–361.
Stüeken, E.E., Catling, D.C., Buick, R., 2012. Contributions to late Archaean sulphur cycling by life on land. Nat. Geosci. 5, 722–725.
Stüeken, E.E., Buick, R., Guy, B.M., Koehler, M.C., 2015a. Isotopic evidence for biological nitrogen fixation by molybdenum-nitrogenase from 3.2 Gyr. Nature 520, 666–669.
Stüeken, E.E., Buick, R., Anbar, A.D., 2015b. Selenium isotopes support free O_2 in the latest Archean. Geology 43, 259–262.
Sumner, D.Y., 1997. Carbonate precipitation and oxygen stratification in Late Archean seawater as deduced from facies and stratigraphy of the Gamohaan and Frisco formations, Transvaal Supergroup, South Africa. Am. J. Sci. 297, 455–487.
Sumner, D.Y., Bowring, S.A., 1996. U-Pb geochronological constraints on deposition of the Campbellrand Subgroup, Transvaal Supergroup, South Africa. Precambrian Res. 79, 25–35.
Sumner, D.Y., Hawes, I., Mackey, T.J., Jungle, A.D., Doran, P.T., 2015. Antarctic microbial mats: a modern analog for Archean lacustrine oxygen oases. Geology 43, 887–890.
Sun, S., Konhauser, K.O., Kappler, A., Li, Y.-L., 2015. Primary hematite in Neoarchean to Paleoproterozoic oceans. Geol. Soc. Am. Bull. 127, 850–861.
Sverjensky, D.A., 1984. Europium redox equilibria in aqueous solution. Earth Planet. Sci. Lett. 67, 70–78.
Swanner, E.D., Planavsky, N.J., Lalonde, S.V., Robbins, L.J., Bekker, A., Rouxel, O.J., Saito, M.A., Kappler, A., Mojzsis, S.J., Konhauser, K.O., 2014. Cobalt and marine redox evolution. Earth Planet. Sci. Lett. 390, 253–263.
Swanner, E.D., Mloszewska, A.M., Cirpka, O.A., Schoenberg, R., Konhauser, K.O., Kappler, A., 2015. Modulation of oxygen production in Archaean oceans by episodes of Fe(II) toxicity. Nat. Geosci. 8, 126–130.
Syme, E.C., Bailes, A.H., 1993. Stratigraphic and tectonic setting of Early Proterozoic volcanogenic massive sulfide deposits, Flin Flon, Manitoba. Can. J. Earth Sci. 88, 566–589.
Szpunar, M., Hand, M., Barovich, K., Jagodzinski, E., Belousova, E., 2011. Isotopic and geochemical constraints on the Paleoproterozoic Hutchison Group, southern Australia: implications for Paleoproterozoic continental reconstructions. Precambrian Res. 187, 99–126.
Taitel-Goldman, N., Singer, A., 2002. Metastable Si-Fe phases in hydrothermal sediments of Atlantis II Deep, Red Sea. Clay Miner. 37, 235–248.
Tamaura, Y., Yoshida, T., Katsura, T., 1984. The synthesis of green rust II(FeII1–FeII2) and its spontaneous transformation into Fe_3O_4. Bull. Chem. Soc. Jpn. 57, 2411–2416.
Tanaka, T., H, S., Kawata, Y., Masuda, A., 1982. Combined La–Ce and Sm–Nd isotope systematics in petrogenetic studies. Nature 327, 113–117.
Taylor, S.R., McLennan, S.M., 1985. The Continental Crust: Its Composition and Evolution: An Examination of the Geochemical Record Preserved in Sedimentary Rocks. Blackwell, Oxford, pp. 1–312.
Taylor, D., Dalstra, H.J., Harding, A.E., Broadbent, G.C., Barley, M.E., 2001. Genesis of high-grade hematite orebodies of the Hamersley Province, Western Australia. Econ. Geol. 96, 837–873.
Tebo, B.M., Johnson, H.A., McCarthy, J.K., Templeton, A.S., 2005. Geomicrobiology of manganese(II) oxidation. Trends Microbiol. 13, 421–428.
Thomazo, C., Ader, M., Philippot, P., 2011. Extreme ^{15}N-enrichments in 2.72-Gyr-old sediments: evidence for a turning point in the nitrogen cycle. Geobiology 9, 107–120.

Thomson, D., Rainbird, R.H., Planavsky, N., Lyons, T.W., Bekker, A., 2015. Chemostratigraphy of the Shaler Supergroup, Victoria Island, NW Canada: a record of ocean composition prior to the Cryogenian glaciations. Precambrian Res. 263, 232–245.
Thorne, W., Hagemann, S., Vennemann, T., Oliver, N., 2009. Oxygen isotope compositions of iron oxides from high-grade BIF-hosted iron ore deposits of the central Hamersley Province, Australia: constraints on the evolution of hydrothermal fluids. Econ. Geol. 104, 1019–1035.
Tosca, N.J., Guggenheim, S., Pufahl, P.K., 2016. An authigenic origin for Precambrian greenalite: implications for iron formation and the chemistry of ancient seawater. Geol. Soc. Am. Bull. 128, 511–530.
Towe, K.M., 1994. Earth's earliest atmosphere: Constraints and opportunities for early evolution. In: Bengtson, S. (Ed.), Early Life on Earth. Columbia University Press, New York, pp. 36–47.
Towe, K.M., 1996. Environmental oxygen conditions during the origin and early evolution of life. Adv. Space Res. 18, 7–15.
Tréguer, P., Nelson, D.M., Van Bennekom, A.J., DeMaster, D.J., Leynaert, A., Quéguiner, B., 1995. The silica balance in the world ocean: a reestimate. Science 268, 375–379.
Trendall, A.F., 2002. The significance of iron-formation in the Precambrian stratigraphic record. Int. Assoc. Sedimentol. Spec. Publ. 33, 33–66.
Trendall, A., Blockley, J., 1970. The iron formations of the Precambrian Hamersley Group, Western Australia with special reference to the associated crocidolite. In: Western Australia Geological Survey Bulletin 119, pp. 1–366.
Trendall, A., Blockley, J., 2004. Precambrian iron-formation. In: Eriksson, P.G., Altermann, W., Nelson, D.R., Mueller, W.U., Catuneanu, O. (Eds.), The Precambrian Earth: Tempos and Events. Elsevier, Amsterdam, pp. 403–421.
Trendall, A.F., Nelson, D., Thorne, A., Compston, W., Williams, I., Armstrong, R., 1990. Precise zircon U-Pb chronological comparison of the volcano-sedimentary sequences of the Kaapvaal and Pilbara cratons between about 3.1 and 2.4 Ga. In: Glover, J.E., Ho, S.E. (Eds.), Proceedings of the Third International Archaean Symposium, Perth, 1990, Extended Abstracts. Geoconferences (W.A.) Inc., Perth, pp. 81–83.
Trendall, A.F., Compston, W., Nelson, D.R., De Laeter, J.R., Bennett, V.C., 2004. SHRIMP zircon ages constraining the depositional chronology of the Hamersley Group, Western Australia. Aust. J. Earth Sci. 51, 621–644.
Tsikos, H., Moore, J.M., 1997. Petrography and geochemistry of the Paleoproterozoic Hotazel Iron-Formation, Kalahari manganese field, South Africa: implications for Precambrian manganese metallogenesis. Econ. Geol. 92, 87–97.
Tsikos, H., Beukes, N.J., Moore, J.M., Harris, C., 2003. Deposition, diagenesis, and secondary enrichment of metals in the Paleoproterozoic Hotazel Iron-Formation, Kalahari manganese field, South Africa. Econ. Geol. 98, 1449–1462.
Tsikos, H., Matthews, A., Erel, Y., Moore, J.M., 2010. Iron isotopes constrain biogeochemical redox cycling of iron and manganese in a Paleoproterozoic stratified basin. Earth Planet. Sci. Lett. 298, 125–134.
Turner, E.C., Bekker, A., 2016. Thick sulfate evaporate accumulations marking a mid-Neoproterozoic oxygenation event (Ten Stone Formation, Northwest Territories, Canada). Geol. Soc. Am. Bull. 128, 203–222.
Tyler, S.A., Barghoorn, E.S., 1954. Occurrence of structurally preserved plants in pre-Cambrian rocks of the Canadian Shield. Science 119, 606–608.
Valeton, I., Schumann, A., Vinx, R., Wieneke, M., 1997. Supergene alteration since the Upper Cretaceous on alkaline igneous and metasomatic rocks of the Poços de Caldas ring complex, Minas Gerais, Brazil. Appl. Geochem. 12, 133–154.
van den Boorn, S.H.J.M., van Bergen, M.J., Nijman, W., Vroon, P.Z., 2007. Dual role of seawater and hydrothermal fluids in Early Archean chert formation: evidence from silicon isotopes. Geology 35, 939–942.
van den Boorn, S.H.J.M., van Bergen, M.J., Vroon, P.Z., de Vries, S.T., Nijman, W., 2010. Silicon isotope and trace element constraints on the origin of ~3.5 Ga cherts: implications for Early Archaean marine environments. Geochim. Cosmochim. Acta 74, 1077–1103.
Van Wyck, N., Norman, M., 2004. Detrital zircon ages from early Proterozoic quartzites, Wisconsin, support rapid weathering and deposition of mature quartz arenites. J. Geol. 112, 305–315.
Vargas, M., Kashefi, K., Blunt-Harris, E.L., Lovely, D.R., 1998. Microbiological evidence for Fe(III) reduction on early Earth. Nature 395, 65–67.
Viehmann, S., Bau, M., Hoffmann, J.E., Münker, C., 2015. Geochemistry of the Krivoy Rog Banded Iron Formation, Ukraine, and the impact of peak episodes of increased global magmatic activity on the trace element composition of Precambrian seawater. Precambrian Res. 270, 165–180.
Walker, J.C.G., 1984. Suboxic diagenesis in banded iron formations. Nature 309, 340–342.
Walraven, F., Martini, J., 1995. Zircon Pb-evaporation age determinations for the Oak Tree Formation, Chuniespoort Group, Transvaal Sequence: implications for Transvaal-Griqualand West basin correlations. S. Afr. J. Geol. 98, 58–67.
Wan, Y.-S., Zhang, Q.-D., Song, T.-R., 2003. SHRIMP ages of detrital zircons from the Changcheng System in the Ming Tombs area, Beijing: constraints on the protolith nature and maximum depositional age of the Mesoproterozoic cover of the North China Craton. Chin. Sci. Bull. 48, 2500–2506.
Wang, C., Konhauser, K.O., Zhang, L., 2015. Depositional environment of the Paleoproterozoic Yuanjiacun banded iron formation in Shanxi Province, China. Econ. Geol. 110, 1515–1539.
Wang, C., Konhauser, K.O., Zhang, L., Zhai, M., Li, W., 2016. Decoupled sources of the 2.3-2.2 Ga Yuanjiacun banded iron formation: implications for the Nd cycle in Earth's early oceans. Precambrian Res. 280, 1–13.
Weidman, S., 1904. The Baraboo iron-bearing district of Wisconsin. In: Wisconsin Geological and Natural History Survey Bulletin. 13. pp. 1–190.
Widdel, F., Schnell, S., Heising, S., Ehrenreich, A., Assmus, B., Schink, B., 1993. Ferrous iron oxidation by anoxygenic phototrophic bacteria. Nature 362, 834–836.
Wiesli, R.A., Beard, B.L., Johnson, C.M., 2004. Experimental determination of Fe isotope fractionation between aqueous Fe(II), siderite and “green rust” in abiotic systems. Chem. Geol. 211, 343–362.
Williford, K.H., Van Kranendonk, M.J., Ushikubo, T., Kozdon, R., Valley, J.W., 2011. Constraining atmospheric oxygen and seawater sulfate concentrations during Paleoproterozoic glaciation: in situ sulfur three-isotope microanalysis of pyrite from the Turee Creek Group, Western Australia. Geochim. Cosmochim. Acta 75, 5686–5705.
Wu, L., Beard, B.L., Roden, E.E., Kennedy, C.B., Johnson, C.M., 2010. Stable Fe isotope fractionations produced by aqueous Fe(II)-hematite surface interactions. Geochim. Cosmochim. Acta 74, 4249–4265.
Wu, L., Percak-Dennett, E.M., Beard, B.L., Roden, E.E., Johnson, C.M., 2012. Stable iron isotope fractionation between aqueous Fe(II) and model Archean ocean Fe–Si co-precipitates and implications for iron isotope variations in the ancient rock record. Geochim. Cosmochim. Acta 84, 14–28.
Xiong, J., 2006. Photosynthesis: what color was its origin? Genome Biol. 7, 245.1–245.5.
Yang, W.H., Weber, K.A., Silver, W.L., 2012. Nitrogen loss from soil through anaerobic ammonium oxidation coupled to iron reduction. Nat. Geosci. 5, 538–541.
Zahnle, K.J., Claire, M., Catling, D., 2006. The loss of mass-independent fractionation in sulfur due to a Paleoproterozoic collapse of atmospheric methane. Geobiology 4, 271–283.
Zegeye, A., Bonneville, S., Benning, L.G., Sturm, A., Fowle, D.A., Jones, C., Canfield, D.E., Ruby, C., MacLean, L.C., Nomosatryo, S., Crowe, S.A., Poulton, S.W., 2012. Green rust formation controls nutrient availability in a ferruginous water column. Geology 40, 599–602.
Zhang, J., Amakawa, H., Nozaki, Y., 1994. The comparative behaviors of yttrium and lanthanides in the seawater of the North Pacific. Geophys. Res. Lett. 2, 2677–2680.
Zheng, X.-Y., Beard, B.L., Reddy, T.R., Roden, E.E., Johnson, C.M., 2016. Abiologic silicon isotope fractionation between aqueous Si and Fe(III)-Si gel in simulated Archean seawater: implications for Si isotope records in Precambrian sedimentary rocks. Geochim. Cosmochim. Acta 187, 102–122.